January 2013

Heat Transfer Measurements On An Incidence-Tolerant Low Pressure Turbine Blade In A High Speed Linear Cascade At Low To Moderate Reynolds Numbers

Leolein Patrick Gouemeni Moualeu

Follow this and additional works at: https://commons.und.edu/theses

HEAT TRANSFER MEASUREMENTS ON AN INCIDENCE–TOLERANT LOW
PRESSURE TURBINE BLADE IN A HIGH SPEED LINEAR CASCADE AT
LOW TO MODERATE REYNOLDS NUMBERS

by

Leolein Patrick Gouemeni Moualeu
Bachelor of Science, Texas A & M University, 2010

A thesis

Submitted to the Graduate Faculty

of the

University of North Dakota

in partial fulfillment of the requirements

for the degree of

Master of Science

Grand Forks, North Dakota
December
2013

This thesis, submitted by Leolein Patrick Gouemeni Moualeu in partial fulfillment of the requirements for the degree of Master of Science from the University of North Dakota, has been read by the Faculty Advisory Committee under whom the work has been done and is hereby approved.

_____
Dr. Forrest Ames

_____
Dr. Nanak Grewal

_____
Dr. Clement Tang

This thesis is being submitted by the appointed advisory committee as having met all of the requirements of the School of Graduate Studies at the University of North Dakota and is hereby approved.

_____
Dr. Wayne Swisher
Dean, School of Graduate Studies

_____
Date

Title   Heat Transfer Measurements on an Incidence–Tolerant Low Pressure Turbine Blade in a High Speed Linear Cascade at Low to Moderate Reynolds Numbers

Department Mechanical Engineering

Degree   Master of Science

In presenting this thesis in partial fulfillment of the requirements for a graduate degree from the University of North Dakota, I agree that the library of this University shall make it freely available for inspection. I further agree that permission for extensive copying for scholarly purposes may be granted by the professor who supervised my thesis work or, in his absence, by the chair person of the department or the dean of School of Graduate Studies. It is understood that any copying or publication or other use of this thesis or part thereof for financial gain shall not be allowed without my written permission. It is also understood that due recognition shall be given to me and to the University of North Dakota in any scholarly use which may be made of any material in my thesis.

<div align="center">
Leolein P. Moualeu
December 10, 2013
</div>

TABLE OF CONTENTS

CHAPTER

LIST OF TABLES

LIST OF FIGURES

NOMENCLATURE

A	Surface area, m^2
AC	Aero–derivative combustor, high turbulence
C	Blade true chord, m
c_p	Specific heat at constant pressure, $J/(kg \cdot K)$
C_p	Pressure coefficient, $C_p = P_s/P_t$
h	Heat transfer coefficient, $W/(m^2 \cdot K)$
i	Incidence angle
I	Electrical current, Amp
k	Thermal conductivity, $W/(m \cdot K)$
k	Turbulent kinetic energy, m^2/s^2
LT	Low turbulence
M, Ma_{ex}	Exit Mach number
P	Pressure
Pr	Prandtl number
q"	Heat flux, W/m^2
r	Recovery coefficient
Re_C	Reynolds number based on true chord
S	Arc or curve length, m
St	Stanton number
t	Time, s
T	Temperature, $^\circ C or K$
Tu	Turbulence intensity
V	Voltage, $volt$
V, V_{ex}	Velocity, m/s
X	Axial length, m
Z	Cross-span, m

	Symbols
β_1	Inlet angle
γ	Ratio of specific heats
ϵ	Emissivity
ε	Turbulence dissipation rate, $N/(s \cdot m^2)$
μ	Dynamic viscosity coefficient, $N \cdot s/m^2$
ρ	Density, kg/m^3
σ	Stefan–Boltzmann constant, $W/(m^2 \cdot K^4)$

	Subscripts
avg	Average
aw	Adiabatic wall state
cond	Conductive heat transfer
ex	Exit condition
s	Surface or wall
t	Total or stagnation condition
∞	Free–stream condition

ACKNOWLEDGMENTS

ABSTRACT

Runway-independent aircraft are expected to be the future for short-haul flights by improving air transportation and reducing area congestion encountered in airports. The Vehicle Systems Program of NASA identified a Large Civil Tilt-Rotor, equipped with variable–speed power–turbine engines, as the best concept. At cruise altitude, the engine rotor–speed will be reduced by as much as the 50% of take–off speed. The large incidence variation in the low pressure turbine associated with the change in speed can be detrimental to the engine performance. Low pressure turbine blades in cruise altitude are more predisposed to develop regions of boundary layer separation. Typical phenomenon such as impinging wakes on downstream blades and mainstream turbulences enhance the complexity of the flow in low pressure turbines. It is therefore important to be able to understand the flow behavior to accurately predict the losses. Research facilities are seldom able to experimentally reproduce low Reynolds numbers at relevant engine Mach number. Having large incidence swing as an additional parameter in the investigation of the boundary layer development, on a low pressure turbine blade, makes this topic unique and as a consequence requires a unique facility to conduct the experimental research.

The compressible flow wind tunnel facility at the University of North Dakota had been updated to perform steady state experiments on a modular–cascade, designed to replicate a large variation of the incidence angles. The high speed and low Reynolds number facility maintained a sealed and closed loop configuration for each incidence angle. The updated facility is capable to produce experimental Reynolds numbers as low as 45,000 and as high as 570,000 at an exit Mach number of 0.72. Pressure and surface temperature measurements were performed at these low pressure turbine conditions.

The present thesis investigates the boundary layer development on the surface of an incidence–tolerant blade. The heat transfer approach is the method used to obtain knowledge of the state of the boundary layer on the surface of the blade. Pressure and temperature

distributions are acquired for Reynolds numbers of 50,000, 66,000, 228,000, and 568,000 at an exit Mach number of 0.72, and Reynolds numbers of 228,000, and 568,000 at an exit Mach number of 0.35. These experimental flow conditions are conducted at different flow inlet angles of 40°, 34.2°, 28°, 18°, 8°, -2.6°, -12°, and -17°, and at two free–stream turbulence levels. Results of the analyses performed show that as the incidence angle decreases, a region of laminar separation bubble forms on the pressure surface and grows toward the trailing–edge. It is also noted that the position of the leading–edge moves as the incidence angle varies. A transitional flow is observed on both the pressure and suction surfaces, mainly at the two highest incidence angles, for the high turbulence case. This investigation also reveals that the Stanton number increases as the mainstream turbulence increases, and that the Stanton number at the leading–edge increases as the Reynolds number decreases, as it is documented in the literature.

CHAPTER I

INTRODUCTION

1.1 General

The next generation of aircraft, being investigated, is envisioned to mitigate the problem of airplane congestion that is present in most airports today. It is established that a solution to this issue would require aircraft to be runway independent (Vertival Take–Off and Landing VTOL) to maximize the capacity of public air transportation. The challenge of obtaining variability in the main–rotor speed then arises. Investigation of different technologies resulted in two approaches to resolve this challenge: a variable gear–ratio transmission and a variable–speed power turbine (VSPT) with fixed gear ratio. For aircraft application the variable gear–ratio transmission presents the disadvantage of adding weight to the aircraft, and therefore requiring higher fuel burn in comparison to VSPT. The investigation of rotorcraft configurations that will meet the NASA technology goals resulted to the concept of the NASA Large Civil Tilt–Rotor vehicle (LCTR) [1]. This variable–speed aircraft will be designed to take off vertically like a helicopter then at the designed altitude, the wing tips will rotate to allow the turboprop engines to be horizontal for cruise mode. The operating conditions from hover mode to cruise mode change considerably with the main–rotor speed. The cruise speed is expected to be reduced as much as 50% of take–off speed as the enthalpy extraction is maintained essentially constant [2].

1.2 Objective

The large incidence swings associated with the speed change increase loading on the VSPT blades. At cruise altitude, low pressure turbines experience low Reynolds number as a result of the pressure drop. The presence of adverse pressure gradients on highly loaded blades at low Reynolds numbers can lead to a transitional or even separated flow on the blade surfaces. The complexity of the flow in low pressure turbines can also be due to other

phenomenon such as the free–stream turbulence, impinging wakes, and surface roughness. The profile loss is most significantly determined by the development of the boundary layers and separation on the blade surfaces. Hence, it is crucial to understand boundary layer development as a function of key parameters, to be able to estimate the range of incidence angles for which the loss is minimum. For that purpose, an experimental investigation was then carried out in the compressible flow wind tunnel facility located in the Mechanical Engineering Department at the University of North Dakota. Heat transfer measurements were acquired under simulated conditions typically observed in low pressure turbines.

The incidence–tolerant turbine blade cascade investigated in the present thesis was tested under steady flow conditions. The closed–loop wind tunnel provided high speed flow at an exit Mach number of 0.72 for Reynolds numbers based on chord length and exit conditions ranging from 50,000 to 568,000. The free–stream turbulence intensities were generated by a nozzle for an estimated low turbulence of 0.47% and a mock aero–derivative combustor for an estimated high free–stream turbulence of about 5.03% (depending on the flow inlet angle). The flow angle, at the fixed blade–cascade inlet, ranges from $-17°$ to $40°$. This required eight angled nozzles to simulate each angle of attack. Heat transfer distributions were acquired using thermocouples inserted and epoxied into the surface of the blade. The static pressure distributions were also recorded to document the loading along with the cascade inlet total and static pressure, and the exit pressure.

This study is a partial contribution to the large research and technology development of the VSPT for the NASA LCTR concept. The wind tunnel results, analyzed for the current investigation, have been presented in terms of Stanton number to show the effect of the turbulence intensity, the effect of low and moderate Reynolds numbers, and the effect of varying the incidence angle on the heat transfer. These results will provide evidence to the state of the blade boundary layer development for a wide range of incidence angles. The transition process occurring in current high–lift low pressure turbines is often too complex to be accurately predicted with numerical simulation. CFD codes used to design highly loaded blades are sensitive to the transition model employed, given the advancement of

2

computers. Therefore, researchers and designers largely rely on experimental investigations to accurately predict losses. In the case of two–dimensional profile loss, for which the contribution of the boundary layers is estimated to be around 90% of the total [3],heat transfer measurements are necessary to determine the onset of transition and whether there are separations or re–attachments.

CHAPTER II

LITERATURE REVIEW

Designing the LCTR concept aims to achieve high efficiency on the highly loaded turbine blades. Efficiency is determined by characterizing the different losses generated. For much research on turbine engines, assessing the profile loss is critical in the analysis and the development of turbine blades. The mechanism of loss is complicated by the variety of flow phenomenon that are present in typical gas turbines. The mainstream turbulence, the impinging wake, the Reynolds number, the Mach number distribution, the surface roughness, and the incidence angle just to name a few, have a considerable influence on the entropy generation in the engine. The present chapter will give a background on typical losses generated by turbine blades and a summary of the transition processes will be presented. Also, previous research pertaining to the key parameters investigated in this study will be presented.

Loss mechanisms are of a particular interest in the development of turbomachines. Denton [4] reviewed different loss mechanisms that he categorized into two–dimensional loss, secondary loss, and tip leakage loss. He suggested that the three (categories of losses) are comparable in magnitude, each accounting for about $\frac{1}{3}$ of the total loss. The present thesis investigates the development of the blade boundary layers; hence the secondary loss and tip leakage loss will not be discussed.

2.1 Profile Loss in Low–Pressure Turbine

2.1.1 Profile Loss

Profiles losses are considered two–dimensional and can be determined directly from two–dimensional cascade testing [4]. Two–dimensional blade losses originate from three major sources of loss: boundary layer loss, trailing edge loss, and effect of Mach number. The development of the blade boundary layer determines the two–dimensional loss. Banieghbal

et al. [5] reported testing conducted in an unsteady wake-passing cascade wind tunnel to study the effect of wake–induced transition. They found that only 16% and 4% can be attributed to mixing and the base pressure on the trailing edge, respectively. They estimated that the profile loss for low–pressure turbine is largely dominated by the contribution of the blade boundary layers with 60% of the total loss on suction side and 20% on pressure side. Figure 2.1 shows the estimated loss breakdown for a conventional lift low–pressure turbine blade. Ames and Plesniak [6] studied the effect of high free–stream turbulence on vane aerodynamic losses and found that about 50 to 60% of the total losses could be attributed to the vane boundary layers. They also estimated that 30 to 40% of the total loss can be attributed to flow separation at the trailing edge. The loss of turbine blades increases rapidly in the sonic range, in which contribution of the trailing edge to the two–dimensional blade loss can rise significantly. Measurements by Xu and Denton [7] showed that, for Mach number ranging from 0.8 to 1.2, the trailing edge loss is the major source of profile loss for blades with typical trailing edge thickness.

2.1.2   Measurement Techniques in Transitional Flow

The boundary layers in low-pressure turbines are typically laminar in nature, and are very susceptible to separation in region of strong adverse pressure gradients. Determining the state of the boundary layer on the blade surface is desired to estimate the turbine performance. Over the past few decades, several techniques have been developed to study transitional boundary layer. The measuring devices are based on the principle that the velocity and the temperature of the moving fluid vary across the boundary layer.

Hot-wire anemometers are used mostly for detailed measurements in turbulent flows. Its principle is based on the heat transfer from a wire of 5 micro meters in diameter and 2 mm in length electrically heated element. Hot–wire anemometers are operated in constant current mode or constant temperature (CTA) mode [9], and exist in single and cross hot–wire configurations. Würz and Wagner [10], and Häggmark *et al.* [11] used hot–wire techniques for measurements in laminar separation bubbles. Würz and Wagner used a single hot-wire probe, while Häggmark *et al.* used a customized three parallel wire probe, with the central wire operating as a conventional hot-wire in CTA mode. Both investigators were
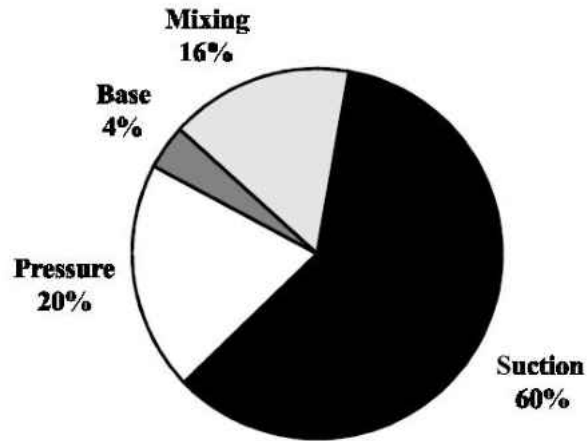
Fig. 2.1: Estimated Loss Breakdown for Datum Blade [8].

able to perform measurement of the mean velocity profiles in the laminar separation bubble. Häggmark *et al.* had an additional ability to map out and identify regions of reverse flow.

Laser or optical measurement techniques are employed in transonic flow regimes, where the operating temperatures limit usage of hot–wire probes. The laser Doppler velocimetry (LDV) is a laser measuring system often used for wind tunnel measurements. LDV operates on the Doppler shift phenomenon of the light that is scattered from the seeded particles. The sizes of the particles are typically 0.1 to 10 microns. The frequency of the scattered light is proportional to the velocity component along the bisector formed by the laser beam and the photo–detector directions [12] . The three velocity components can be measured with the used of additional beams. Young *et al.* [13], and Maresca *et al.* [14] used a laser velocimeter operating in backscatter mode to survey the flow on NACA 0012 airfoil. Maresca *et al.* obtained measurement of the axial and radial velocity components in the airfoil boundary layer, using and embedded laser velocimeter at Reynolds number ranging from 100,000 to 1,000,000, and three angles of attack $6°$, $15°$, and $21°$.Their measured velocity profile exhibited a region of reverse flow that they attributed to vortices, and the presence of separation bubble with flow re–attachment at higher upstroke flow angles. The study showed that the LDV is suited to characterize the structure of the boundary layer and the

flow direction.

The continuous rise of the turbine inlet temperature, for the purpose of obtaining higher thermal efficiency, has led to numerous experimental investigations on heat transfer development on film–cooled turbine blades. Heat transfer measurements provide insight into the state of the transitional boundary layer. The rudiments of this approach, in steady state conditions involve measurement of the surface temperature distribution, from series of thermocouples attached to a constant heat flux generated material, to determine the local heat transfer coefficients. The amount of thermocouples needed for the instrumentation of large scale cascade, to obtain good spatial resolution, can be costly and the process can be tedious. These inconveniences have increasingly favoured the use of liquid crystal techniques for heat transfer measurements. Boyle and Russell [15], Giel *et al.* [16], and Ames *et al.* [17] performed endwall heat transfer measurements in large–scale cascades using liquid crystal measurement technique. They obtained measurement of the location of the liquid crystal isotherms and generated the heat transfer results in term of contours of Stanton number. Liquid crystals are thermally sensitive in a relatively narrow temperature range, and their relatively thick coatings make them unsuitable for surface roughness investigations [18]. Other optical techniques for surface temperature measurements in transitional flow have been reported in literature. Temperature sensitive paint (TSP) is an example of such a technique that had been shown to be applicable to transitional flow with high temperature sensitivity in a transonic cryogenic wind tunnel [19].

The present heat transfer investigations that will be described in Chapter III use the traditional approach of an array of temperature sensors to obtain the surface temperature distribution. The temperature sensors cemented into the airfoil are fine gauge type–K thermocouples. A thin Inconel foil is used to dissipate constant heat flux on the surface of the blade. A finite element analysis of the blade is performed to determine the surface heat flux due to conduction through the airfoil.

2.2   Wake–Induced Transition

Flow unsteadiness in a low pressure turbine is mainly due to the relative motion and the interaction between the rotor and stator rows. The wakes shed by the upstream vane rows

interact with the downstream blades and trigger the laminar boundary layers at the blade surfaces to undergo transition. This phenomenon is termed wake–induced boundary layer transition. The effects of passing wakes on the surface boundary layers of the downstream blade rows are seldom considered in most cascade experiments. Generally, designers assume that the flow is steady within blade rows. This assumption can be inconvenient in a sense that the steady–flow wind tunnel measurements would only under–predict losses expected in real flow. A better prediction of the boundary layer development on the blade surface, therefore, demands the inclusion of wake–passing and boundary layer interactions. Few researchers have investigated the unsteady transition in turbo–machines both from the experimental and numerical standpoints.

For low pressure turbines, where the range of low Reynolds numbers can lead to a separation bubble on the suction side of the blade, the interaction of the passing wakes and the separation bubble formation reduces the profile loss. Hodson and Howell [20] presented the role of unsteady flow in a low pressure turbine. They concluded that the 'calmed regions' from the wake–induced transition, tend to reduce losses. Curtis *et al.* [8] investigated the effect of passing wakes on two blade loadings using wake generator bars passing upsteam of a blade cascade similar to that by Banieghbal *et al.* They found that the highest loaded blade presented an attractive design for low pressure turbine because it generated lower losses as compared to a datum blade profile, and could potentially reduced the number of blades by 20%. However, the profile loss generated by the wake–passing was higher than the no–wake case in their experiments. Schulte and Hodson [21] also looked at the interaction of periodic wakes with separated boundary layer on the same highly loaded blade studied by Curtis *et al.* They suggested that the profile loss can be reduced, for the wake–passing case, for a selected wake–passing frequency and wake length. They added that the Reynolds number can have virtually no effect on the pressure loss for the selected wake characteristics.

2.3   Laminar–Turbulent Flow Transition

Typical low pressure turbines feature transitional flow on the blade surface. Ideally, minimizing the profile loss requires keeping a laminar boundary layer along the blade surface [4]. This can be difficult to maintain since the flow tends to separate before transitioning

to turbulent flow. Flow phenomenon such as the low Reynolds number, high turbulence intensity, blade geometry and surface roughness, and wide range of incidence angles complicate accurate estimation of the boundary layer loss through transition. Flow transitions from laminar to turbulent when the Reynolds number based on the boundary layer momentum thickness ranges between 200 to 500 [4], depending on the level of the turbulence and unsteadiness. Periodic unsteady transition, due to the relative motion of upstream blade or vane row, partially affects the boundary layers of the downstream blades. Other three-dimensional transition mechanisms influence the blade boundary layer and they can be classified into four modes: natural transition, bypass transition, separated–flow transition, and relaminarization. Figure 2.2 shows the topology of the different modes of transition in terms of the momentum Reynolds number and the acceleration parameter (K).

Mayle [22] explained that the natural transition involves three stages in which the first stage is the growth of weak disturbances in the boundary layer in the form of a two-dimensional Tollmien–Schlichting wave. He continued by saying that the disturbances grow into three–dimensional instabilities and develop into loop–shaped vortices. The high fluctuations of the flow then develop into turbulent spots in the final stage of the process. Natural transition mode is mostly prominent in conditions of strong favorable pressure gradients and low turbulence level. Favorable pressure gradients, in comparison to adverse pressure gradients, require higher values of Reynolds number for transition. The values of Reynolds number for transition in gas turbines are an order of magnitude less than that for natural transition with low free-stream turbulence. Hence, the natural transition mode is of little relevance to gas turbines [22], and in particular to low pressure turbines.

Bypass transition involves high level of free-stream turbulence, in which the first two stages of the natural transition can be completely bypassed for direct production of turbulent spots. In the bypass transition process the disturbances are larger and non–linear, as those present in gas turbines. There are numerous studies of the influence of turbulence level on the boundary layer transition. An experimental study was carried out by Suder *et al.* [24] on the bypass transition in a boundary layer on a flat plate model subjected to

9
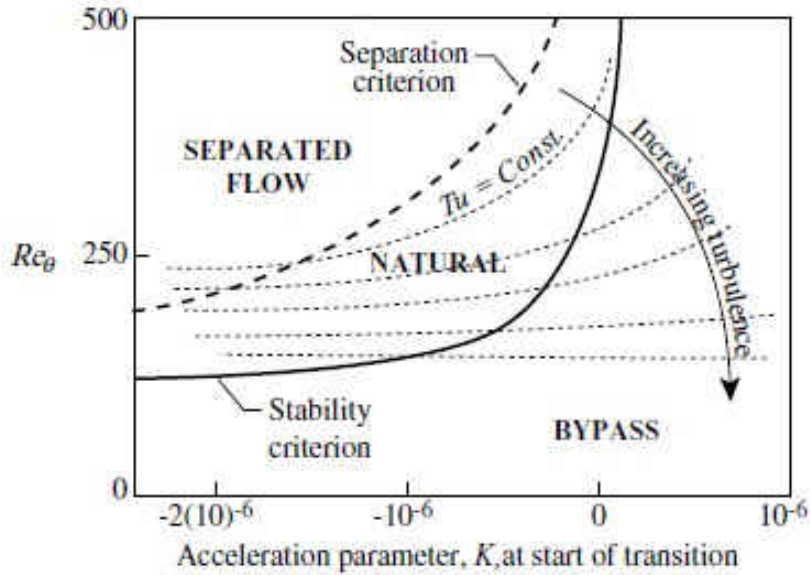
Fig. 2.2: Topology of the Different Modes of Transition in a Reynolds Number, Acceleration Parameter Plane (Mayle, 1991) [23].

free-stream turbulences. They found that the bypass transition mechanism was dominant for a minimum free–stream turbulence level of 0.65%. A similar investigation of the bypass transition induced by grid–generated turbulence was done by Anthony *et al.* [25] using high–frequency temporal heat flux imaging technique. They measured the heat flux for turbulence intensities of 2.3%, 4.2%, and 17% with a fixed integral length scale of approximately 12 mm, on a flat plate covered with high density thin platinum–film arrays. Their surface heat flux measurements reveal that the streaky nature of bypass spots occur in relatively low Reynolds number flows, and the number of turbulence–induced spots increase as the turbulence intensity increases.

Separated–flow transition is usually the result of strong adverse pressure gradients. In low pressure turbines, in which the changes in operating conditions have the most effects, the low Reynolds numbers can result in flow separation on the blades even in regions of mildly adverse pressure gradients. Mayle [22] described in Figure 2.3 the flow on a low pressure turbine airfoil within a typical operating range of Reynolds numbers. At high Reynolds numbers, transition occurs far enough upstream that the flow is turbulent over most of

the airfoil surface. Depending on the design, turbulent separation may happen near the trailing edge. Mayle added that as the Reynolds number decreases, the turbulent separation disappears and the flow is fully attached with bypass transition moving downstream, as it is seen on the right hand side of Figure 2.3. The loss corresponding to bypass transition is lowest. With further decrease in Reynolds number, laminar separation ahead of transition becomes possible. If separation does occur, the bubble is short and the flow reattaches as turbulent. In this case (shown in middle of the figure), the loss is only slightly higher than previous case. For lower Reynolds numbers, the laminar shear layer and transition length increase until reattachment before the trailing edge is no longer possible and the airfoil completely separates (see left hand side of the figure).

Laminar separation commonly occurs in low pressure turbines, which makes it the most crucial mode of transition to be accurately predicted. The over–speed region downstream of the blade stagnation region, on the suction side, can lead to a laminar separation bubble. The bubble length depends on the transition process. Designs of low pressure turbine bladings aim to improve the turbine efficiency by reducing the size of the bubbles, since large bubbles only produce large losses. Futhermore, since the nature of the separated flow is unavoidable in off–design operating conditions of the engine, it is necessary to control the flow transition through separation bubbles. The features associated with a laminar separation bubble with transition are shown in Figure 2.4. Generally, the boundary layer on the airfoil is first subjected to a favorable pressure gradient, from the leading edge, where the flow is accelerated to a maximum velocity. The flow is then decelerated, due to the presence of adverse pressure gradient, as it moves toward the trailing edge. The rising static pressure, if abrupt, may create a region of flow recirculation downstream the trailing edge and cause the boundary layer to separate from the airfoil surface. The flow separation should then be avoided due to the fact that it increases drag and reduces lift on airfoils.

The effect of flow separation is still not completely understood, and the need for a better understanding and possible prevention techniques are still current research subjects. In addition to the flow unsteadiness from periodic passing wakes, the level of free–stream tur-
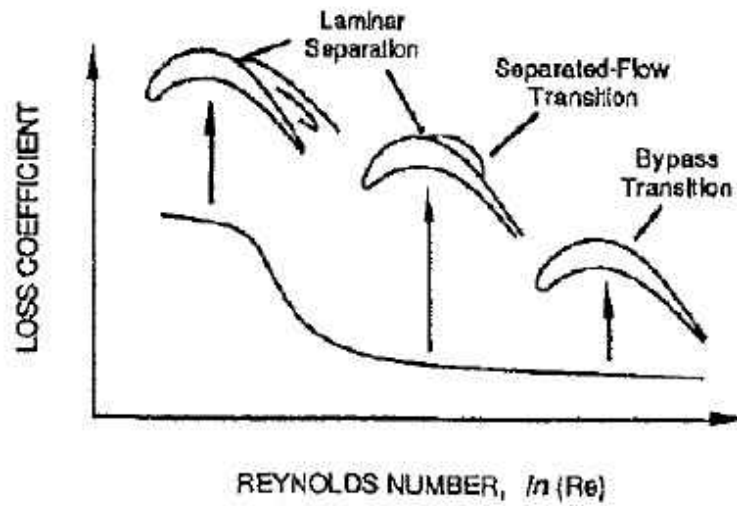
Fig. 2.3: Transition on Low Pressure Turbine Airfoil at Various Reynolds Number
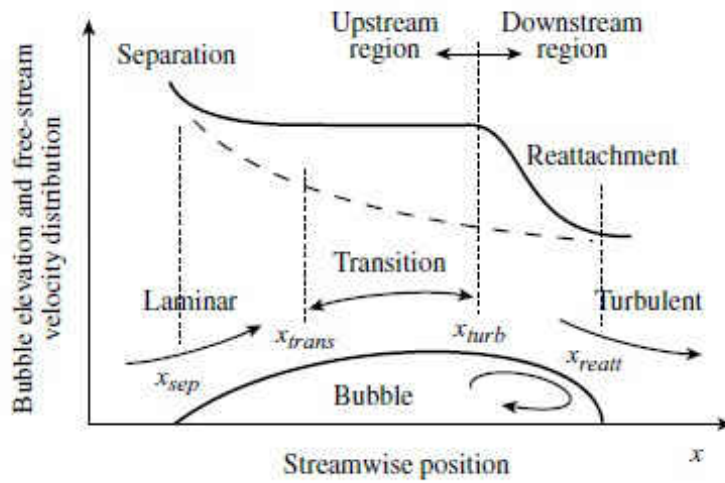
Fig. 2.4: Flow around a Separation Bubble and Corresponding Pressure Distribution (Mayle, 1991) [23].

bulence is another important parameter in understanding separated flow transition. Many experimentalists and numerical investigators have performed heat transfer studies of separated flow by examining the characteristics of turbulence. Butler *et al.* [26] studied the effect of turbulence intensity, length scale, and Reynolds number on the heat transfer distribution of a low pressure turbine blade. They carried out the heat transfer measurement on a Langston turbine blade geometry, in a linear cascade wind tunnel, at two turbulence levels. The uniform heat flux liquid crystal technique they used was complimented with Laser Thermal Tuft measurements to accurately identify flow separation from transition. Sanders *et al.* [27] investigated separation and transitional flow on a low-pressure turbine blade geometry with high level of blade loading. Their CFD model was simulated at low Reynolds numbers and compared with experimental cascade results. The influence of low Reynolds number, free–stream turbulence intensity and turbulence length scale on the suction side of a high-lift low-pressure turbine airfoil was experimentally investigated by Mahallati *et al.* [28]. The experiment was carried out in a low-speed linear cascade wind tunnel, where separated-flow transition and separation bubble characteristics were studied under steady flow conditions.

2.4   Test Facilities for Low to Moderate Reynolds Number Conditions

In spite of the progress made in gas turbines since their introduction in 1939 [22], more improvement on gas turbine components is still needed today. The increasing demands of more efficient and powerful engines with low NOx emission have further driven experimental investigations for engine components operating at low pressure. Modern wind tunnel facilities aim to create flow environment similar to those encountered in gas turbine. In low pressure turbines, the Reynolds numbers range from about 50,000 at high altitude to about 500,000 at sea-level take–off [29]. Low Reynolds number environment present in low pressure turbines can lead to flow separation which consequently can impede the blade aerodynamic performance. Assessing the effect of low Reynolds numbers combined with the wide range of incidence angles require unique test facilities.

There is a wide variety of test facilities for experimental investigations of heat transfer and aerodynamic performance of low pressure turbines. Wind tunnels can range from

closed-loop to conventional open-circuit designs, while including low–speed, transonic and pressure tunnel designs.

2.4.1   Closed–Loop Wind Tunnels

Transonic wind tunnels aim to reproduce the transonic Mach numbers and low Reynolds numbers generally observed in low pressure turbines. A high speed, low Reynolds number test facility had been developed at the Whittle Laboratory, in Cambridge University. Gostelow and Watson [30], and Hodson [31] described a closed-circuit transonic cascade facility, in which the transonic Mach number (up to 1.62 exit Mach) and the Reynolds number ranging from 100,000 to 1,300,000 can be varied independently. Hodson [31] reported successful measurements for the investigation of the boundary-layer transition and separation in the neighborhood of the leading edge of a high-speed turbine blade. Another high speed flow test facility that can be considered as pressure tunnel is the Isentropic Compression Tube (CT-2) cascade facility of the von Karman Institute, in Rhode–Saint–Genèse, Belgium. Figure 2.5 shows a schematic of the CT-2 facility. The institute website described the facility as being a 1m in diameter and 5 m long cylinder containing a light–weight piston. The piston, separated from the test section by a fast opening shuttle valve, is pushed forward by the action of high pressure air. The forward motion of the piston isentropically compresses the gas in front of it to the desired flow conditions. The shuttle valve can then be actuated to allow the stream flow over the two–dimensional linear cascade test section. The flow conditions can be maintained for 100 to 800 ms. The facility is equipped with fast response data acquisition system to obtain convective heat transfer and aerodynamic measurements. The facility instrumentations also include Schlieren visualizations, and can be accommodated for an upstream periodic wake device. Arts *et al.* [32] carried out aero–thermal performance measurements of a two–dimensional high turning rotor blade in the CT-2 facility. The second purpose of their research was to show the degree of reliability of the SNECMA–ONEMA Navier–Stokes solvers. They investigated the effect of free–stream turbulence (1 to 6%), Reynolds numbers (500,000 to 2,000,000), Mach numbers (0.8 to 1.3), and incidence angle (-14 to +11°). They used platinum thin film gages, painted at mid–span on the blade profile, to measure the local time–dependent temperature and to determine

the wall heat flux. Their results showed an increase of the heat transfer coefficient in the leading edge area and an early transition of the laminar boundary layer on the suction side, as the free–stream turbulence increases. They also found that the overall heat transfer coefficient increases with Reynolds number. The incidence swing indicated important separation bubble on the blade pressure side for -14°, and an immediate boundary layer transition on the suction side for +5°.

2.4.2   Open–circuit Wind Tunnels

Closed–loop wind tunnels can present a great advantage for a more uniform flow, in principle, in comparison to open–loop tunnels. However, the latter are suitable for confine area and cost saving. Open–circuit configurations require less components, and their arrangements can be classified as suck–down and blower tunnels [34]. Suck–down tunnel, usually called an Eiffel tunnel, is typically composed of a short settling chamber, which is basically a honeycomb sandwiched between screens, followed by a contraction and a test section, with a diffuser and a fan (or blower) downstream of the test section. Blower tunnels differ from Eiffel tunnels with a blower placed upstream of the test section. Bradshaw and Mehta [34] favored blower tunnels over suck–down tunnels due to the fact that the former are much less sensitive to entry conditions. The flow exiting the wind tunnel and turning at the corner into the bell–mouth inlet of an Eiffel configuration may carry significant swirl. Universities and research institutes that are more inclined to Eiffel configurations have dealt successfully with the possible poor flow quality at the wind tunnel inlet.

Lou and Hourmouziadis [35] conducted their experiments on an open–circuit tunnel of the Eiffel–type, located at the Berlin University of Technology. They investigated the formation of separation bubbles under steady and periodic–unsteady main flow conditions. Their facility is shown in Figure 2.6. The low–speed wind tunnel incorporates an inlet, a settling chamber fitted with a honeycomb straightener, a 9:1 square contraction, and a square test section. The test section is followed by a rotating flap to create flow oscillations and simulate the trailing edge velocity wake. A diffuser is attached at the rotating flap exit. The blower downstream of the diffuser is run by a variable speed controller, and it is capable of a volumetric rate of $2.5m^3$ [36]. The experimental setup covered a range of Reynolds
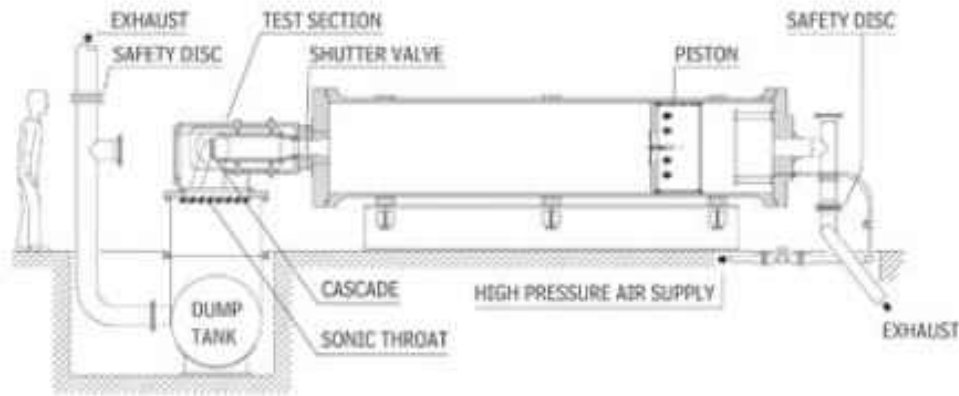
Fig. 2.5: Schematic of the Isentropic Compression Tube Cascade Facility [33]

numbers from 100,000 to 2,000,000. Dähnert *et al.* [36] studied the transition mechanisms in laminar separated flow under simulated low pressure turbine aerofoil conditions using the low–speed facility of the Berlin University of Technology. They conducted boundary layer measurements, using a hot–wire anemometry, at Reynolds numbers ranging from 80,000 to 300,000. They placed a two–dimensional contoured wall above the test plate to simulate a streamwise pressure gradient corresponding to that on the suction side of a scaled blade profile used in commercial aircraft. The comparison of their results to similar experimental investigations suggested that transition at low turbulence level and Reynolds numbers is initiated within the laminar separated shear layer due to the shear–layer instability. Also, comparing their results with available correlations revealed that the best approximation of the onset of transition is given by the model that explicitly includes the effects of Reynolds number and turbulence level.

Another suck–down tunnel type was detailed by Selig and McGranahan [37] [38] . The low–turbulence subsonic wind tunnel is shown in Figure 2.7 [38]. The experimental facility is in service at the University of Illinois at Urbana–Champaign (UIUC), and it is composed of a 10.16 cm honeycomb flow straightener and four anti–turbulence screens at the inlet. A 7.5:1 contraction is placed upstream of a 0.853 x 1.219 m test section. The test section was designed to account for boundary layer growth along the tunnel side

16
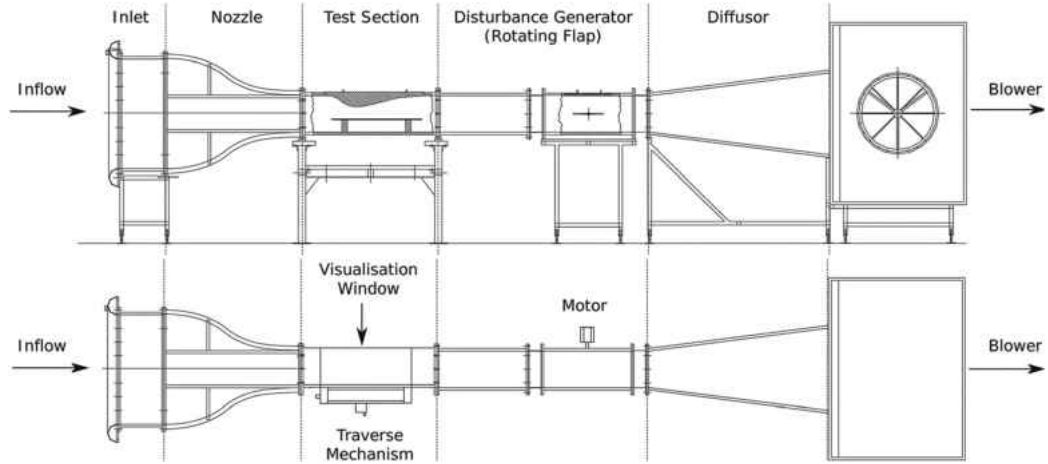
Fig. 2.6: Periodic–Unsteady Low–Speed Wind Tunnel [36]

walls. The subsonic speed is provided by means of a 93.25 kW AC motor connected to a five–bladed fan. The authors performed flow quality tests of the wind tunnel prior to investigating the aerodynamics of six airfoils for use on small wind turbines. The flow quality tests involved measurements of the free–stream turbulence, variations in dynamic pressure, and free–stream flow angle across the test section. The results of their turbulence intensity measurements, using a hot–wire anemometry, showed that the turbulence levels were sufficiently low for low Reynolds number airfoil measurements. Also, they were able to maintain an uniform flow velocity with a relatively small variation in dynamic pressure to be less than 0.2% within the region of the test model. Finally, surveys of the flow angularity by means of a seven–hole probe revealed that the pitch and yaw combined flow angle became more pronounced at lower Reynolds numbers. With the pitch angle being between 0 and 0.2°, the authors concluded that the flow angularity surveys also met the desired level of flow quality for wind tunnel aerodynamic testing.

Blower type tunnels may require a larger space relatively to comparable suck–down tunnels. However, the location of the blower (at the tunnel inlet) provides more flexibility for any desired test section [34]. The choice of a centrifugal blower over an axial fan resides in its steady efficiency over a wide range of flow conditions [39]. McAuliffe [40] used a blower tunnel to investigate flow control using blowing for a low–pressure turbine airfoil. The wind

17
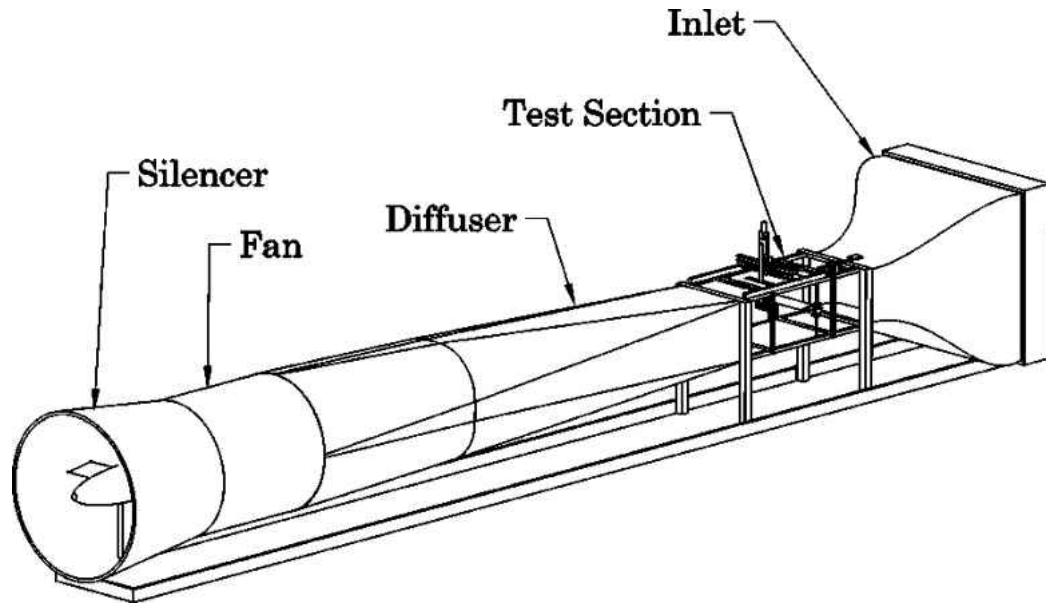
Fig. 2.7: UIUC Low–Speed Subsonic Wind Tunnel [38]

tunnel is located at the Low–Speed Turbo–machinery Laboratory at Carleton University, and it is shown in Figure 2.8. The radial blower is driven by a four–pole AC motor which is controlled by a solid–state variable–frequency controller, and supplied approximately 5 kg/s maximum flow rate with at total pressure rise of about 1.2 kPa. A square diffuser with an area ratio of 5.6 and a divergence of 19° is located at the inlet of the settling chamber. The settling chamber exit is connected to a square–to–rectangle contraction with an area ratio of 14:1. The wind tunnel provides a maximum velocity of approximately 35 m/s at the test section exit with a turbulence intensity of approximately 0.4% at the test section inlet. The author also performed cascade flow quality tests to ensure uniform inlet and periodic outlet flow on the middle blades. The tests involved measurements of the flow angle, static pressure coefficient, dynamic pressure coefficient, and total pressure loss coefficient distributions. Measurements at the inlet and the exit of the cascade were performed at 1.2 axial chord lengths upstream and 0.5 axial chord lengths downstream of the blades, respectively. The results of the inlet and exit measurements using flow control airfoils at two different turbulence levels (and blowing ratios) showed that a relative uniform flow can be achieved upstream of the cascade for the low turbulence case, with a slight drop

of the desired flow incidence angle. The lack of periodicity downstream of the cascade was attributed to the absence of flow control nearby the investigated airfoils. Flow quality tests, undertaken by the researchers presented in this section, are necessary to assess the cascade limits and extend the test results to real turbo–machineries.
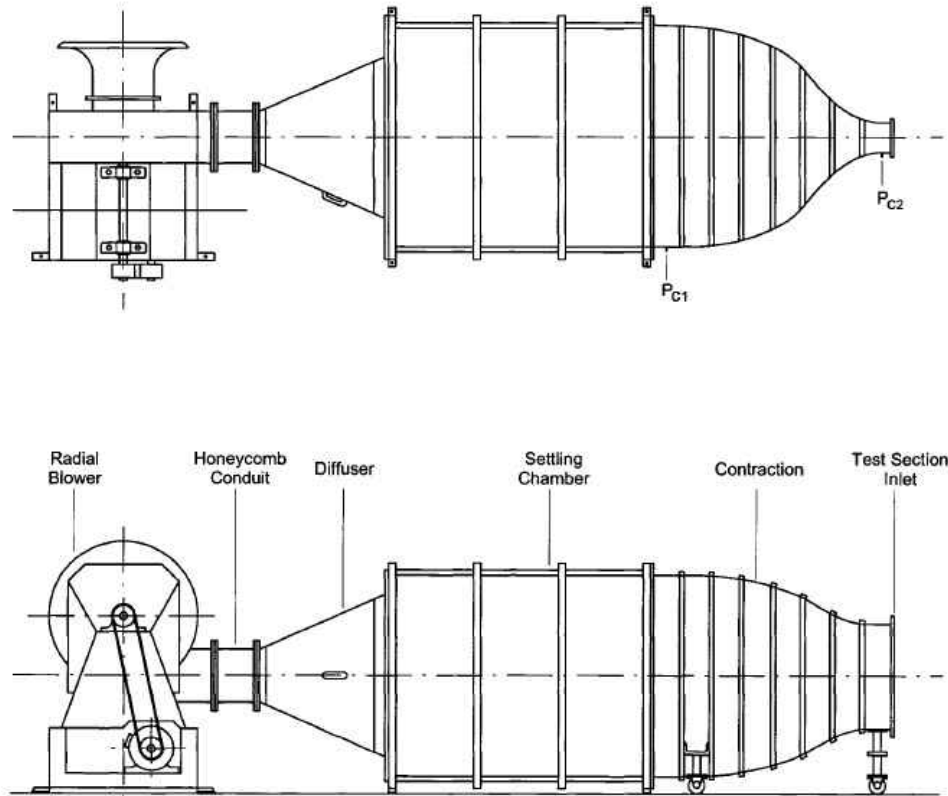
Fig. 2.8: Schematic of Low–Speed Open–Circuit Wind Tunnel [40]

2.5 Variable–Incidence Linear Cascade

Research and development in turbo–machinery mostly come from cascade experiments, and the flow measurements obtained are typically useful to the designer requiring turbine stage or individual blade row performances. Wind tunnel turbine cascades are typically classified as low–speed for the lower range of Mach numbers, and high–speed for the compressible flow rigs operating in the transonic range. It has been discussed in section [2.1.1] that the blade boundary layer layers can be well estimated in a cascade setting due to

the approximation that the flow, away from the end–wall, is two–dimensional. A well–designed blade cascade therefore requires a nearly two–dimensional flow in lieu where the flow measurements are made.

2.5.1 Effects of Incidence Angle on Pressure Loss

The cascade efficiency at the design Reynolds number and Mach number conditions can be considerably impacted by the variation of incidence flow angles. The empirical work of Ainley and Mathieson [41] provided a method for correlating the loss in a row of blades at design and off–design conditions. Their correlations considered an arithmetic mean of the rotor and stator row inner and outer diameters to estimate pressure loss at a variety of incidences. The later work of Moustapha *et al.* [42] suggested that the off–design pressure loss correlations should include the blade leading–edge diameter as a correlating parameter [43]. Benner *et al.* [43] investigated the influence of leading–edge geometry of the off–design profile losses for turbine blades. A purpose to their experiment was to bring improvement to Moustapha *et al.* correlations. They obtained their measurements in the open–circuit linear cascade located at Carleton University. The low–speed test section is shown in Figure 2.9. The set of blades are mounted on a turntable allowing the incidence to be varied over a range of $^+_-20°$. The inlet flow uniformity and the outlet flow periodicity were adjusted by the use of the side flaps and tailboards. They conducted their studies on two set of blades with different circular leading–edge diameters at a constant Reynolds number of 300,000, based on inlet velocity and true chord. The results of the pressure distribution on the larger diameter blade showed a velocity peak at the leading–edge on the suction surface as the positive incidence increases .The authors' investigations revealed that Moustapha *et al.* loss predictions do not correlate well with experimental data for the positive incidence. They claimed that by including the leading–edge wedge angle as an additional correlating parameter an improvement to Moustapha *et al.* correlations could be obtained.

2.5.2 Effects of Incidence Angle on Heat Transfer

There are other parameters influencing off–design pressure losses. These include the Reynolds number, the turbulence intensity, and chord–wise pressure distribution [43]. Meschwitz [44]
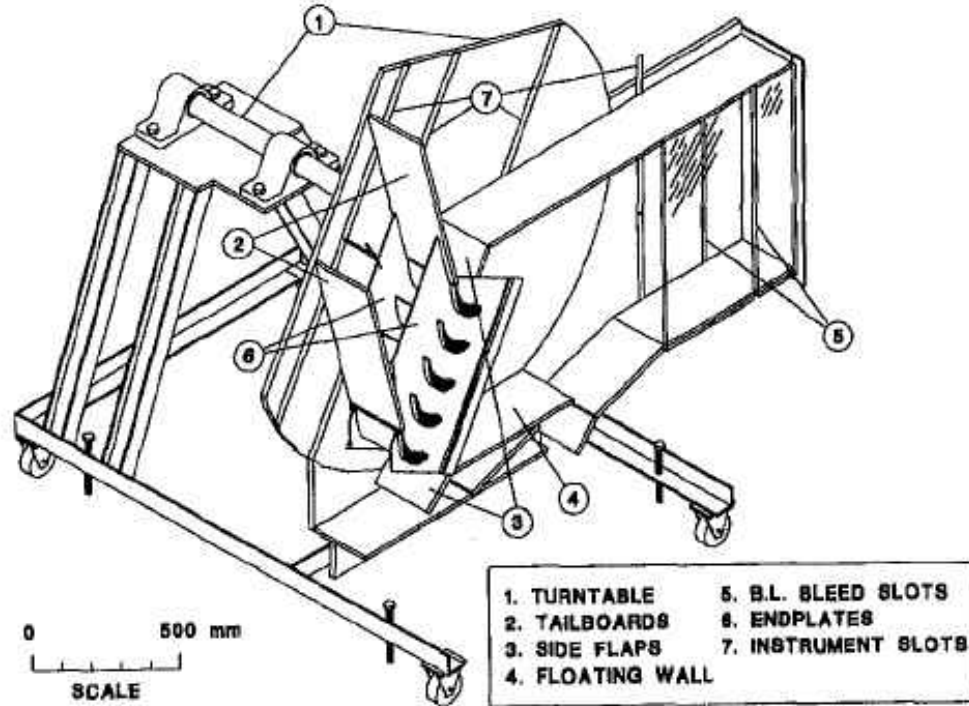
Fig. 2.9: Schematic of Variable–incidence Test Section

investigated the effect of small variation of the incidence angle (from -2.5° to +5°) on the heat transfer in a linear turbine cascade at three Reynolds numbers (400,000, 800,000, and 1,000,000 based on exit conditions) and two turbulence levels (0.5% and 10%). His results of pressure loading on the blade showed slight movement of the stagnation point on the suction side as the angle of incidence decreases. At the low turbulence level and at a given Reynolds number, the author observed that the heat transfer coefficient decreases as the angle of incidence increases with the flow separation having greater influence at the highest angle. At the high turbulence level there was no apparent change of the heat transfer as the angle of incidence was varied. The author attributed the absence of any obvious behavior to the high free–stream turbulence affecting the boundary layer. Meschwitz also noted that heat transfer coefficient increases with increasing Reynolds number, for a given angle of incidence and turbulence intensity.

21

A later work by Ames *et al.* [45] looked at the effects of incidence angle on the performance of lightly loaded turbine guide vanes at an estimated 5% turbulence intensity. The tests were conducted in a compressible flow rig with a vacuum system. The incidence angles varying from -10° to +10° were simulated by means of five slanted grids upstream of the 6–vane 5–passage cascade, combined with five sets of cascade inlet flow–blocks. Measurements of the cascade performance were performed at an exit chord Reynolds number of 1,200,000 and an exit Mach number of 0.7. From the midline pressure and heat transfer distributions acquired, the authors reported that the location and the mode of transition changes with the changing incidence angle. They pointed out that the heat transfer for the -10° incidence angle suggested that transition had been initiated through formation of separation bubble on the vane suction surface. They also noted a minimum passage loss at +5° incidence, and maximum passage loss at -10° incidence. However, they observed no significant secondary loss on the low turning cascade.

CHAPTER III

EXPERIMENTAL APPROACH

The present chapter provides detailed description of the test facility used to investigate heat transfer and aerodynamics of an incidence–tolerant turbine blade cascade. Some of the major components that were designed and built for the investigations are also presented along with the instrumented blades. This chapter also provides an overview of the data acquisition system and the analyses performed. Finally, information about typical flow quality obtained at the inlet and exit of the turbine blade cascade is presented.

3.1 High Speed Compressible Flow Wind Tunnel Facility

The experiments were conducted at the existing compressible flow facility located at the University of North Dakota. A description of the original closed–loop facility is provided by Mihelish [46]. The original facility includes an inlet tank which incorporate a fin and tube heat exchanger, a rugged 63B vacuum pump, a Roots blower of type RGS 10–18, an outlet tank which is thermally insulated, and a flow conditioning unit.

The unique facility provides independent control of the tunnel pressure and speed. The range of Reynolds numbers investigated at the Mach number of 0.72 requires a sub–atmospheric pressure range. The low pressure within the facility is maintained by the vacuum pump capable of producing an ultimate vacuum of 67 Pa (0.5 mm Hg), at a volumetric rate flow rate of 1.27 m^3/min. The vacuum is adjusted by a control system of valves and an air filter mounted on galvanized tubing that connects the vacuum pump to the inlet tank. A coarse adjustment is possible by the use of a 3.18 cm ($1\frac{1}{4}''$) ball valve, while a 1.27 cm ($\frac{1}{2}''$) needle valve provides the fine adjustment. The air filter allows intake of the outside air into the tunnel through a polyester element, filtering particulate of 5 microns in size.

The Roots rotary lobe blower, providing the air motion within the wind tunnel, is a vertical positive displacement type unit capable of a volumetric flow rate of about 105

m^3/min (3600 ft^3/min). It displaces air from the inlet tank to the outlet tank by means of a 56 KW (75 HP) electric motor that is controlled by a three phase, 60 Hz P7 Yaskawa frequency drive. The drive incorporates a LCD operator display to monitor the blower outputs, and a customized remote control to ease its operation. The good functionality of the blower is also maintained with a shell and tube heat exchanger. The flow rate of the water supply used to cool the blower lubricating oil can be adjusted and monitored through an 11 gallon per minute (GPM) rotameter.

The 1.92 m^3 inlet and outlet tanks connected to the inlet and exit of the blower were designed to be able to control the thermal load within the tunnel and reduce the unsteadiness generated by the Roots blower. Figure 3.1(a) and Figure 3.1(b) show internal images of the outlet and inlet tanks. The heat exchanger embedded inside the inlet tank is the main instrument maintaining the tunnel air temperature to the desirable level for steady state measurements. The flow rate of the water coolant supply to the inlet tank heat exchanger is monitored by a 36 GPM rotameter. The outlet tank insulation is provided by a thick and even layer of polyimide foam. The foam is covered with a white navy cloth to enhance its resistance to degradation during tunnel operation. The flow exiting the outlet tank is conditioned by a flow conditioning unit. It is a round–to–square unit composed of two offset perforated aluminum plates with an open area of 0.056 m^2, followed by two fine meshed screens at its exit.

A portion of the original facility had been redesigned to allow a large variation of the angle of incidence at the inlet of the linear cascade test section, and to facilitate its operability above atmospheric pressure. A configuration of the updated facility is shown in Figure 3.2. The incidence–tolerant blade cascade experiment was conducted for two turbulence levels: a low turbulence simulated with a straight two–dimensional nozzle, and a high turbulence simulated with the mock aero–derivative combustor. Each turbulence level was tested for Reynolds numbers of 50,000, 66,000, 228,000, and 568,000 (based on true chord and exit conditions) at the exit Mach number of 0.72, and Reynolds numbers of 228,000, and 568,000 at the exit Mach number of 0.35. Pressure and surface temperature

(a) Outlet Tank   (b) Inlet Tank
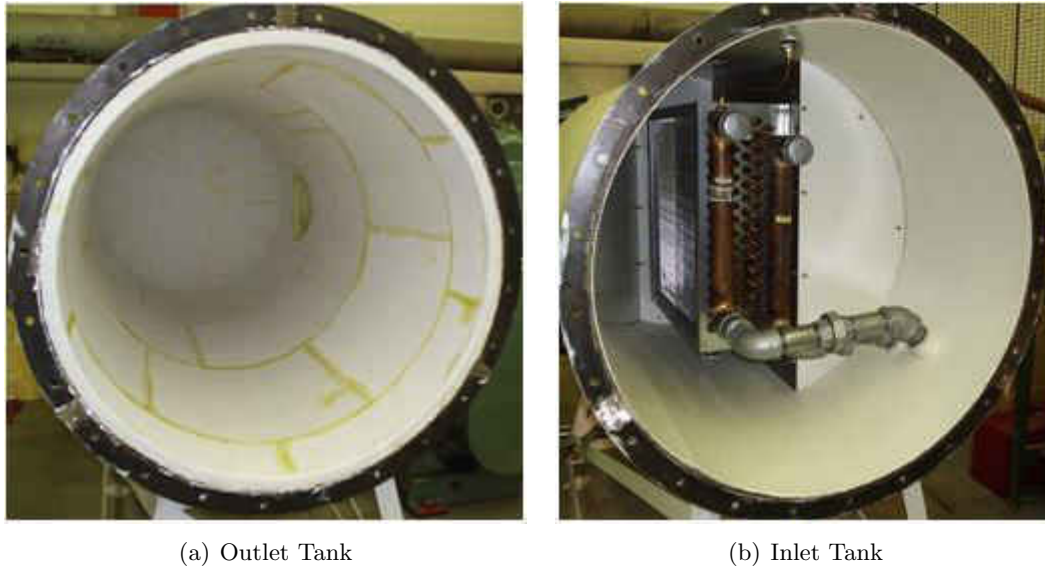
Fig. 3.1: (a) Insulated Outlet Tank and (b) Inlet Tank Containing a Fin and Tube Heat Exchanger.

distributions for all twelve conditions (six conditions for each turbulence level) were acquired at eight different flow inlet angles: 40°, 34.2°, 28°, 18°, 8°, -2.6°, -12°, and -17°.

3.2 Low and High Turbulence Generators

The low free–stream turbulence is generated by a two–dimensional straight nozzle of 2 to 1 area ratio followed by an angled nozzle which also has contraction. The open area at the inlet was designed to match the exit of the flow conditioning unit with 32.05 cm in height and 30.82 cm wide. The nozzle contour was generated from a polynomial function developed over the length of 20.32 cm so that it can easily replace the mock aero–derivative combustor for low turbulence measurements. This approach conveniently reduced the number of required slanted nozzles to be designed and built in half. A picture of the low free–stream turbulence generator is shown in Figure 3.3.

The high free–stream turbulence is generated by the mock aero–derivative combustor. Figure 3.4(a) and Figure 3.4(b) show detail drawings of the aero combustor. It was designed to reproduce similar turbulence observed in industrial gas turbine engine combustors. Air at the aero combustor inlet is forced to pass through two rows of four slots in the back panel and through two rows of eight holes in each side panel. The slots and holes create
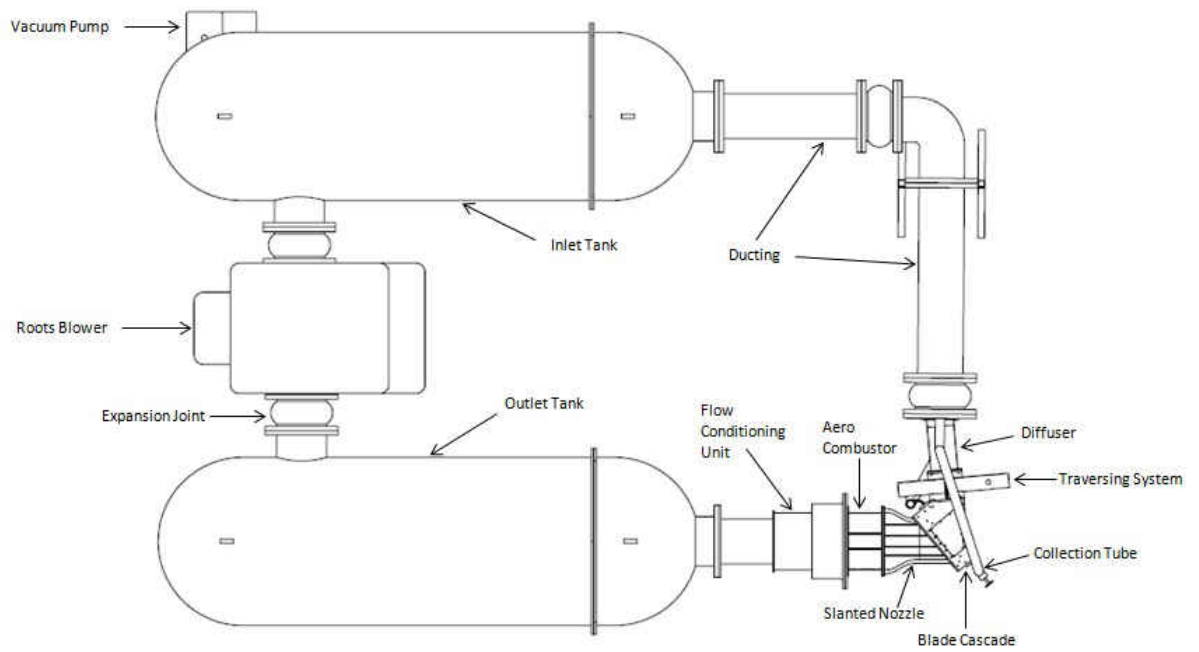
Fig. 3.2: Compressible Flow Wind Tunnel for 40° Inlet Angle Configuration.

Fig. 3.3: 2D Nozzle used of Low Turbulence Generation.

air jets similar to the recirculation and dilution zones of modern industrial gas turbine combustors [46].

(a) Back and Side Panels   (b) Aero Combustor section view
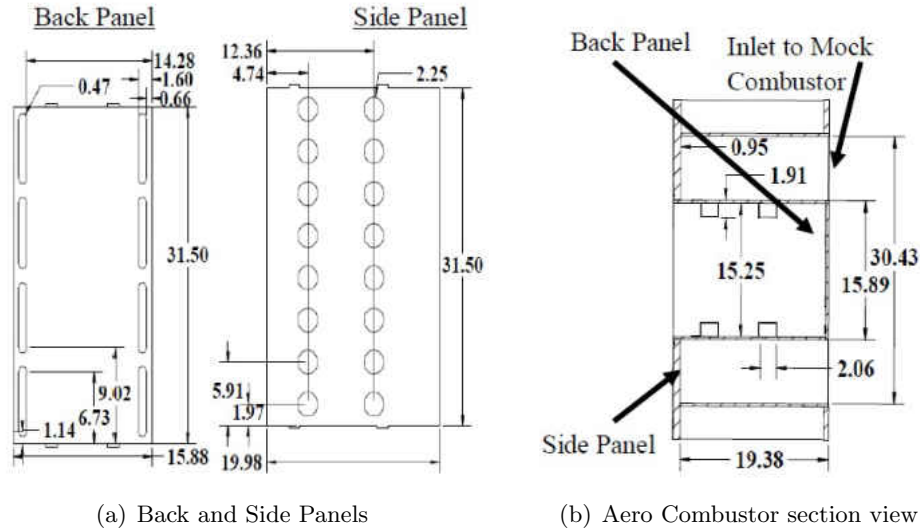
Fig. 3.4: Diagram of Aero–Derivative Combustor Turbulence Generator Showing (a) Back and Side Panels (b) Section View [46] (modified from Mihelish's thesis).

The low and high turbulence intensities were estimated from turbulence measurements performed on the vane cascade of the original facility described by Mihelish. Based on the measured bulk velocity, the turbulence parameters generated in the original facility were measured to be 0.8% (not including 1.35% for background unsteadiness) turbulence intensity with an energy length scale of 1.7 cm for the low turbulence level. The turbulence intensity for the high turbulence level was measured to be 9.0% with 2.2 cm energy scale [47]. The low and high turbulence intensities for the current investigations have not been measured at the time the present thesis was written. An estimation of both turbulence levels was performed based on the measurements done for the original facility. It was assumed that the turbulence kinetic energy generated in the tunnel would be the same for the current facility, in spite of the higher Mach number at the cascade inlet (due to the smaller inlet area as compare to the inlet of the vane cascade). Therefore, the current cascade experiences a higher bulk velocity with corresponding lower turbulence intensity. It was estimated that the mean values of the low and the high free–stream turbulence intensities would be approximately

0.47% and 5.03%, respectively, at the inlet of the current blade cascade.

3.3 Slanted Nozzles

Eight angled nozzles, 40°, 34.2°, 28°, 18°, 8°, -2.6°, -12°, and -17°, were designed to simulate different flow angles at the inlet of the blade cascade. The contours of each nozzle were obtained from a developed sixth–order polynomial function to achieve a double contraction from 31.54 cm by 15.24 cm at the inlet to 25.4 cm by 5.08 cm at the exit. Figure 3.5(a) and Figure 3.5(b) show the 40° and the -17° angled nozzles, respectively.

(a) +40° Nozzle   (b) -17° Nozzle
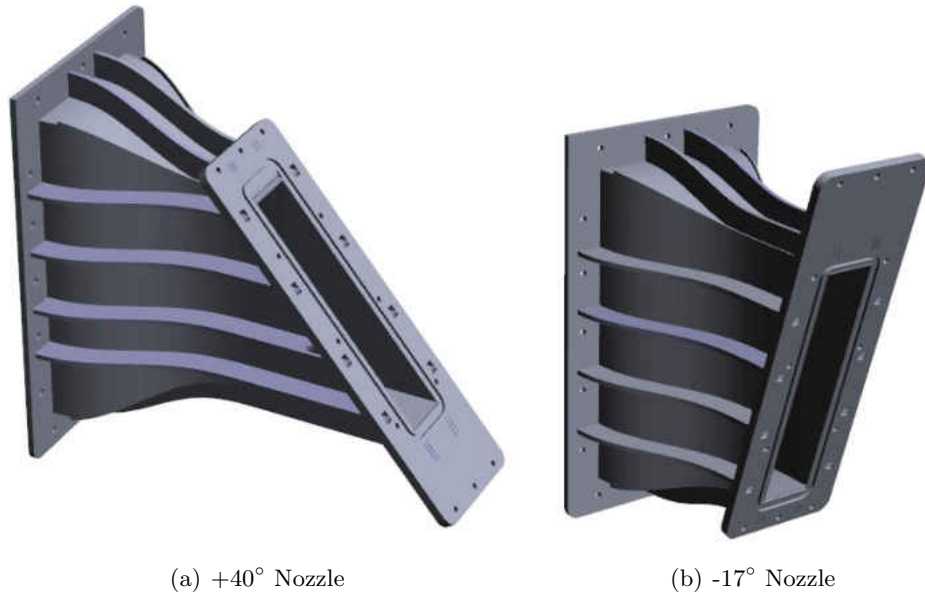
Fig. 3.5: CAD Models Showing (a) 40° Nozzle and (b) -17° Nozzle.

Calculations of the flow field through a double–contraction nozzle appended to the corresponding blade cascade were performed at three different inlet angles using Fluent 6.3. The results of the calculations were compared to those of a two–dimensional straight nozzle to ensure that the optimal nozzle contours were chosen. The boundary conditions of the different simulations were set such that a Mach number of 0.75 is achieved at the quarter axial chord downstream of the blade trailing–edge. The nozzle contours were validated by verifying the pressure loadings on the investigated blades at the symmetry plane ($z = 0$), and at 0.0127 m and 0.0254 m away from the symmetry plane. Figure 3.6(a) and Figure 3.6(b) show the comparisons of the simulations for a 40° nozzle, and Figure 3.7(a) and

Figure 3.7(b) show the comparisons of the simulations for -17° nozzle after post–processing of the CFD results. It can be seen that similar pressure loadings on blade 2 and blade 3 were obtained when compared to the two–dimensional simulation, at various span locations ($z = 0$ and $z = 0.0127$ m).
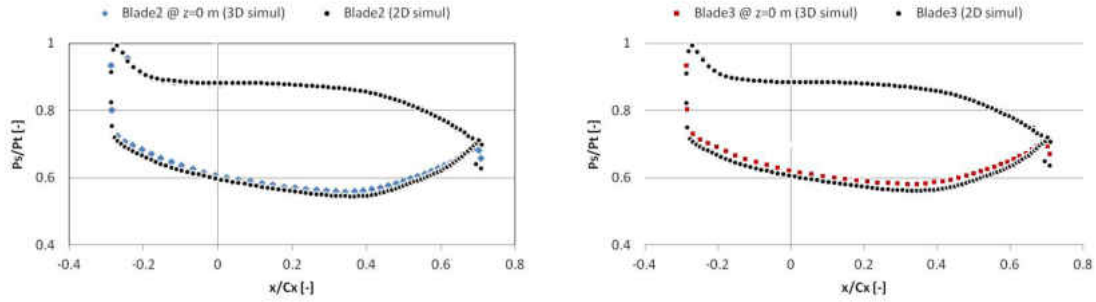
(a) Pressure Distribution on Blade 2

(b) Pressure Distribution on Blade 3

Fig. 3.6: Pressure Distribution on (a) Blade 2 and (b) Blade 3 from +40° Nozzle
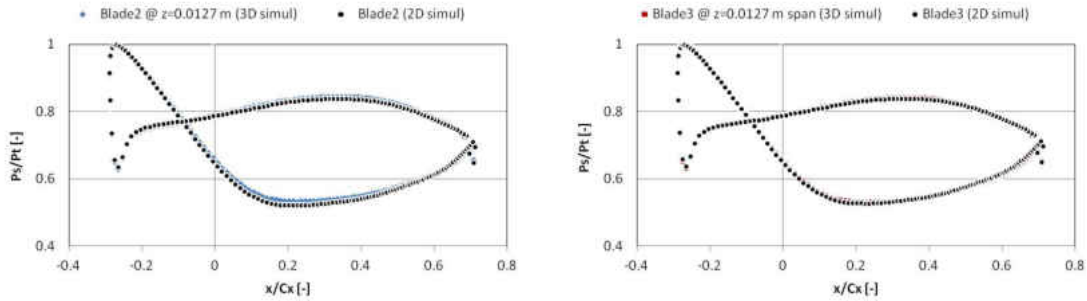
(a) Pressure Distribution on Blade 2

(b) Pressure Distribution on Blade 3

Fig. 3.7: Pressure Distribution on (a) Blade 2 and (b) Blade 3 from -17° Nozzle

3.4   Modular Blade–Cascade

The modular blade–cascade is a two–dimensional scaled representation of the second rotor (rotor 2) of the selected four–stage VSPT. The blade geometry along with flow–blocks for 40° and -17° inlet angles are shown in Figure 3.8. The test section is a six–blade and five–passage linear cascade, with an adjustable tailboard to help control the exit flow periodicity. The curvatures applied on the flow–blocks and the tailboard are streamlines obtained from two–dimensional CFD calculations.

The top plate of the modular cascade is equipped at its inlet with two Kiel probes to measure the total pressure, and two total temperature probes. The probes are positioned at the mid–span to measure the free–stream properties. Each total pressure and temperature probe is paired with a customized boundary layer rake for inlet boundary layer measurements. The probes are oriented in the direction of the incoming flow, for each angle, to minimize flow disturbance and stay within the yaw range limits of the probe insensibility. A polycarbonate window is placed on the top plate for blade visibility. The bottom plate of the modular cascade is instrumented with two rows of thirty inlet static pressure taps and thirty exit static pressure taps, located at quarter axial chord upstream of the leading–edge and downstream of the trailing–edge, respectively. The flow quality of the test section (inlet uniformity and exit periodicity) is assessed from measurements through the static pressure taps, and can be adjusted by two 3.18 cm ($1\frac{1}{4}''$) gate valves connected to the flow–blocks on each side of the cascade.

A set of quadruple blades is inserted through the opening incorporated in the bottom plate. Two sets of blades were made and instrumented for measurements: a set for the mid–span and quarter–span pressure distributions, and another for mid–line pressure and temperature measurements. Both sets were made virtually identical so they can be interchanged with ease for the multiple tests. The two set of blades are made out of a stereolithography resin, commercially known as Somos NanoTool, from a three–dimensional layering process. The stereolithography process is adequate for good smooth surface quality, and the NanoTool provides ideal material properties for wind tunnel models. The incidence–tolerant blade has an inlet metal angle of 34.2° and an exit metal angle of -54.97° relative to the axial direction. The scaled blades are spaced 4.89 cm (1.923") with 5.08 cm (2") span. The leading–edge and the trailing–edge diameters of the blade are 5.67 mm and 1.24 mm, respectively.

3.5   Instrumented Blades for Heat Transfer and Pressure Measurements

The set of quadruple blades for heat transfer tests, represented in Figure 3.8, had the middle two blades (blade 2 and blade 3) instrumented for surface temperature and pressure distributions. Each blade was manufactured with 36 holes of 0.79 mm ($\frac{1}{32}''$) in diameter,
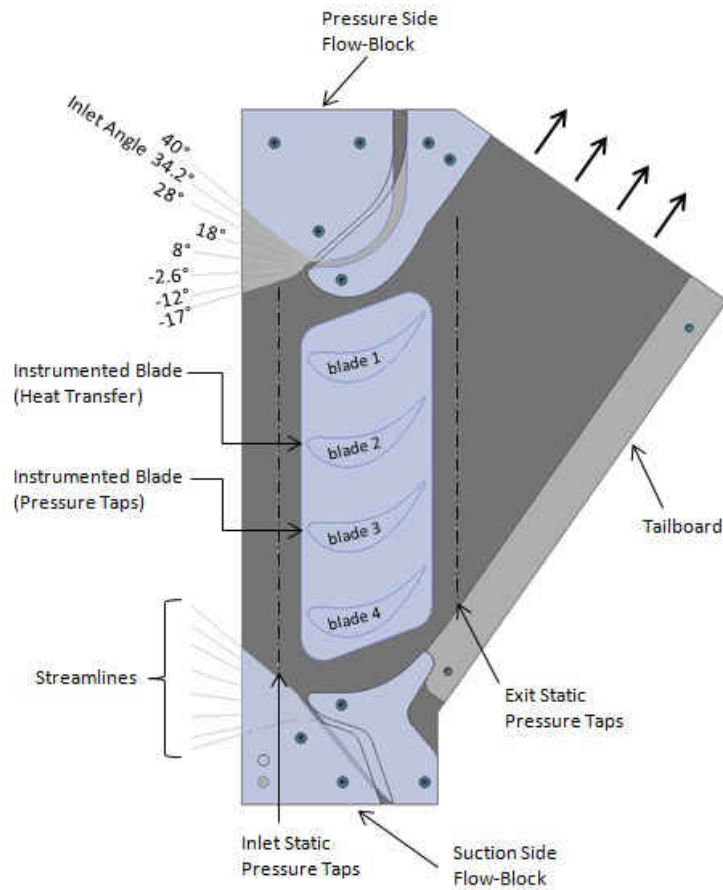
Fig. 3.8: Schematic of the Incidence–Tolerant Cascade Showing Arrays of Inlet Streamlines and Measurement Locations.

drilled 5.08 cm (2") deep from the base of the set of blades. The 36 pressure holes were intersected perpendicularly by 36 other pressure taps, of same the diameter, drilled along the blade surface. Brass tubes of 0.79 mm in diameter were fed through the bottom holes on blade 3, and positioned such that the two–part epoxy (Loctite epoxy product), used to seal the holes around the brass tubes, would not clog the tubes. The open ends of the brass tubes were soldered to barbed fittings to facilitate their connection to the data acquisition system, through flexible clear tubing (Tygon tubing). Figure 3.9(a) and Figure 3.9(b) show the side and bottom pictures of the quadruple heat transfer blades. The temperature distribution was acquired on blade 2 by the use of 36 type–K thermocouples. The thermocouples were introduced through the 0.79 mm bottom holes and carefully positioned

such that the thermocouple beads were not recessed nor protruded from the surface orifices on blade 2. Omegabond 101 was used to cement the thermocouple beads in place along the blade surface, and the Loctite epoxy was also used to seal the bottom holes around the thermocouple wires. A 0.023 mm thick Inconel foil, cut–down to the blade dimensions, had both lengthwise extremities soldered to copper bus bars. After the Omegabond was fully cured, the Inconel foil was then meticulously placed around blade 2, and the bus bars would come to rest in the notches incorporated on the blade to present a virtually seamless profile.

The quadruple pressure–blades were similar to the heat transfer blades, with the exception that blade 2 was then instrumented for pressure measurements and the surface pressure taps on blade 3 were staggered for mid–span and quarter–span pressure measurements. The staggered arrangement on blade 3 was meant to investigate possible influence of the blade end–wall to the surface pressure distribution.

3.6   Data Acquisition System

The acquisition system developed at the University of North Dakota is a computer based system. A description of the system used for the original compressible flow facility is provided in Mihelishs thesis. The computer used in this investigation is equipped with an Intel Celeron 1.7Ghz processor and 80 GB hard–drive to gather large amount of data. The desktop CPU contains a IEEE–488 interface card, which serves as a liaison between the computer and a HP 3497A control unit, and a DIO–48 board that enable the computer to operate the 48 solenoid valves of the pressure scanner.

The automated system for pressure measurements was composed of 48 solenoid valves, 4 Rosemount differential and absolute pressure transducers calibrated to read pressure in the ranges of 0 to 0.12 kPa, 0 to 3.73 kPa, 0 to 34.34 kPa, and 0 to 103.4 kPa. Four of the forty eight solenoid valves were used to measure the total pressure at the inlet of the cascade, and therefore the Kiel probes were connected to two of these four valves. Total pressure conditions were obtained by connecting the four valves in parallel to the absolute pressure transducer (calibrated from 0 to 103.4 kPa) and to the high pressure sides of the three differential pressure transducers. The remaining 44 valves were connected to the low
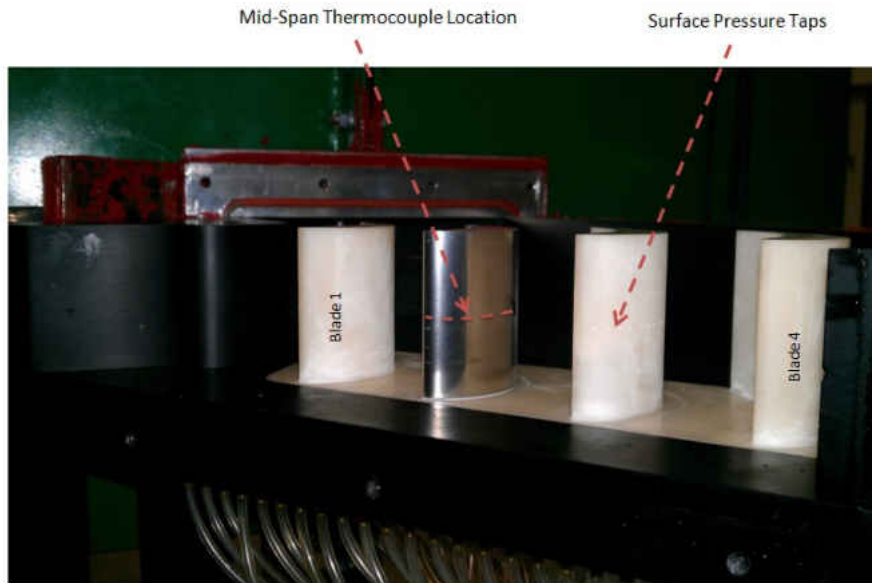
(a) side view of HT blade
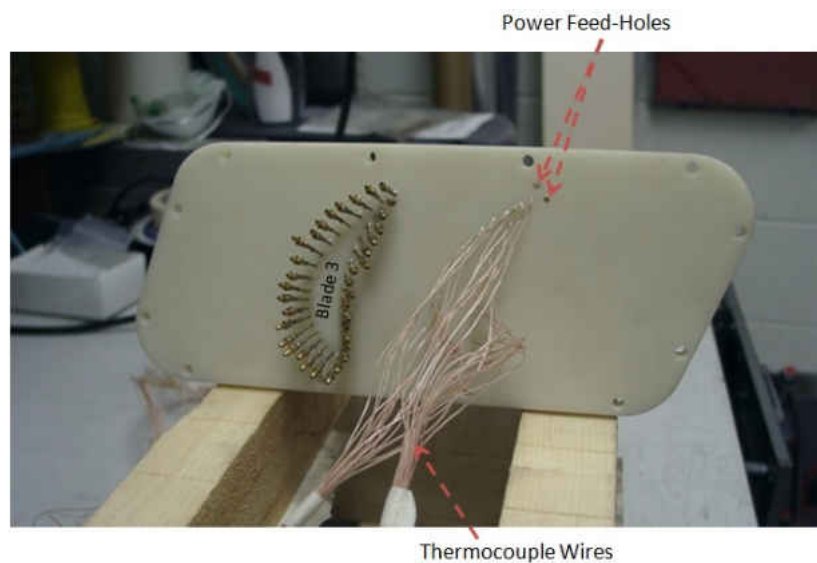
(b) bottom view of HT blade

Fig. 3.9: (a) Side and (b) Bottom Views of the Heat Transfer Blade.

pressure sides of the differential pressure transducers. Static pressure measurements at the inlet and exit locations and along the blade surface as well, were outputted in terms of pressure differential referenced from the inlet total pressure. Preliminary tests of the facility have identified two faulty valves which had been replaced to available ones prior to

the present investigation. An additional malfunctioning valve had been noticed during the first tested configurations, and had been replaced for the remaining of the investigations. The corresponding pressure read by the malfunctioning valve will be indicated in the Data Analysis section.

The 36 thermocouples distributed on the heat transfer blade surface were connected to existing instrumentation equipments designed to perform the heat transfer testing. A picture of the compressible flow rig, set up for heat transfer test at the -2.6° inlet flow angle and the high turbulence condition, is shown in Figure 3.10. The thermocouples, including the total temperature probe, were referenced to an ice–bath temperature and connected to a 90 terminal jack–panel. The terminal panel input the measured temperatures through a constant temperature junction box, which output corresponding thermoelectric potentials to the HP 3497A control unit. The Inconel foil, dissipating uniform heat flux on the surface of blade 2, was connected to a HP 6269B DC power supply through the bus bars. The power supply can produce a voltage ranging between 0 to 40V, with a current ranging from 0 to 50 A. The large current output was monitored using a 24.39 mA shunt resistor connected to the positive pole of the power supply, and enabled direct measurement from the control unit.

The pressure and temperature measurements were acquired with an existing Quick-Basic program updated for this investigation and used in MS–DOS prompt. The updated program required the user to first zero the four pressure transducers, such that reference pressures can be attained, before accessing the program menu. The menu presented the user with the option to monitor the wind tunnel conditions, which included the total pressure and temperature, exit static pressure, exit velocity, exit Mach number, the blade exit Reynolds number, and the supplied current and power. Other options of the program menu allowed the user to acquire inlet and exit static pressure surveys, blade surface pressures, inlet boundary layer, perform a quick scan of the thermocouples and acquire the blade temperature distributions at steady state condition. The tests performed at a Reynolds number of 568,000 and Mach number of 0.35 required the wind tunnel to operate above
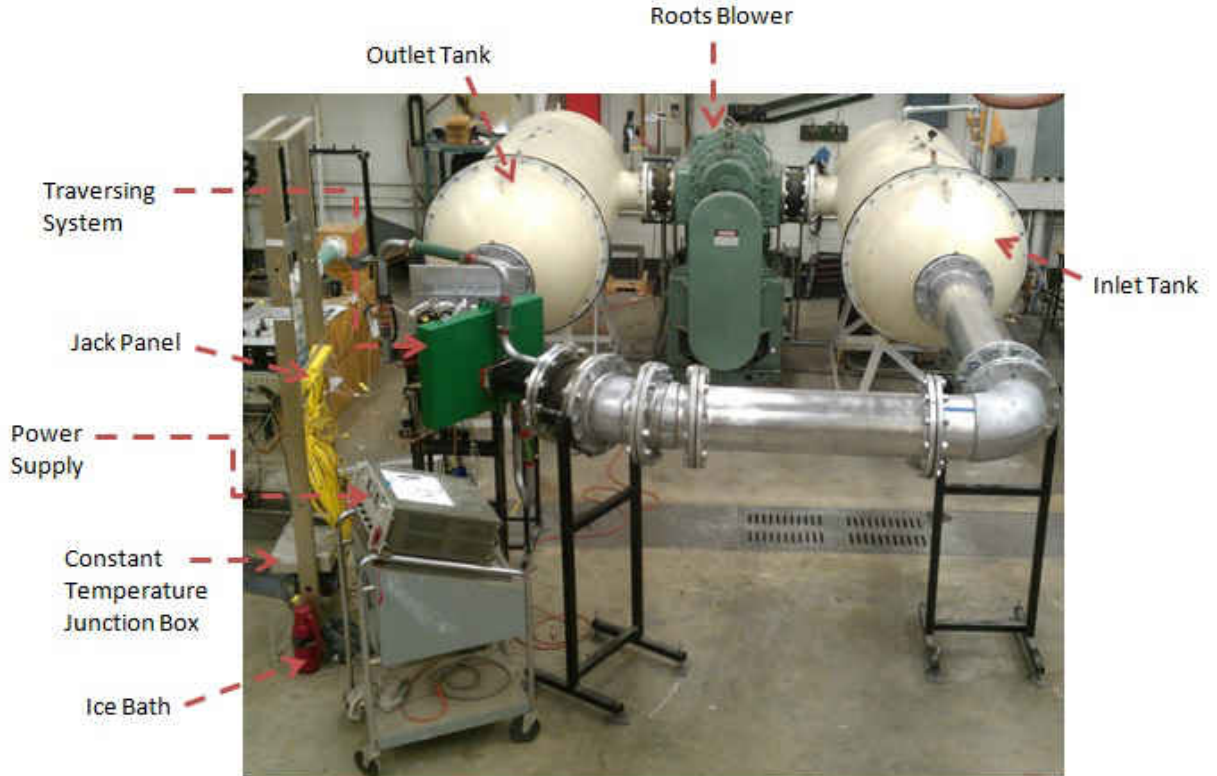
Fig. 3.10: Compressible Flow Facility Set up for Heat Transfer Tests at -2.6° Inlet Flow Angle.

atmospheric pressure. A separate QuickBasic program was updated for this flow condition to acquire the necessary pressure and temperature distributions.

3.7 Data Analysis

The set of data required to assess the flow quality and perform steady state heat transfer analyses involved the acquisition of inlet and exit static pressure distributions, pressure distributions on blade 2 and blade 3 for the pressure–blades, and temperature and pressure distributions on blade 2 and blade 3 for the heat transfer–blades. Eight incidence angles simulated by the eight different slanted nozzles were tested for two turbulence levels, with each turbulence level investigated for Reynolds numbers of 50,000, 66,000, 228,000, and 568,000 at the Mach number of 0.72, and Reynolds numbers of 228,000 and 568,000 at Mach number of 0.35. The values of the investigated incidence angles can be determined from the inlet flow angles using Equation 3.7.1. A summary of the different incidence angles

used the heat transfer investigations can be seen in Table 3.1.

$$i = \beta_1 - 34.2°$$

(3.7.1)

The flow conditions at which the pressure and temperature distributions were acquired, are listed in Table 3.2. Complete sets of data were acquired for incidence angles of $+5.8°$ (cruise point), $0°$, and $-36.8°$ (take–off point). For the remaining angles, only the pressure and temperature distributions on blade 2 were acquired for flow conditions requiring sub–atmospheric wind tunnel operation. The output data obtained in the present investigations were gathered in Excel spreadsheet format for analyses.

3.7.1   Inlet and Exit Static Pressure Distributions

The 3.18 cm gate valves were conveniently opened for an adequate uniform flow at the cascade inlet. The inlet pressure distributions were measured by the 30 inlet static pressure taps. The large incidence swing would cause the first few taps (for the positive inlet angles) or the last few taps (for the negative inlet angles) to be obstructed by the flow–blocks. However, the obstructed pressure taps were not in proximity of the investigated blades, and the assessment of flow quality at the cascade inlet was not influenced. Figure 3.11 shows the inlet distributions, obtained from 27 pressure taps, in terms of the isentropic Mach numbers.   The local Mach number was calculated from the measured inlet total

Table 3.1: Investigated Incidence Angles

Inlet Angle(β_1)	Incidence Angle (i)
40°	5.8°
34.2°	0°
28°	-6.2°
18°	-16.2°
8°	-26.2°
-2.6°	-36.8°
-12°	-46.2°
-17°	-51.2°

Table 3.2: Wind Tunnel Flow Test Conditions

Reynolds Number(Re_C)	Exit Mach Number (Ma,ex)	Turbulence Level
568,000	0.72	Low Turbulence
228,000	0.72	Low Turbulence
66,000	0.72	Low Turbulence
50,000	0.72	Low Turbulence
568,000	0.35	Low Turbulence
228,000	0.35	Low Turbulence
568,000	0.72	High Turbulence
228,000	0.72	High Turbulence
66,000	0.72	High Turbulence
50,000	0.72	High Turbulence
568,000	0.35	High Turbulence
228,000	0.35	High Turbulence

pressure and local static pressure using the following isentropic relation:

$$
M = \sqrt{\frac{2}{\gamma - 1} \left[\left(\frac{P_t}{P_s} \right)^{\frac{\gamma-1}{\gamma}} - 1 \right]}
\tag{3.7.2}
$$

where P_t is the inlet total pressure, P_s is the local static pressure, and $\gamma = 1.4$ is the ratio of specific heats.

The exit conditions were evaluated from an exit pressure tap chosen from the 30 exit pressure taps located at the quarter axial chord downstream of the blade trailing–edge. Figure 3.12 shows the isentropic Mach number distribution at the cascade exit. The ideal exit pressure tap was determined by comparing its measured value to the average of the entire distribution peak values. Its location was further restricted to the pressure taps spanning in the passage between blade 2 and blade 3, and being away from the airfoil wakes. The exit conditions, calculated from the QuickBasic program and including the exit Mach number and velocity and the Reynolds number, were evaluated from the static pressure tap located at 0.24 m for the entire set of wind tunnel measurements. Figure 3.12 shows measurements obtained from 28 exit pressure taps. The adjustment of the tailboard during the cascade assemblage obstructed the first 2 pressure taps which are not shown.
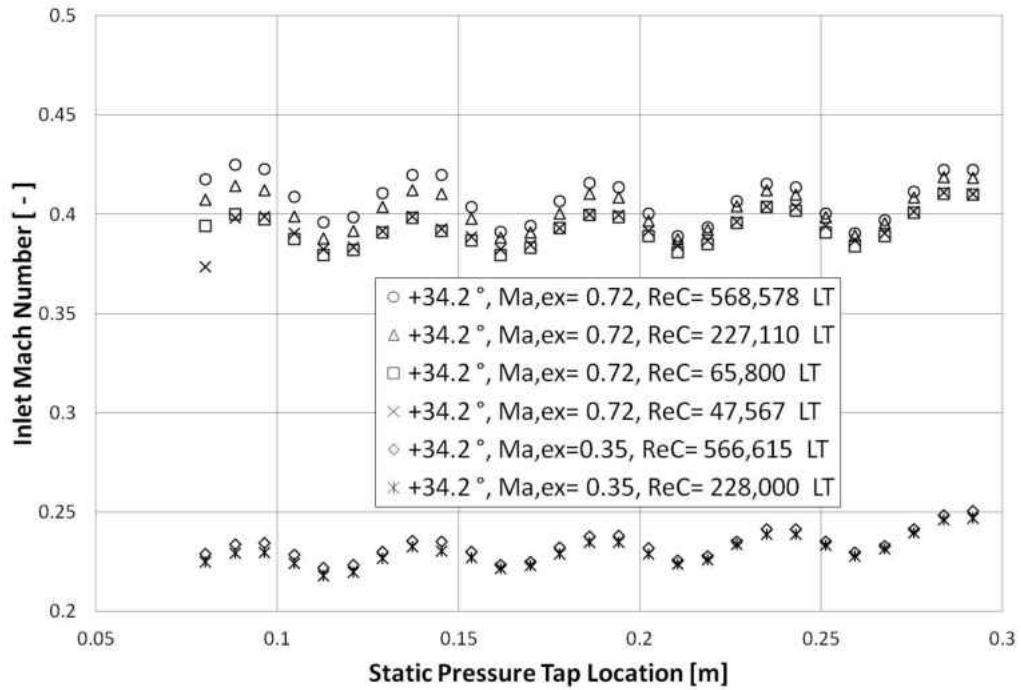
Fig. 3.11: Inlet Mach Number Distributions at 0° Incidence Angle and Low Turbulence Level.

3.7.2 Blade Pressure Distributions

The pressure distributions, measured from the pressure taps embedded in the investigated blades, are presented in terms of the isentropic Mach numbers calculated from Equation 3.7.2. Figure 3.13 shows the Mach number distribution for the different flow conditions on blade 2, at the zero incidence angle and low turbulence level. The surface arc lengths, of the mid–span pressure tap locations, were obtained and normalized with respect to the airfoil true chord. It is depicted in Figure 3.13 that negative abscissa values represent the pressure surface and the positive values represent the suction surface of blade 2 profile. The zero normalized value represents the position of the pressure tap closest to the true leading–edge.

Two–dimensional Fluent calculations were performed for the zero incidence case, as a method to validate and improve the experimental data acquisition. The structured grids
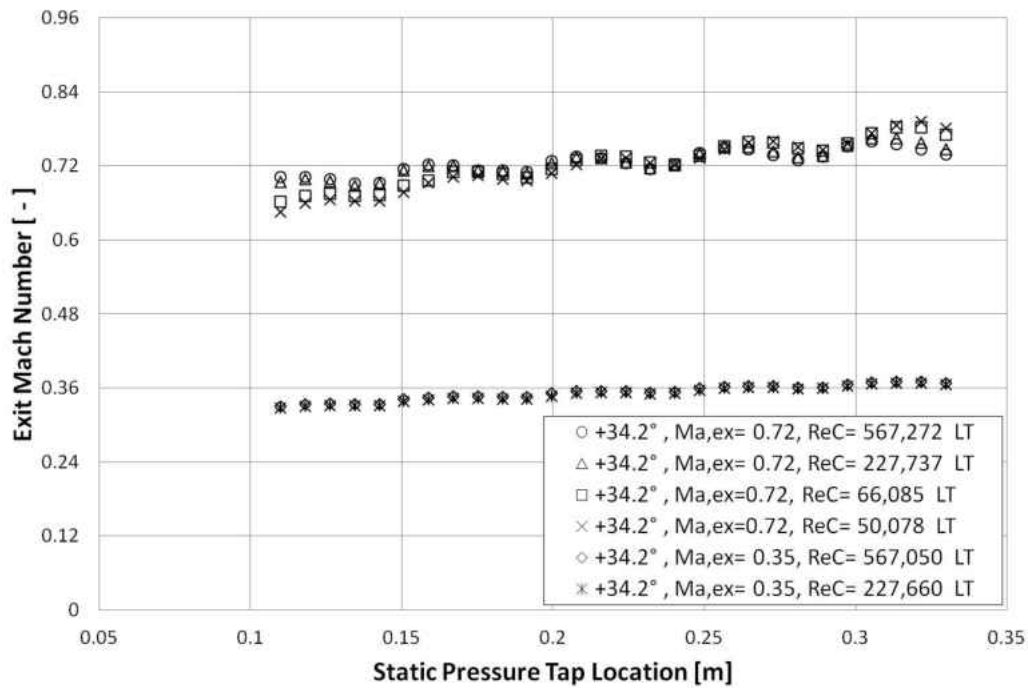
38

Fig. 3.12: Exit Mach Number Distributions at 0° Incidence Angle and High Turbulence Level.

were generated for a geometry modeling the 4 full–blade profiles with periodic streamlines applied at the mid–passages. The simulation was defined for density–based implicit solver with the boundary conditions set to match the wind tunnel conditions for the Reynolds number of 228,000 at an exit Mach number of 0.72. A Realizable $k-\varepsilon$ viscous model was used for the compressible flow simulation. The simulation predicted an exit metal angle of -54.65° with exit Mach number of 0.70 at the quarter axial chord location from the blade trailing–edge. The obtained CFD prediction turned out to be of an adequate fidelity and useful to be compared to the experimental data, nonetheless. As it can be seen in Figure 3.13, the Mach number distributions for the highest Reynolds number conditions show good agreement with the CFD prediction. It was found that the measurements obtained from the pressure tap located at the normalized distance of 0.35 (suction surface) were questionable. Later measurements from the same pressure tap connected to a different solenoid valve confirmed

that the initial solenoid valve used was faulty. However, it was observed that the faulty valve did not significantly alter the interpretation of the measurements for the different incidence angles in which it was used.
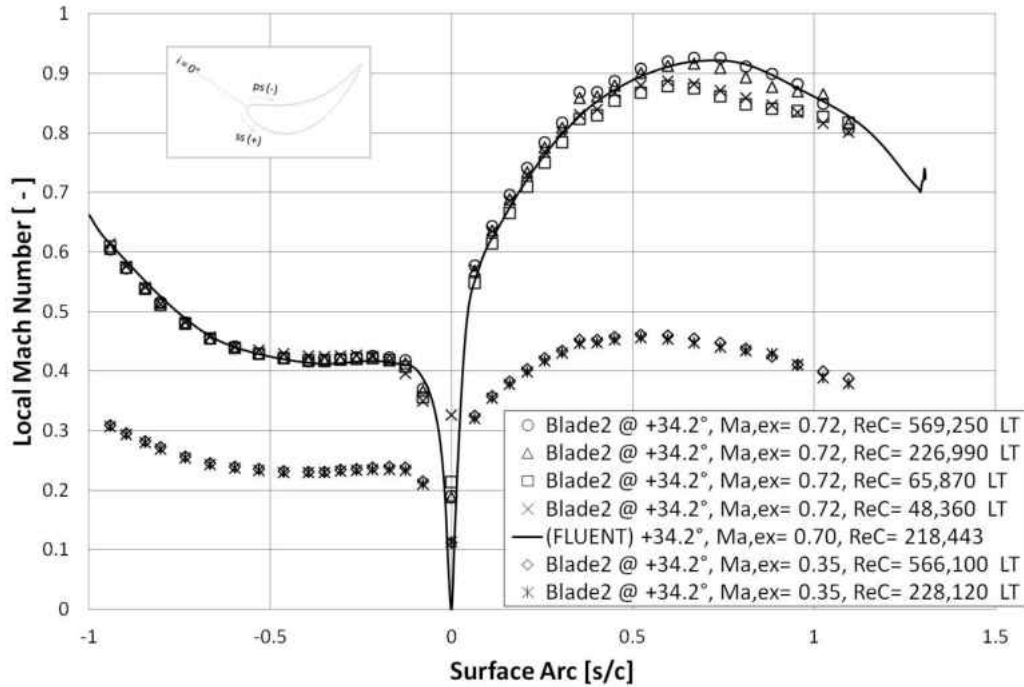

Fig. 3.13: Blade 2 Surface Mach Number Distributions at 0° Incidence Angle and Low Turbulence Level.

The good flow quality inside the blade cascade was further supported by the periodicity obtained at the various configurations. Figure 3.14 shows the surface Mach number distributions for blade 2 and blade 3 at the Reynolds number of 228,000. On the pressure side, there is evidence that the two blades are subjected to virtually identical loads up to leading–edge region. On the suction side, the two profiles present discrepancy downstream of the over–speed region. It is possible that the boundary layer blockages might slightly differ between the two corresponding flow passages.

3.7.3   Heat Transfer Analysis

The steady state heat transfer measurement involved initially acquiring the adiabatic or recovery surface temperatures prior to acquire the surface temperatures with the heated
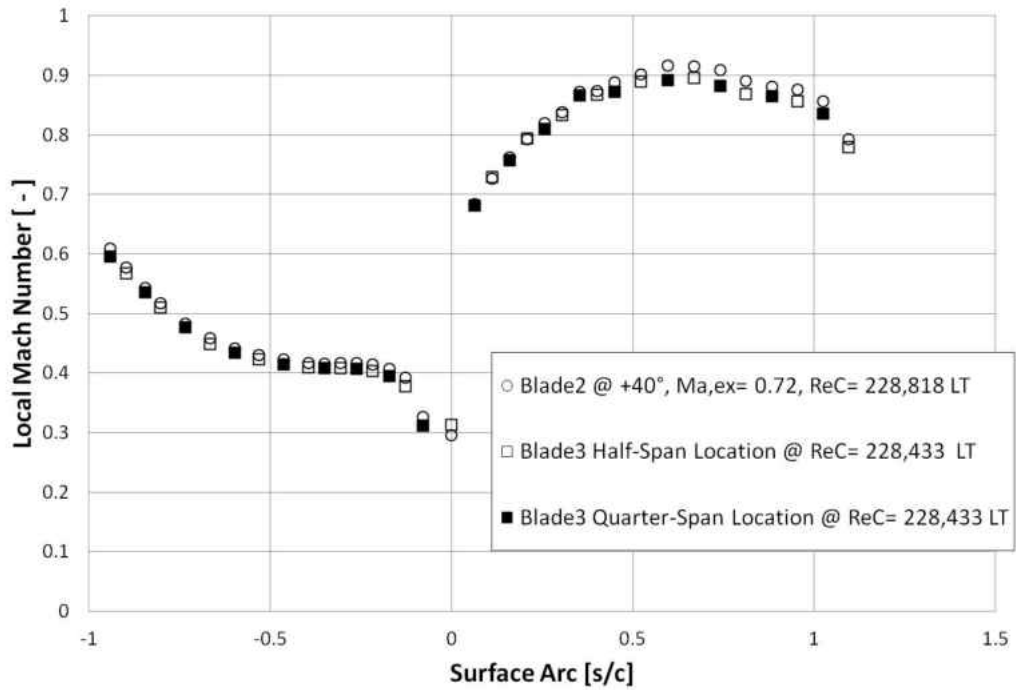
Fig. 3.14: Surface Mach Number Distributions on Blade 2 and Blade 3 at +5.8° Incidence Angle and $Re_C = 228,000$.

Inconel foil. In general, the heat transfer from the heated blade is a combination of the conductive, convective, and radiative heat fluxes. The net heat flux, necessary to obtain the heat transfer coefficient, was determined from the dissipated heat flux less the radiation heat loss and corrected for the heat conduction through the NanoTool material:

$$q'' = \frac{V \cdot I}{A} - \epsilon \sigma \left(T_S^4 - T_\infty^4 \right) - q''_{cond} \tag{3.7.3}$$

where A is the Inconel foil surface area, $\epsilon = 0.21$ is the emissivity of the foil, σ is the Stefan–Boltzmann constant, T_S is the surface temperature, and T_∞ is the free–stream temperature. The local heat transfer coefficient was derived from Newton's law of cooling:

$$h = \frac{q''}{\Delta T} \tag{3.7.4}$$

41

and Stanton number was calculated from the obtained heat transfer coefficient:

$$St = \frac{h}{\rho V c_p} \tag{3.7.5}$$

where the density ρ, velocity V, and specific heat c_p are the flow conditions at the exit. The recovery wall temperature is generally considered as the driving temperature for heat transfer on an airfoil. When heat is transferred from blade wall to the surrounding gas, the recovery temperature is then the reference temperature that is necessary to evaluate the heat transfer coefficient. The differential temperature ΔT between the adiabatic and heated conditions was calculated using Equation 3.7.6:

$$\Delta T = T_s - T_{s,aw} + (T_t - T_{t,aw}) \tag{3.7.6}$$

where T_s is the heated surface temperature, and T_t is the total inlet temperature for the heated surface case. The measured recovery temperatures were compared to laminar recovery temperature distributions based on the recovery coefficient $r = Pr^{1/2}$ and to turbulence temperature distributions based on the recovery coefficient $r = Pr^{1/3}$, to estimate the effect of conduction and be able to accurately correct its values. Comparison obtained will be presented and discussed in the result section, and additional plots can be found in Appendix F.

3.8   Finite Difference Conduction Model

A finite–difference conduction model was developed to obtain the surface heat flux due to conduction through the blade. The blade nodal network, shown in Figure 3.15, is a two–dimensional system composed of 204 nodes covering the entire blade section in a well determined discrete scheme. The Inconel foil, used for heat dissipation on the blade surface, did not cover the tip of the trailing–edge. Therefore, a small portion of the trailing–edge was modeled as a heat sink to reduce the temperature distribution uncertainties in that region. The steady–state conduction analyses were performed from the measured boundary conditions, and approximating the majority of the grids as planar walls. Analyses in the leading–edge region were performed with the assumption of a radial system. The conduction

model not only corrected the net heat flux, but it also provided correction to the measured adiabatic wall temperature and heated surface temperature.
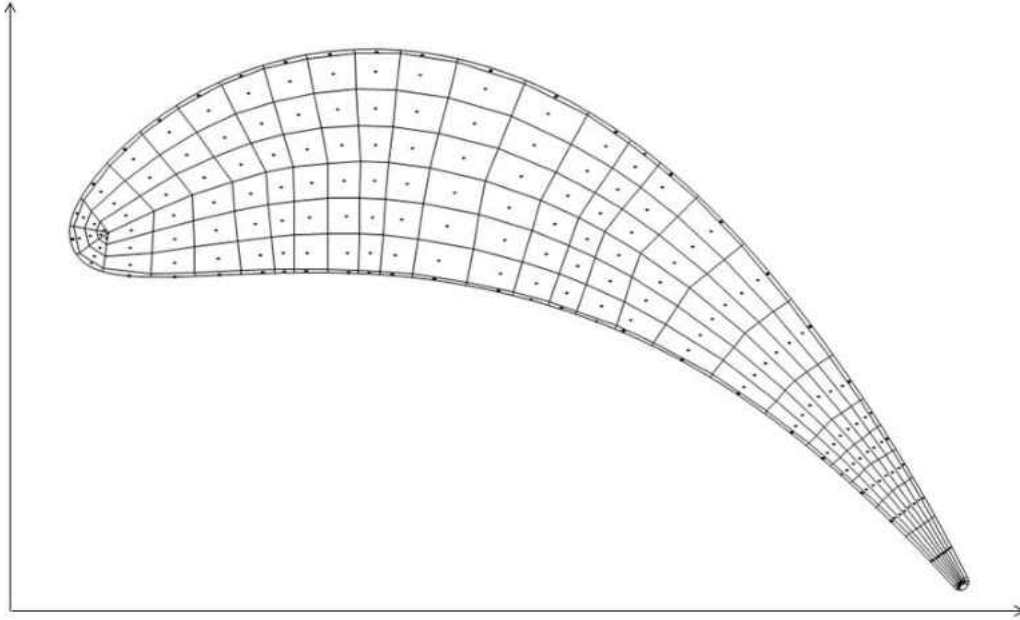

Fig. 3.15: Finite–Difference Model for Conduction Analyses.

3.9   Data Uncertainties

Uncertainties of the heat transfer data were estimated from the root–sum–square method described by Moffat [48]. The uncertainties of the voltage and the current through the shunt resistor were about $+/-$ 0.1% and $+/-$ 2%, respectively. The Inconel foil was cut–down to the blade dimensions with an uncertainty of about $+/-$ 0.6%. The dissipated heat flux had a local uncertainty of about $+/-$ 3%, and the measured adiabatic wall temperature and the heated surface temperature had an uncertainty of $+/-$ 0.2 °C. It was determined that the developed conduction model calculated the conduction through the blade with an estimated uncertainty of $+/-$ 25%. The radiative heat flux in the modular–cascade was also determined with an uncertainty of $+/-$ 25%. The nominal uncertainty in the heat transfer coefficient was estimated to be $+/-$ 5% for the highest Reynolds number. Larger uncertainties are expected for lower Reynolds number heat transfer data.

CHAPTER IV

EXPERIMENTAL RESULTS

This chapter discusses the results of the pressure measurements and heat transfer distributions on the incidence–tolerant blade. The blade loadings and the heat transfer are presented in terms of the local midline Mach number and the Stanton number distributions, respectively. The following results will be presented such that the effect of the Reynolds number, turbulence intensity, and the angle of incidence can be clearly identified. Additional results, not presented in this Chapter, can be seen in the Appendices. An indication of the flow quality in the cascade was obtained at the cascade inlet and exit, as shown in Figure 3.11 and Figure 3.12, in Chapter III. The inlet Mach number distribution indicated a consistent and better flow behavior from the pressure tap 14, located at 0.16 m, to the last pressure tap, located at 0.29 m. This range of pressure taps covered the flow region around blade 2. The Exit Mach number distribution indicated good periodicity over the entire cascade exit. The results of the inlet and exit measurements ensured good flow quality for heat transfer tests. Heat transfer experiments can provide insight into the state of the blade boundary layer. However, the heat transfer results alone are not sufficient to properly indicate the state of the boundary layer. The combination of the blade loading and the heat transfer data is necessary for better interpretation of the results.

4.1   Blade Loading Profiles

The pressure distributions on blade 2 were measured for each of the incidence angles listed in Table 3.1 at the different conditions listed in Table 3.2. The pressure distributions were obtained to calculate the corresponding isentropic Mach numbers using Equation 3.7.2. The non–dimensional values were necessary to effectively compare results of the different configurations.

The Mach number distributions at the incidence angle of $+5.8°$ ($+40°$ inlet angle) are

shown in Figure 4.1. On the pressure surface, the flow accelerates from the leading–edge to maintain a steady progression to the throat of the cascade passage, at which a gradual acceleration to the trailing–edge, in presence of a favorable pressure gradient, is observed. On the suction surface, the presence of a favorable pressure gradient allows the flow to accelerate to its peak value, followed by a flow deceleration to the trailing–edge, due to the presence of an adverse pressure gradient. The true stagnation point appears to be near the zero location and on the pressure side. There is no apparent flow separation observed on the pressure surface of this low turbulence configuration. On the suction surface, there is an apparent change of the flow behavior, downstream of the peak Mach number, for the two lowest Reynolds numbers. This change suggests a region of flow separation starting near the pressure tap located at the normalized distance of 0.596 cm, with an apparent longer separation zone observed at the lowest Reynolds number.
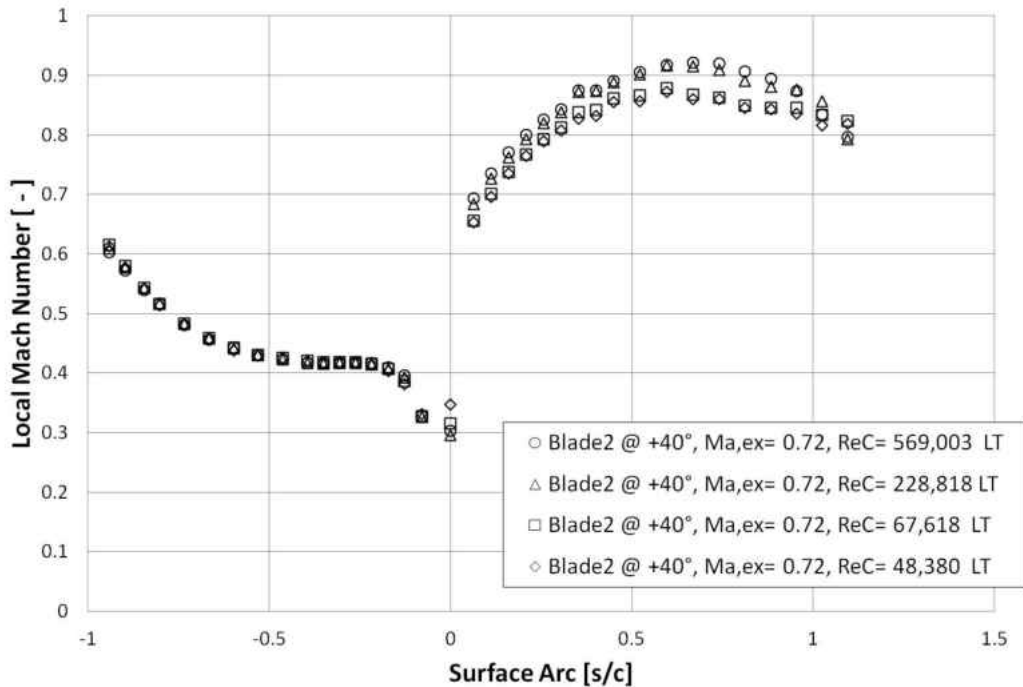

Fig. 4.1: Blade 2 Surface Mach Number distributions at +5.8° Incidence Angle and Low Turbulence Level.

4.1.1 Effect of Reynolds number

The four Reynolds numbers obtained for this experiment are based on the blade true chord and the cascade exit conditions. The investigated Reynolds numbers are 50,000, 66,000, 228,000, and 568,000. Figure 4.2 shows the Mach number distributions on blade 2 at the exit Mach number of 0.72 for the different Reynolds numbers, at the incidence angle of -36.8° (-2.6° inlet angle) for the low turbulence level. In this configuration, a rapid over–speed region can be seen downstream the leading–edge on the pressure surface, followed by a flow deceleration and a gradual acceleration to the trailing–edge, successively. The two lowest Reynolds numbers display a laminar separation bubble region downstream of the blade leading–edge. As the Reynolds number increases, the over–speed gradient steepens with the laminar separation region diminishing to what appears to be fully attached flow. It is expected that the heat transfer would be suppressed in this region, for the two lowest Reynolds numbers. On the suction surface, it appears there is flow separation downstream of the peak velocity region for the two lowest Reynolds numbers. Multiple locations of the peak Mach numbers are observed, for this low turbulence case, in a pattern suggesting that the location of the point of separation moves toward the trailing–edge as the Reynolds number increases. The apparent formation of a laminar separation bubble was also noticed on the pressure surface for other incidence configurations. Some of these Mach number distributions can be seen in the Appendix C. It appears that as the incidence angle moves further toward the negative value, the higher Reynolds numbers also display regions of laminar separation bubble on the pressure surface. As it can be seen in Figure 4.3 the four Reynolds numbers show a region of separation bubbles on the pressure side for the incidence angle of -51.2° (-17° inlet angle).

4.1.2 Effect of Free–Stream Turbulence

The two turbulence conditions developed for this investigation were estimated at 0.47 % for the low turbulence intensity (LT) and 5.03 % for the high turbulence intensity (AC). Figure 4.3 shows the Mach number distributions on blade 2 for the two turbulence levels at the exit Mach number of 0.72 and incidence angle of -51.2° (-17° inlet angle). The
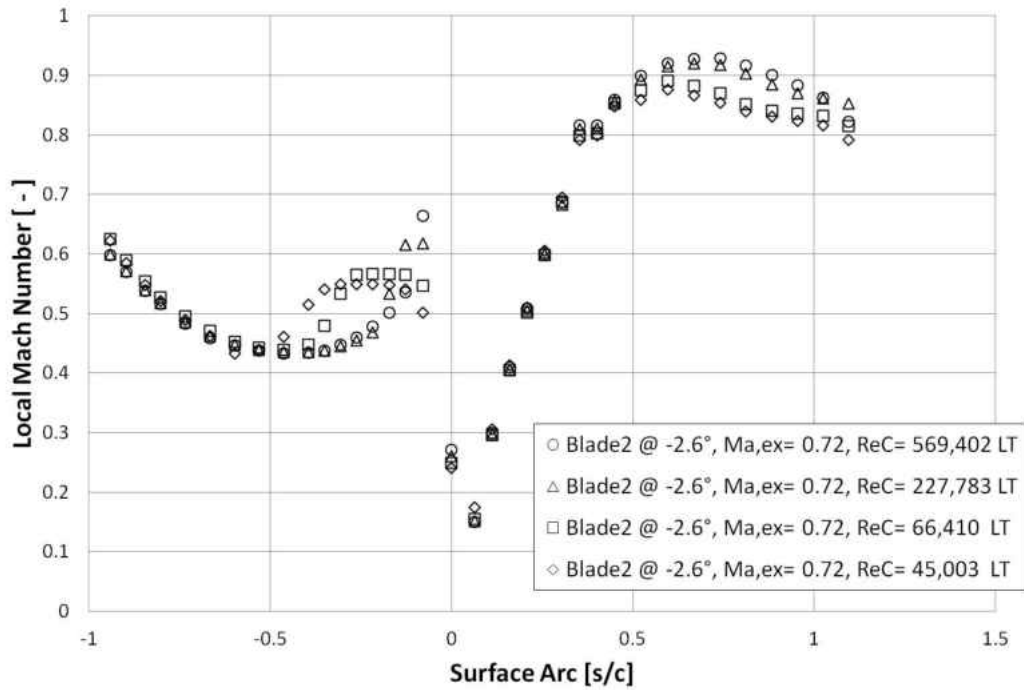
Fig. 4.2: Blade 2 Surface Mach Number distributions at -36.8° Incidence Angle and Low Turbulence Level.

open symbols represent the low turbulence, while the closed symbols represent the high turbulence conditions. It is interesting to see how the moderate magnitude of the intensity generated by the mock aero–derivative combustor has a greater effect on both the pressure and suction surfaces of the blade. On the pressure surface, it can be noted that region of laminar separation is wider as compared to the -36.8° incidence angle case. There is evidence that the high turbulence level impedes formation of the laminar separation for the Reynolds numbers of 50,000, 66,000, and 228,000, and a complete elimination at the Reynolds number of 568,000. It is expected that heat transfer results will show an increase of the local heat transfer as the turbulence level increases. On the suction surface, a separation zone is apparent downstream of the over–speed region for the low turbulence case. For the high turbulence case, it appears that the high free–stream turbulence has facilitated a smoother boundary layer transition downstream of the peak velocity region to the trailing–

edge, for the two highest Reynolds numbers. The closed symbols representing the two lowest Reynolds also show improvement of laminar to turbulent flow transition. However, it seems that a separation zone still exists in a mild adverse pressure region for the two lowest Reynolds numbers.
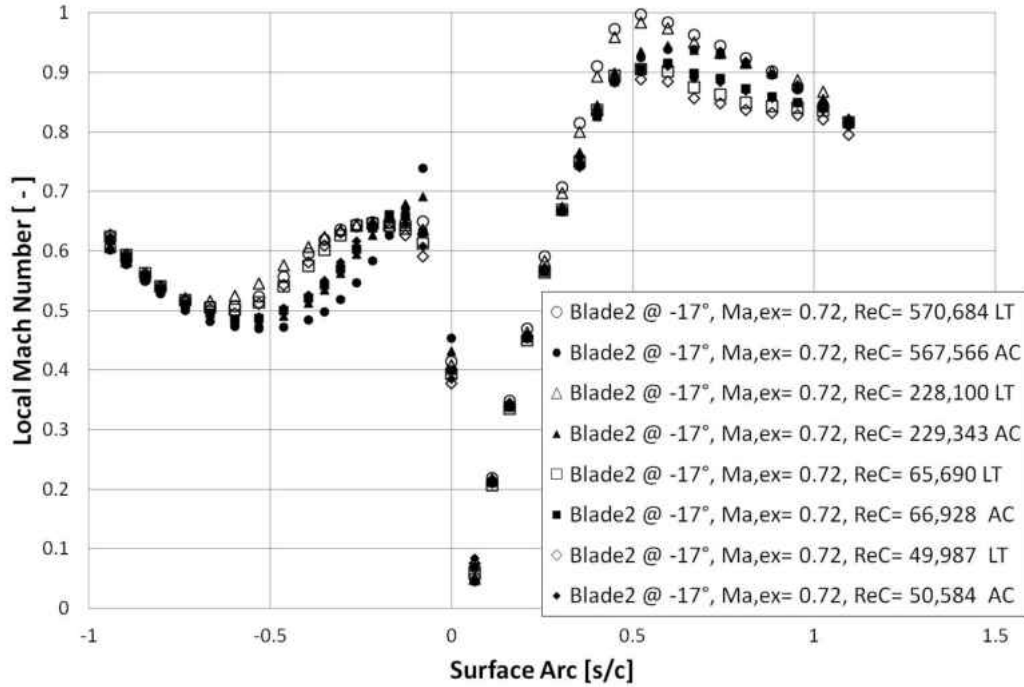

Fig. 4.3: Effect of Free–Stream Turbulence on Blade 2 Surface Mach Number distributions at -51.2° Incidence Angle.

The influence of the high free–stream turbulence was not apparent for the incidence angle of +5.8°, +0°, and -6.2° (+28° inlet angle). Figure 4.4 shows the negligible effect of the free–stream turbulence for the +5.8° incidence angle case. It can be seen that the open and closed symbols are virtually identical within their respective Reynolds number values, on both pressure and suction surface of the blade. This may suggest that the thin boundary layer developing on the blade surface is not large enough for the high free–stream turbulence to produce a noticeable effect.

4.1.3   Effect of Incidence Angle

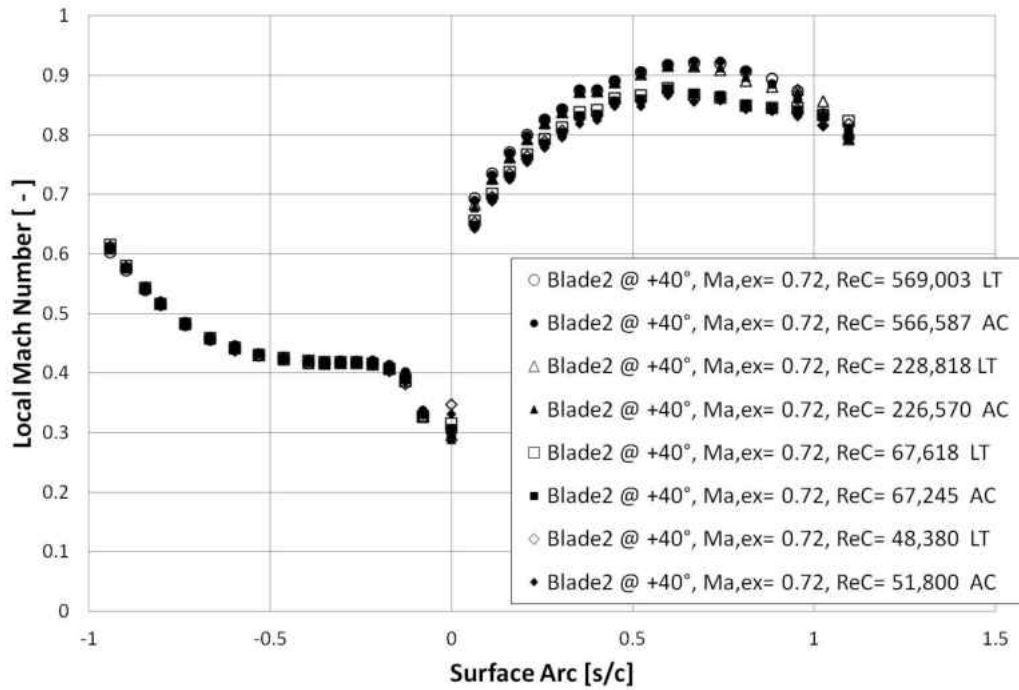The eight slanted nozzles simulated the different incidence angles listed in Table 3.2 of

Fig. 4.4: Effect of Free–Stream Turbulence on Blade 2 Surface Mach Number distributions at +5.8° Incidence Angle.

Chapter III. For the purpose of clarity, analyses of the investigated angles were grouped in two different plots in a manner that shows comparable results. Figure 4.5 shows the Mach number distributions on blade 2 at nominal Reynolds number of 568,000 and high turbulence level, and Figure 4.6 shows the Mach number distributions at nominal Reynolds number of 228,000 and the low turbulence level. It can be seen in both plots that the location of the stagnation point moves as the incidence angle varies, as it had been documented in the literature. As the inlet angle decreases from +40° to -17° the stagnation point moves toward the suction side, from the zero point to the next pressure tap located on the suction side (at 0.06 normalized distance). The movement of the stagnation point can be revealed by observing the velocity variation in the over–speed region, on the suction surface. Figure 4.5 shows this phenomena better, as it can be clearly seen that the over–speed region progressively steepens as the inlet angle is further away from the inlet metal angle. On the

49

pressure side in Figure 4.5, decreasing the incidence angle generated a region of separated flow followed by the flow re–attachment downstream. In Figure 4.6, it appears that the magnitude of laminar separation bubble increases as the incidence angle decreases further from the inlet metal angle.
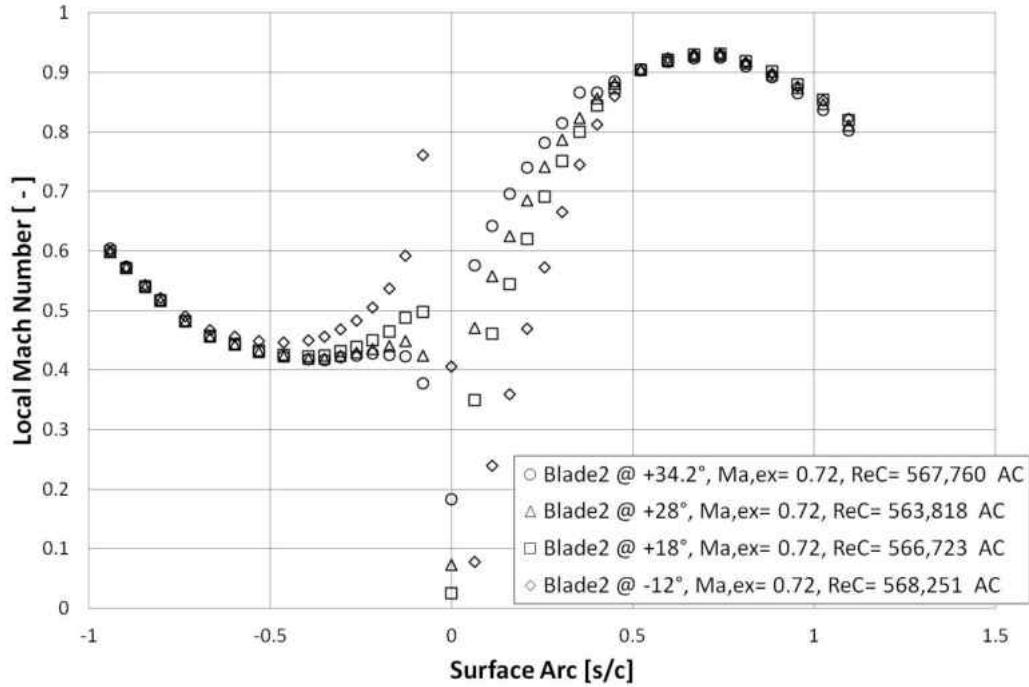

Fig. 4.5: Effect of four Incidence Angle on Blade 2 Surface Mach Number distributions at $Re_C = 568,000$ for High Turbulence Level.

4.2 Heat Transfer

Results of the heat transfer analyses presented in this section of the thesis will focus on one flow condition ($Re_C = 568,000$, at exit Mach number $M = 0.72$). The temperature distribution along the blade surface was measured with 36 embedded thermocouples. Figure F.1 in Appendix F shows raw temperature data for the incidence angle of $+5.8°$. Thermocouples upstream of thermocouple #19 (leading–edge) were positioned on the suction surface, while those downstream were positioned on the pressure surface. Thermocouple #36 was placed very close to the copper bus bar, and the measured temperature was strongly affected by the fin effect of the bus bar. It was determined after few analyses that
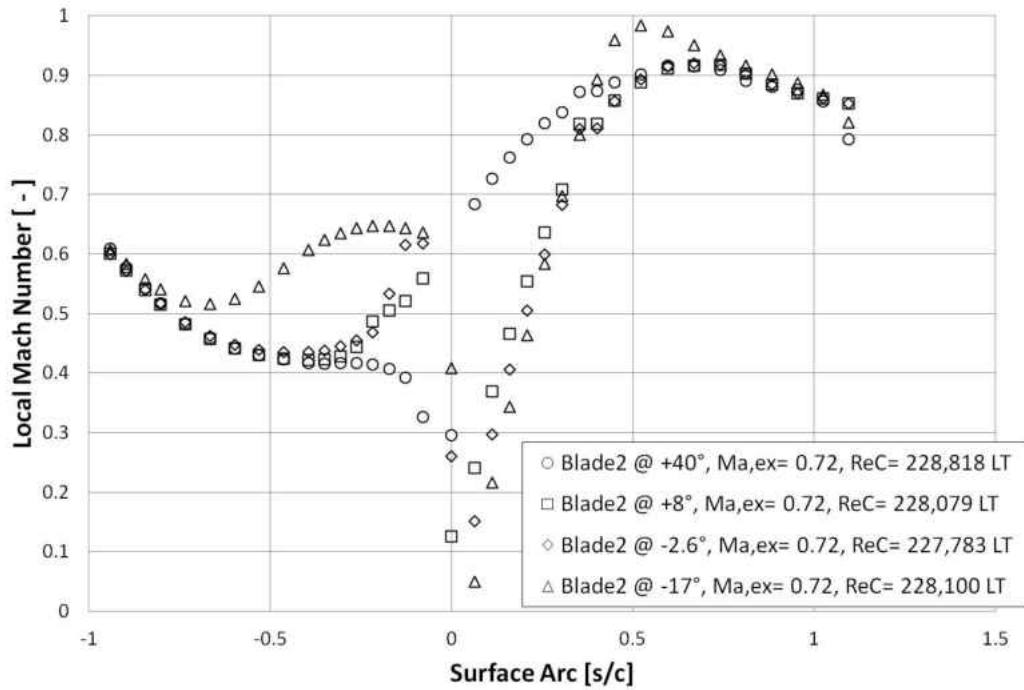
Fig. 4.6: Effect of four Incidence Angle on Blade 2 Surface Mach Number distributions at $Re_C = 228,000$ for Low Turbulence Level.

the reading observed from thermocouple #36 did not accurately represent the local heat transfer at the trailing–edge. Therefore, thermocouple #36 was omitted from the results presented below, but it was utilized in the conduction analysis.

4.2.1   Adiabatic Wall Temperature

The measured adiabatic wall temperature distributions were corrected to minimize the effect of the conduction through the blade. A first step to the heat transfer analyses was to evaluate the corrected adiabatic wall temperature distributions against the laminar and the turbulent recovery temperature distributions. The laminar and the turbulent recovery temperatures were assumed from the isentropic Mach number distributions, presented above in this section, and using the following relation:

$$T_r = T_t \cdot \frac{1 + r\frac{\gamma-1}{2}M^2}{1 + \frac{\gamma-1}{2}M^2} \tag{4.2.1}$$

where T_t is the total temperature, M is the local isentropic Mach number, and r is the laminar or the turbulent recovery coefficient. Figure 4.7 shows the adiabatic wall temperature distribution at the incidence angle of $0°$ ($34.2°$ inlet angle) for the high turbulence level. The negative abscissa values represent the pressure surface and the positive values represent the suction surface of blade 2, as it is illustrated in the figure. Multiple wall temperatures were interpolated from adjoining thermocouple measurements for consistency with the number of temperature boundary conditions required in the conduction model. The corrected values of these temperatures are represented with the closed symbols in Figure 4.7. The round open symbols represent the corrected adiabatic wall temperature distribution obtained from the measurement of 35 thermocouples, and the square symbols represent the wind tunnel raw data. It can be seen that the corrected wall temperature distribution shows a profile more consistent with the expected recovery temperature distributions. On the pressure surface in Figure 4.7, the corrected adiabatic wall temperature distribution shows a departure from the laminar recovery temperature distribution to the turbulent recovery temperature distribution, suggesting a transitional flow downstream the leading–edge.

The measured temperature at the zero location shows a 0.6 °C discrepancy from the laminar adiabatic wall temperature correlation. The corrected distribution shows that the effects of conduction were significantly reduced at the leading–edge and along the blade surface. Similar improvement were observed for other incidence angles, as it is shown in Figure 4.8 for the incidence angle of -16.2° at the high turbulence level. Figure 4.7 and Figure 4.8 show that the adiabatic wall temperature follows a laminar trend from the zero location to a location at the normalized distance of $s/c = 0.74$ on the suction surface, after which a mild temperature rise is observed toward the turbulent adiabatic wall temperature correlation. There is a sudden temperature rise from thermocouple #7 (suction side) that is observed in both figures. Laminar and turbulent adiabatic wall temperature distributions do not present such a rise. Furthermore, knowledge of the surface Mach number distributions on the suction surface for the incidence angles of 0° and -16.2° (18° inlet angle) do not show

a transitional flow at that location. A possible explanation might be that thermocouple #7 has a high level of uncertainty and could have measured approximately 0.5 °C over the actual sensed temperature.

On the pressure surface, the adiabatic wall temperature distributions appear to have a less "clean" profile in both figures. From Figure 4.7, a laminar trend is observed near the leading–edge followed by an increase toward the turbulent adiabatic wall temperature correlation, suggesting that the smooth change of the recovery temperature is due to transition. This smooth change of the recovery temperature was also observed at the incidence angle of +5.8° and -6.2°, for the high turbulence case. At the low turbulent level, the recovery temperature on the pressure surface appears to be consistent with the laminar adiabatic wall temperature correlation from the leading–edge to the trailing–edge for the incidence angles of +5.8° and 0°, as shown in Appendix F. In Figure 4.8, the sharp change of the recovery temperature on the pressure surface was typically observed for the next decreasing incidence angles: these are -26.2° and -36.8°. The isentropic Mach number distributions for these angles had shown a rapid over–speed region near the leading–edge followed by a flow re–attachment downstream to the trailing–edge on the pressure surface, for the high turbulence case. This shows consistency with the observed sharp change of the recovery temperature. At the incidence angles of -46.2° and -51.2° the peak recovery temperature on the pressure surface departed from the laminar temperature correlation for about 1 °C. The corrected recovery temperature at the incidence angles of -46.2° and -51.2°, for the high turbulence level, are shown in Appendix F. The two recovery temperature distributions appeared to track back the laminar correlation at a location between the thermocouples #30 and #31 for -46.2° incidence angle, and between the thermocouples #31 and #32 for -51.2°. This is consistent with observation made from Figure 4.5 and Figure 4.6, suggesting that the point of re–attachment moved downstream toward the trailing–edge as the incidence angle was further away from the inlet metal angle.

Analyses of the recovery temperature for the Reynolds number of 228,000 showed similar consistency observed at the Reynolds number of 568,000, for the high turbulence case.

On the suction surface, the temperature distributions displayed a laminar recovery temperature trend up to a location between thermocouples #6 and #7 at which steady increase toward the turbulent recovery temperature correlation was observed for all the incidence angles. On the pressure surface, a sharp peak recovery temperature was first observed at the incidence angle of -26.2°, for the high turbulence case. At the incidence angle of -51.2° the peak recovery temperature departed from the laminar temperature correlation for about 2 °C. Results from the low turbulence case show some noticeable discrepancies from the recovery temperature correlations for some incidence angles. Particularly on the pressure surface, the corrected adiabatic wall temperature distributions did not show consistency with the laminar correlation for the incidence angles of -6.2°, -36.8°, -46.2° and -51.2°. The incidence angle of -6.2° did not present a region of sharp temperature drop on the pressure surface, as it was seen for the other three angles. A possible explanation to the observed discrepancies at these incidence angles would suggest that the recovery factor in a separated flow region, although unknown, might be lower than the laminar recovery coefficient.

In general, it was observed that the corrected recovery temperature distributions on the pressure surface were consistent with the laminar recovery temperature correlation, at the low turbulence level, up to a location between thermocouples #34 and #35 at which the temperature dropped below the laminar correlation. Some exceptions to this observation were found at the incidence angles of -36.8°, -46.2° and -51.2°, where the sharp peak temperatures were observed. At the high turbulence level, the pressure surface distributions showed increasing recovery temperature toward the turbulent recovery temperature correlation, downstream of the leading–edge. This temperature change was observed for the two highest Reynolds numbers, and for most of the incidence angles other than -46.2° and -51.2°. Analyses of the recovery temperature distributions showed confidence that the effect of conduction had been attenuated for the most part; and also assuring that the convective heat transfer results, presented below in terms of Stanton number, were not significantly influenced.

4.2.2   Effect of Reynolds Number on Convective Heat Transfer

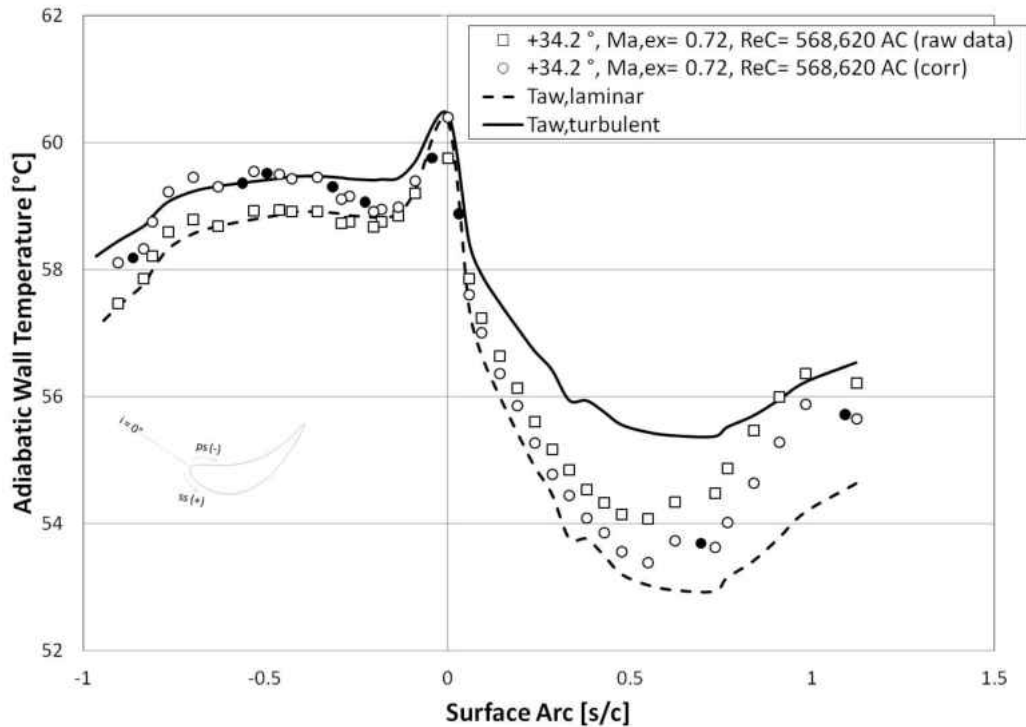The two highest Reynolds numbers were used to illustrate the effect of the Reynolds

Fig. 4.7: Comparison of Measured and Corrected Adiabatic Wall Temperature at 0° Incidence Angle, $Re_C = 568,000$, $Ma.ex = 0.72$, AC.

number at a particular incidence angle. Figure 4.9 shows the Stanton number distributions at the incidence angle of -36.8°, for the high turbulence level. On the suction surface (positive abscissa), it can be seen that the Stanton number decreases (and therefore the heat transfer coefficient decreases) downstream of the stagnation region, as the boundary layer develops and becomes thicker. The high Reynolds number in Figure 4.9 displays a gradual decrease of the Stanton number to a location near thermocouple #4, at which an increase is observed. The low Reynolds number shows similar trend with the particularity of having a rise of the Stanton number at a location near thermocouple #3. A comparison to the isentropic Mach number distribution at the incidence angle of -36.8° for the high turbulence case, revealed an attached flow for the two Reynolds numbers. On the pressure surface (negative abscissa) a rapid decrease of the Stanton number is observed downstream of the leading–edge. This drastic change suggests a region of separated flow in which the
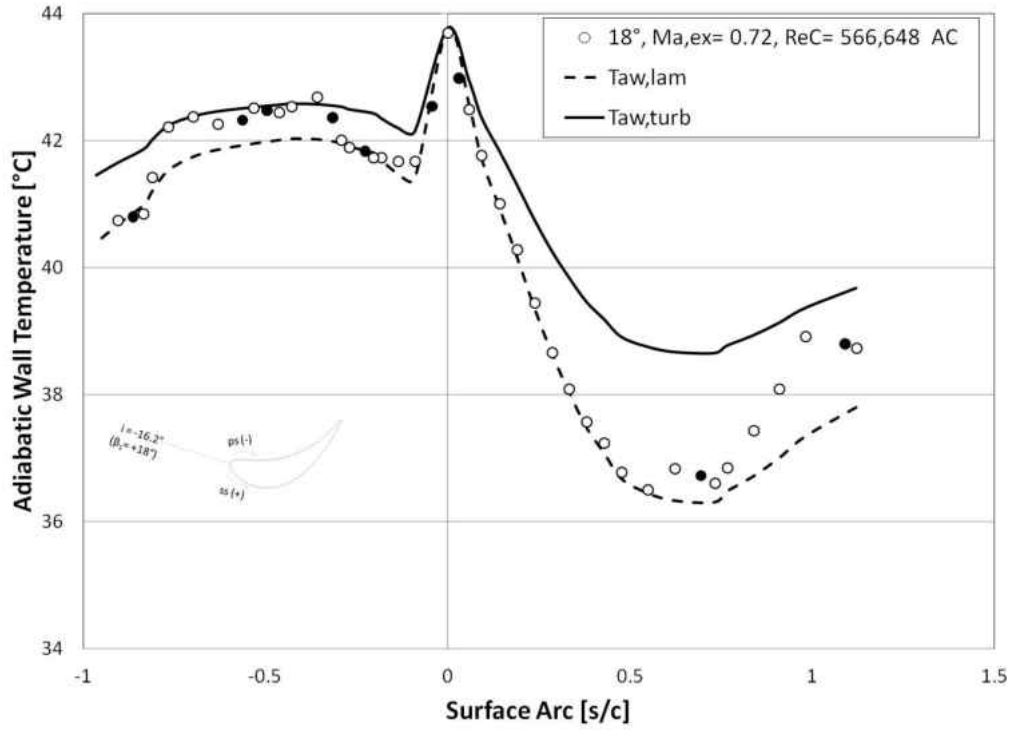
Fig. 4.8: Corrected Adiabatic Wall Temperature at -16.2° Incidence Angle, $Re_C = 568,000$, $Ma.ex = 0.72$, AC.

heat transfer is known to be suppressed. It can be seen that the heat transfer is suppressed at two thermocouple locations (#20 and #21) downstream of the stagnation point for the low Reynolds number, and at one thermocouple location (#20) for the high Reynolds number. This is consistent with what had been shown in Figure 4.2, suggesting that the region of laminar separation bubble increases as the Reynolds number decreases. Figure 4.9 also displays the evidence of an increasing Stanton number at the stagnation point as the Reynolds number decreases. The following *Pohlhausen solution* from Kays *et al* [49] explains that the increase of the Stanton number is inversely proportional to the square root of the Reynolds number:

$$St \cdot Pr^{2/3} = 0.332 \cdot Re_x^{-1/2} \qquad (4.2.2)$$

Equation 4.2.2 shows that the Stanton number at the leading–edge would increase by a factor of about 1.58 from the nominal Reynolds number of 568,000 to 228,000. The results shown

in Figure 4.9 revealed a 1.47 factor increase, yielding a minor discrepancy of 7.2% from *Pohlhausen solution*, which is likely due to turbulent augmentation. Investigations of the effect of Reynolds number on the heat transfer, at other incidence angles, also show similar believable augmentations of the Stanton number at the stagnation point with discrepancies as low as 1% (at -16.2° and -26.2° incidence angles) and as high as 28% (at +5.8° incidence angle) from Equation 4.2.2.
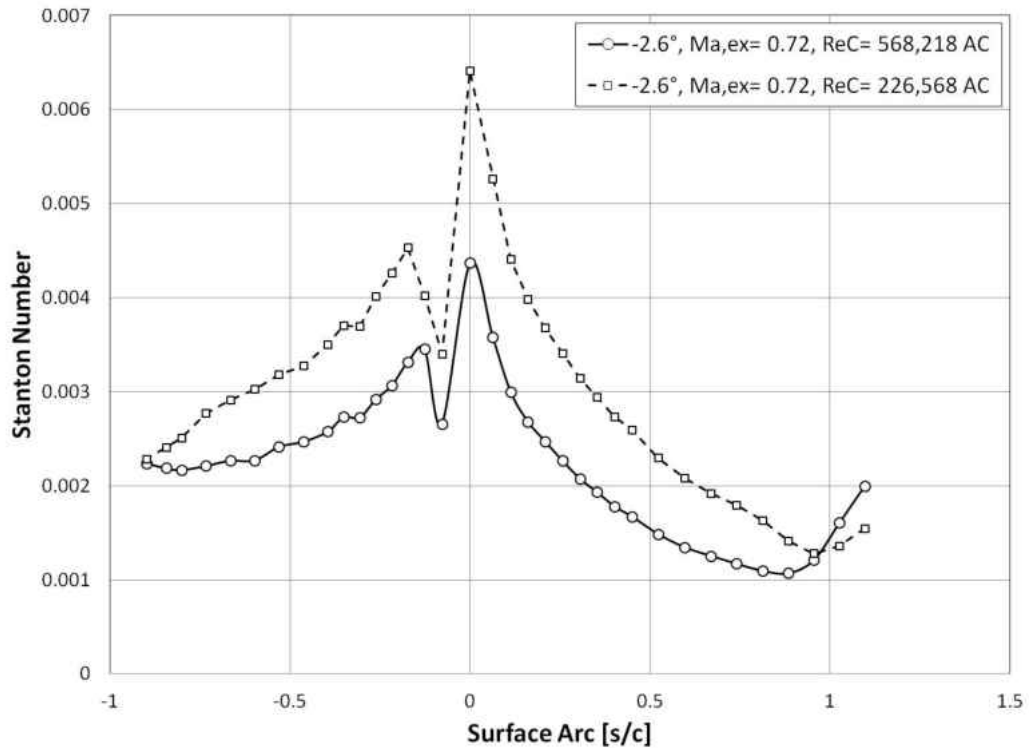
Fig. 4.9: Comparison of Stanton Number Distributions at Two Reynolds Numbers, for -36.8° Incidence Angle, AC.

4.2.3 Effect of Turbulence on Convective Heat Transfer

Figure 4.5 shown in Section *4.1.3* revealed that the high turbulence level did not produce noticeable effect on the blade loadings for the incidence angle of +5.8°, and also 0°. Absence of any significant effect of the free–stream turbulence was partially observed from the heat transfer stand point, for the incidence angle of +5.8°. Figure 4.10 shows that heat transfer is enhanced as the free–stream turbulence intensity increases, with the Stanton number

57

increasing for about 7.7% at the leading–edge. It is evident from Figure 4.10 that the heat transfer enhancement is minimum near the leading–edge region, where the boundary layer is thinner. However, a much larger effect is observed toward the trailing–edge. On the suction surface, a mild increase of the Stanton number can be observed, suggesting a transitional flow toward the trailing–edge at a location between thermocouples #5 and #6. The low turbulence case displays a sudden jump of the Stanton number at a location near thermocouple#4. This rapid increase might indicate a flow re–attachment. On the pressure surface, it appears that the free–stream turbulence promotes early transition, with the apparent transition point moving from a location near thermocouple #28 (of the low turbulence level) to a location near thermocouple #25 of the high turbulence distribution. A larger effect of the high free–stream turbulence was observed for the lowest incidence angles, particularly those exhibiting a region of laminar separation bubbles on the pressure side.
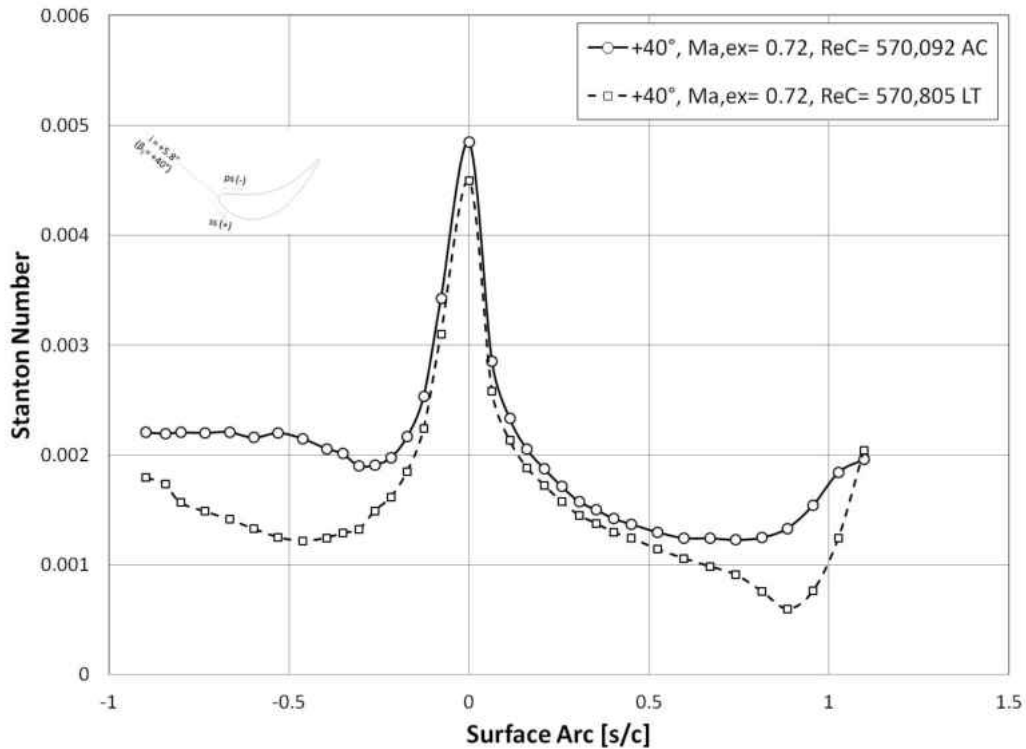
Fig. 4.10: Comparison of Stanton Number Distributions at Two Reynolds Numbers, for +5.8° Incidence Angle, $Re_C = 568,000$.

4.2.4 Effect of Incidence Angle on Convective Heat Transfer

Figure 4.11 shows the Stanton number distributions for the incidence angles of $+5.8°$, $-16.2°$, $-36.8°$, and $-51.2°$. On the suction surface, a transitional flow is apparent for the incidence angle of $+5.8°$. This flow characteristic was also observed for the incidence angle of $0°$. The other three incidence angles shown in Figure 4.11 also display a rapid increase of the Stanton number toward the trailing–edge on the suction surface. It appears that the location of transition, which may be caused by the flow re–attachment, moves further toward the trailing–edge as the incidence angle increases from $-51.2°$ to $-16.2°$. Stanton number increases at a location between thermocouples #4 and #5 for the incidence angle of $-51.2°$, and between thermocouples #3 and #4 for the incidence angles of $-16.2°$ and $-36.8°$. On the pressure surface, a transitional then fully turbulent flow can be observed for the incidence angle of $+5.8°$. As the incidence angle departs from the inlet metal angle toward the negative incidences, it can be seen that the Stanton number (and therefore the heat transfer rate) increases as the formation of the laminar separation bubble region becomes more pronounced near the leading–edge. For the incidence angle of $-16.2°$, a transitional flow can be seen downstream of the leading–edge at a location between thermocouples #23 and #24. The incidence angles of $-36.8°$, and $-51.2°$ display regions of laminar separation bubbles characterized by the rapid drop of the Stanton number near the leading–edge. It appears that the Stanton number value at the location of thermocouple #20 for the incidence angle of $-36.8°$ is lower than the value of the same thermocouple for the incidence angle of $-51.2°$. This result seems to be in contradiction with what had been observed from the isentropic Mach number distributions. A reason to this peculiar observation can be explained by verifying the location of the leading–edge. It had been observed from the isentropic Mach number distributions that the leading–edge moves from the pressure surface to the suction surface as the incidence angle decreases to $-51.2°$. Therefore, the leading–edge for the incidence angle of $-51.2°$ actually lies between thermocouples #18 and #19, with the Stanton number value possibly higher than what is observed for $-36.8°$.

Observations obtained from the high turbulence level and shown in Figure 4.11 were

similar to those obtained for the low turbulence case and shown in Figure G.3, in Appendix G, with some exceptions. On the suction surface, the low turbulence level presented a flow re–attachment near the trailing–edge for all the incidence angles. The location of the re–attachment point seemed to be near thermocouple #3 for most angles. On the pressure surface, the transitional flow was observed for the incidence angles of +5.8° and 0°, at a location near thermocouple #28. No appreciable result can be obtained from the leading–edge standpoint, due to the fact that the thermocouples concentration at the leading–edge region did not properly capture the heat–transfer rates at some incidence angles.
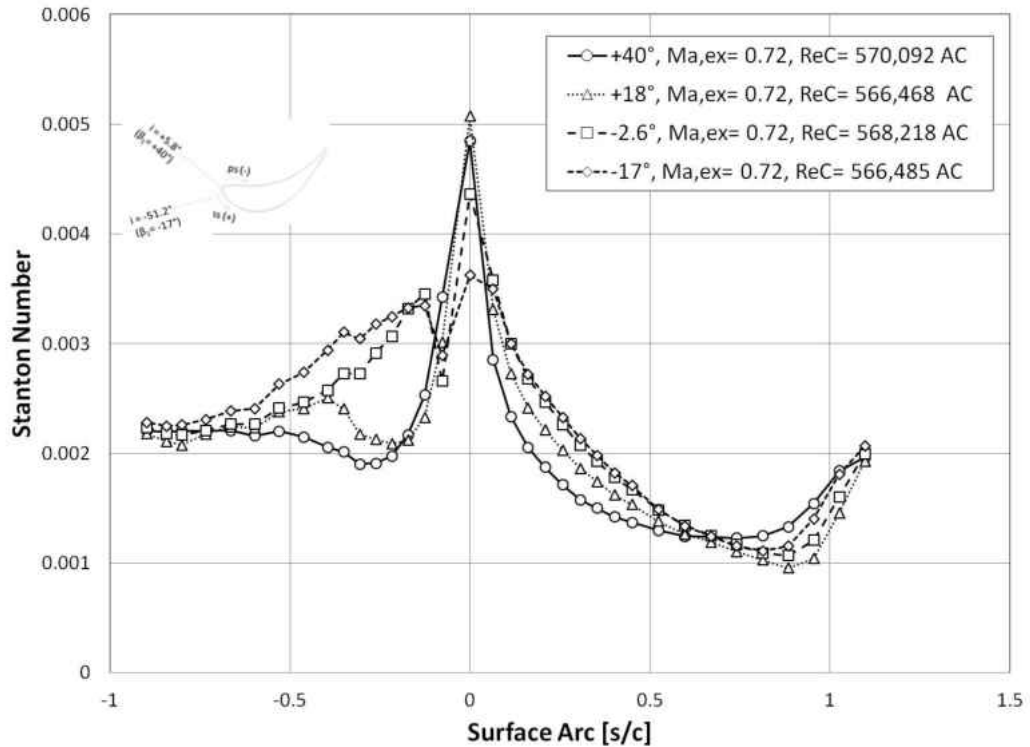
Fig. 4.11: Comparison of Stanton Number Distributions of Four Incidence Angles, $Re_C = 568,000$, AC.

CHAPTER V

CONCLUSION

UND's compressible flow wind tunnel facility had been updated to conduct steady state experiments on a low pressure modular–cascade. The updated facility was setup to investigate the effect of eight incidence angles on the heat transfer of an incidence–tolerant turbine blade. The different incidence angles varied from $+40°$ to $-17°$ over a range of nominal Reynolds numbers from 50,000 to 568,000 at exit Mach numbers of 0.72 and 0.35, and at two free–stream turbulence levels. The facility presented the task of changing some major components of the wind tunnel such as the angled nozzles, the diffusers and the ducts to maintain a sealed loop for each incidence angle. Two sets of quadruple blades were manufactured to acquire pressure and temperature measurements. Profile loss is most significantly determined by the development of the boundary layer and flow separation on the surface of the blade. There are a variety of techniques to measure the boundary layer development on a blade or vane. The heat transfer approach is the method used in this investigation. The measured temperature distributions were analyzed to account for the conductive and radiative heat fluxes. Convective heat transfer can provide knowledge of the state of the boundary layer on the blade surface. However, a better understanding of the blade boundary layer can only be obtained with knowledge of the blade loading.

A first task to this investigation required the measurement of the pressure distributions at the inlet and exit of the cascade, and pressure measurement along the surfaces of the blade 2 and blade 3. The pressure measurements were acquired at all the flow conditions, for the blade inlet metal angle ($34.2°$) and the inlet angles representative of the cruise point ($40°$) and the take–off point ($-2.6°$). Analyses of the inlet pressure distributions showed good uniformity mainly in the region upstream of the investigated blades, with the inlet Mach number averaging at about 0.4 for the inlet angle of $34.2°$ at an exit Mach number

of 0.72. The exit distributions revealed good periodic profiles for the different Reynolds numbers. The good flow quality inside the modular–cascade was also displayed by the consistent loadings on blade 2 and blade 3. Results of the inlet and exit surveys enabled the pressure and the heat transfer measurements to be acquired with confidence.

5.1   Pressure Measurement

The pressure measurements along the surface of blade 2 were obtained for all flow conditions. Results of the measurements were obtained in terms of the isentropic Mach number distributions, and they were grouped in a manner that revealed the effect of the Reynolds number, the effect of the free–stream turbulence, and the effect of the incidence angle on the blade loading. It was observed that as the Reynolds number decreased, the blade was more susceptible to flow separation in the region of adverse pressure gradients, on the suction surface. Noticeable flow separation regions were seen mostly at the two lowest Reynolds numbers. On pressure surface, the Mach number distributions were consistent for all the four Reynolds numbers, at the incidence angles ranging from $+5.8°$ to $-16.2°$ (angles that do not exhibit a noticeable region of laminar separation bubbles). The effects of free– turbulence were not apparent for the incidence angles ranging from $+5.8°$ to $-6.2°$. For the other angles, noticeable effects were observed on both the pressure and suction surfaces. On the pressure surface, the high free-stream turbulence impeded the formation of laminar separation bubbles, and appeared to have a much larger effect at the high Reynolds number. On the suction surface, the high free–stream turbulence appeared to have facilitated the boundary layer transition to turbulent flow, downstream of the peak velocity region. The transitional flows were mostly observed at the two highest Reynolds numbers, while the lowest still presented smaller separated flow regions near the trailing–edge. The effects of the incidence angle on the blade leading–edge, observed from the isentropic Mach number distributions, were in agreement with what had been documented in the literature. It was observed that as the incidence angle decreases from $+5.8°$ to $-51.2°$, the location of the stagnation line moves from the pressure side to the suction side. On the suction side, the movement of the stagnation line was manifested by the over–speed region becoming steeper as the incidence angle decreases.

5.2   Heat Transfer Measurement

The heat transfer measurements performed on blade 2 of the heat transfer set of blades, were acquired for all the test conditions. The analyses of the heat transfer measurements were completed for the two highest Reynolds numbers (568,000 and 228,000) at the exit Mach number of 0.72, for the eight different incidence angles and the two turbulence levels. An initial step, in obtaining believable heat transfer results, was to develop a conduction model that would not only correct the net heat flux, but would also improve the adiabatic wall temperature and the heated surface temperature measurements. Results of the adiabatic wall temperature distributions were compared to laminar and turbulent recovery temperature correlations. The corrected adiabatic wall temperature distributions were relatively consistent at both Reynolds numbers for the high turbulence case. The low turbulence case presented some discrepancies (particularly the Reynolds number of 228,000) with the recovery temperature correlations for the incidence angles of -6.2°, -36.8°, -46.2° and -51.2°, on the pressure side of the blade. It was concluded that the recovery factor in the separated region differed from the laminar and turbulence recovery coefficients. Results of the heat transfer analyses were grouped in terms of the effects of the Reynolds number, the free–stream turbulence and the incidence angle, as it was done for the isentropic Mach number distributions. It was observed that decreasing the Reynolds number delays the location of the point of re–attachment from the trailing–edge. It was noted that the boundary layer was mainly laminar on the suction surface up to a location of re–attachment. +5.8° and 0° incidence angles seemed to present a transitional flow behavior on the pressure and suction surfaces, for the high turbulence level. The effect of the Reynolds number was also displayed by the augmentation of the Stanton number at the leading–edge to a factor between 1.1–1.6 depending on the incidence angle. The effects of the free–stream turbulence were displayed by the enhancement of the Stanton number along the surface of the blade. The thin boundary layer downstream of the leading–edge and developing on either side of the blade yielded minimum heat transfer enhancement for the incidence angles of +5.8° and 0°. The high free–stream turbulence also reduced the magnitude of the laminar

separation bubbles for the lowest incidence angles. The variation of the incidence angle was noted to enhance the Stanton number after the flow re–attachment on the pressure surface as the angle decreased to -51.2°. A larger formation of the laminar separation bubble was also observed as the incidence angle decreased. No significant pattern was observed at the leading–edge to make conclusive remarks about the variation of the peak Stanton number due to the incidence swing.

REFERENCES

[1] Johnson, W., Yamauchi, G. K., and Watts, M. E., "NASA Heavy Lift Rotorcraft Systems Investigation," *NASA TP*, Vol. 213467, 2005.

[2] Welch, G. E., "Assessment of Aerodynamic Challenges of a Variable-Speed Power Turbine for Large Civil Tilt-Rotor Application," 2010.

[3] Coull, J. D. and Hodson, H. P., "Predicting the Profile Loss of High-Lift Low Pressure Turbines," *Journal of turbomachinery*, Vol. 134, No. 2, 2012.

[4] Denton, J. D., "Loss mechanisms in turbomachines," *Journal of Turbomachinery;(United States)*, Vol. 115, No. 4, 1993.

[5] Banieghbal, M., Curtis, E., Denton, J., Hodson, H., Huntsman, I., Schulte, V., and Harvey, N., "Wake passing in LP turbine blades," *85th Symposium on Loss Mechanisms and Unsteady Flows in Turbomachines*, North Atlantic Treaty Organization, 1995.

[6] Ames, F. and Plesniak, M., "The influence of large-scale, high-intensity turbulence on vane aerodynamic losses, wake growth, and the exit turbulence parameters," *Journal of turbomachinery*, Vol. 119, No. CONF-950629–, 1997.

[7] Xu, L. and Denton, J., "The Base-Pressure and Loss of a Family OF Four Turbine-Blades," *Journal of turbomachinery*, Vol. 110, 1988, pp. 9–17.

[8] Curtis, E., Hodson, H., Banieghbal, M., Denton, J., Howell, R., and Harvey, N., "Development of blade profiles for low-pressure turbine applications," *Journal of Turbomachinery. Transactions of the ASME*, Vol. 119, No. 3, 1997, pp. 531–538.

[9] Wubben, F., "Single and cross hot wire anemometry in incompressible flow," *NASA STI/Recon Technical Report N*, Vol. 93, 1991, pp. 16280.

[10] Würz, W. and Wagner, S., "Experimental investigations of transition development in attached boundary layers and laminar separation bubbles," *New Results in Numerical and Experimental Fluid Mechanics*, Springer, 1997, pp. 413–420.

[11] Häggmark, C., Bakchinov, A., and Alfredsson, P. H., "Measurements with a flow direction boundary-layer probe in a two-dimensional laminar separation bubble," *Experiments in fluids*, Vol. 28, No. 3, 2000, pp. 236–242.

[12] John, J. and Keith, T., "Measurements in Compressible Flow," *Gas dynamics*, Vol. 3, Pearson Education Inc, 2006, pp. 574–575.

[13] Young Jr, W. H., James F, M., and Danny R, H., "A laser velocimeter flow survey above a stalled wing," 1978.

[14] Maresca, C., Berton, E., and Favier, D., "Embedded LDV measurements in the boundary layer of moving walls," Tech. rep., DTIC Document, 2000.

[15] Boyle, R. J. and Russell, L. M., "Experimental determination of stator endwall heat transfer," *American Society of Mechanical Engineers*, Vol. 1, 1989.

[16] Giel, P. W., Thurman, D., Van Fossen, G., Hippensteele, S., and Boyle, R., "Endwall Heat Transfer Measurements in a Transonic Turbine Cascade." Tech. rep., DTIC Document, 1996.

[17] Ames, F. E., Barbot, P. A., and Wang, C., "Effects of aeroderivative combustor turbulence on endwall heat transfer distributions acquired in a linear vane cascade," *Journal of turbomachinery*, Vol. 125, No. 2, 2003, pp. 210–220.

[18] Lorenz, M., Horbach, T., Schulz, A., and Bauer, H.-J., "A Novel Measuring Technique Utilizing Temperature Sensitive PaintMeasurement Procedure, Validation, Application, and Comparison With Infrared Thermography," *Journal of turbomachinery*, Vol. 135, No. 3, 2013.

[19] Sullivan, J. P. and Liu, T., "Surface Measurement Techniques Temperature and Pressure Sensitive Paints," *Planar Optical Measurement Methods for Gas Turbine Components*, 1999.

[20] Hodson, H. and Howell, R., "Unsteady flow: its role in the low pressure turbine," *9th International Symposium Unsteady Aerodynamics, Aeroacoustics and Aeroelasticity of Turbomachines, Lyon*, 2000, pp. 4–8.

[21] Schulte, V. and Hodson, H., "Unsteady wake-induced boundary layer transition in high lift LP turbines," *Journal of turbomachinery*, Vol. 120, No. 1, 1998, pp. 28–35.

[22] Mayle, R., "The role of laminar-turbulent transition in gas turbine engines," *(ASME, International Gas Turbine and Aeroengine Congress and Exposition, 36 th, Orlando, FL, June 3-6, 1991) ASME, Transactions, Journal of Turbomachinery,*, Vol. 113, 1991, pp. 509–537.

[23] Greitzer, E. E. M., Tan, C. S., and Graf, M. B., "Laminar–turbulent boundary layer transition," *Internal flow: concepts and applications*, Vol. 3, Cambridge University Press, 2004, p. 183.

[24] Suder, K. L., Obrien, J. E., and Reshotko, E., "Experimental study of bypass transition in a boundary layer," *National Aeronautics and Space Administration Report*, Vol. 1, 1988.

[25] Anthony, R. J., Jones, T. V., and LaGraff, J. E., "High frequency surface heat flux imaging of bypass transition," *Journal of turbomachinery*, Vol. 127, No. 2, 2005, pp. 241–250.

[26] Butler, R. J., Byerley, A. R., VanTreuren, K., and Baughn, J. W., "The effect of turbulence intensity and length scale on low-pressure turbine blade aerodynamics," *International journal of heat and fluid flow*, Vol. 22, No. 2, 2001, pp. 123–133.

[27] Sanders, D. D., O'Brien, W. F., Sondergaard, R., Polanka, M. D., and Rabe, D. C., "Predicting separation and transitional flow in turbine blades at low Reynolds numbersPart II: the application to a highly separated turbine blade cascade geometry," *Journal of turbomachinery*, Vol. 133, No. 3, 2011.

[28] Mahallati, A., McAuliffe, B. R., Sjolander, S. A., and Praisner, T. J., "Aerodynamics of a Low-Pressure Turbine Airfoil at Low Reynolds NumbersPart I: Steady Flow Measurements," *Journal of turbomachinery*, Vol. 135, No. 1, 2013.

[29] Hodson, H. P. and Howell, R. J., "Bladerow interactions, transition, and high-lift aerofoils in low-pressure turbines," *Annu. Rev. Fluid Mech.*, Vol. 37, 2005, pp. 71–98.

[30] Gostelow, J. and Watson, P., "A closed circuit variable density air supply for turbomachinery research," *American Society of Mechanical Engineers, Gas Turbine Conference and Products Show, New Orleans, La*, 1976, p. 1976.

[31] Hodson, H., "Boundary-layer transition and separation near the leading edge of a high-speed turbine blade," *Journal of engineering for gas turbines and power*, Vol. 107, No. 1, 1985, pp. 127–134.

[32] Arts, T., Duboue, J., and Rollin, G., "Aerothermal performance measurements and analysis of a two-dimensional high turning rotor blade," *Journal of turbomachinery*, Vol. 120, No. CONF-970604–, 1998.

[33] the Von Karman Institute for Fluid Dynamics, "Isentropic Compression Tube Cascade Facility CT–2," https://www.vki.ac.be/index.php, 2009.

[34] Bradshaw, P. and Mehta, R., "Wind Tunnel Design," http://navier.stanford.edu/bradshaw/tunnel/index.html, 2003.

[35] Lou, W. and Hourmouziadis, J, "Separation bubbles under steady and periodic-unsteady main flow conditions," *Journal of turbomachinery*, Vol. 122, No. 4, 2000, pp. 634–643.

[36] Dähnert, J., Lyko, C., and Peitsch, D., "Transition Mechanisms in Laminar Separated Flow Under Simulated Low Pressure Turbine Aerofoil Conditions," *Journal of turbomachinery*, Vol. 135, No. 1, 2013.

[37] Selig, M. S., Lyon, C. A., Giguere, P., Ninham, C., and Guglielmo, J., *Summary of low-speed airfoil data*, Vol. 1, SoarTech Publications Virginia Beach, VA, 1995, pp. 1–315.

[38] Selig, M. S. and McGranahan, B. D., "Wind tunnel aerodynamic tests of six airfoils for use on small wind turbines," *Journal of Solar Energy Engineering(Transactions of the ASME)*, Vol. 126, No. 4, 2004, pp. 986–1001.

[39] Mehta, R. and Bradshaw, P., "Design rules for small low speed wind tunnels," *Aeronautical Journal*, Vol. 83, No. 827, 1979, pp. 443–449.

[40] McAuliffe, B., "An experimental study of flow control using blowing for a low-pressure turbine airfoil," *Masters Abstracts International*, Vol. 45, 2004.

[41] Ainley, D. and Mathieson, G., "A Method of Performance Estimation for Axial-Flow Turbines," Tech. rep., DTIC Document, 1951.

[42] Moustapha, S., Kacker, S., and Tremblay, B., "An improved incidence losses prediction method for turbine airfoils," *Journal of turbomachinery*, Vol. 112, No. 2, 1990, pp. 267–276.

[43] Benner, M., Sjolander, S., and Moustapha, S., "Influence of leading-edge geometry on profile losses in turbines at off-design incidence: Experimental results and an improved correlation," *Journal of turbomachinery*, Vol. 119, No. 2, 1997, pp. 193–200.

[44] Meschwitz, S., "The Effect of Angle of Incidence and Reynolds Number on Heat Transfer in a Linear Turbine Cascade," Tech. rep., DTIC Document, 1991.

[45] Ames, F. E., Peters, J. M., and Crook, B. A., "Effects of Incidence Angle on the Performance of Lightly Loaded Turbine Guide Vanes," *AIAA Paper*, , No. 2010-408, 2010.

[46] Mihelish, M. P., *Heat Transfer, Transition, and Aerodynamic Loss in a Linear Vane Cascade at Low Reynolds Numbers in High Speed Flows*, Master's thesis, University of North Dakota, USA, 2012.

[47] Mihelish, M. P. and Ames, F. E., "The Development Of A Closed Loop High Speed Cascade Wind Tunnel For Aerodynamic And Heat Transfer Testing At Moderate To Low Reynolds Numbers," *ASME*, No. GT-2013-95048, 2013.

[48] Moffat, R. J., "Describing the uncertainties in experimental results," *Experimental thermal and fluid science*, Vol. 1, No. 1, 1988, pp. 3–17.

[49] Kays, W. M., Crawford, M. E., and Weigand, B., "Laminar External Boundary Layers: Heat Transfer," *Convective heat and mass transfer*, Vol. 4, McGraw-Hill New York, 2005, pp. 153–154.

[50] Ortega, A. and Moffat, R., "Buoyancy induced convection in a non-uniformly heated array of cubical elements on a vertical channel wall," Tech. rep., Stanford Univ., CA (USA). Dept. of Mechanical Engineering, 1986.

APPENDICES

Appendix A
Measurement of the Temperature–Dependent Thermal Conductivity of the Somos NanoTool Material

A.1 Description

The developed finite difference conduction model of the NanoTool blade required input of the material thermal conductivity to calculate the surface heat flux due to conduction through the blade and to accurately determine the heat transfer. A slug calorimeter experiment was therefore performed to obtain the thermal conductivity of the blade material as a function of temperature. The experimental procedure and the analysis approach are those described by Ortega and Moffat [50]. The slug calorimeter experiment covered the temperature range observed during the blade cascade measurements. A picture of the slug calorimeter built and instrumented is shown in Figure A.1(a). The top piece was a 0.316 cm thick disc made out of aluminum alloy 5052. Its top surface was pray painted with a high absorptivity black coating. The base slug piece was a 2.54 cm thick cylinder made out of aluminum alloy 6061. A row of four holes with typical 0.102 cm in diameter and 1.59 cm deep, were drilled on the side surface of both the top and base pieces to allow access of the thermocouples. Two additional holes were drilled on the top surface of the top piece and the bottom surface of the base to ease the excess bonding element to ooze out. A 6.35 cm in diameter and 0.12 cm thick Somos sample was cast between the aluminum pieces of the same diameter with Omegabond 101 epoxy. The epoxy, also used to cement thermocouples during instrumentation of the slug, has a reported thermal conductivity of 1.038 W/m/K. The assembled unit was inserted into a 5.1 cm thick rigid polyisocyanurate (Energy Shield product) having both sides foil–faced. An initial test was performed using a blue polystyrene foam (Dow Styrofoam) for insulation. An aluminum foil was placed over the insulation with a cut–out exposing only the black–coated face to the impinging heat source as shown in Figure A.1(b). The heating lamps used generated approximately 300 W on the slug calorimeter setup. The multiple tests performed consisted of monitoring the

temperature gradient along the axis of the slug calorimeter. The temperatures and the time steps were recorded by a LXI data acquisition unit (Agilent 34972A).

(a) Slug Calorimeter   (b) Experimental Setup
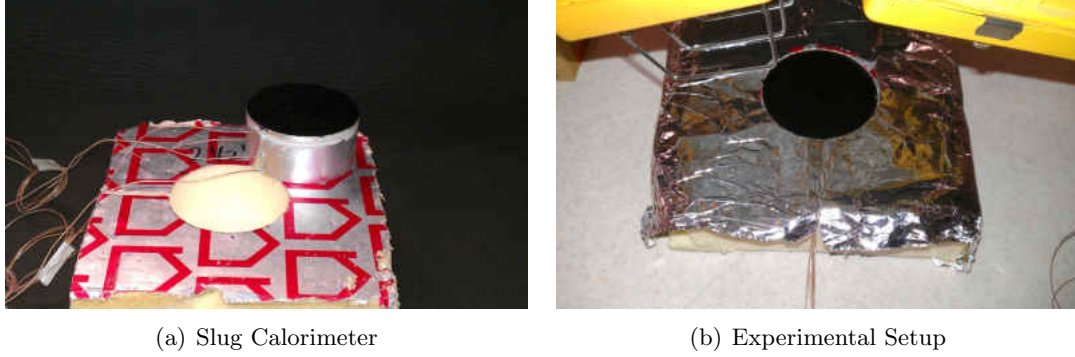
Fig. A.1: Assembled (a) Slug Calorimeter and (b) Experimental Setup for Measurements.

A.2   Results of the Measurements

The temperature–dependence thermal conductivity of the Somos NanoTool was determined using the following equation obtained from Ortega and Moffat [50]:

$$k_{nt} = \frac{(\Delta x \cdot \rho \cdot c_p)_{base}\frac{dT_{base}}{dt} + 2\sqrt{\frac{(k \cdot \rho \cdot c_p)_{ins}}{\pi t}}(\frac{A_{base,nt}}{A_0})[T_{avg}(t) - T_{avg}(o)]}{\frac{T_0(t) - T_{base}(t)}{\Delta x_{nt}}} \tag{A.0.1}$$

where $(\Delta x \cdot \rho \cdot c_p)_{base}$ are the thickness and properties of base aluminum slug, $(k \cdot \rho \cdot c_p)_{ins}$ are properties of the insulation, T_{avg} is the average temperature from the three thermocouples glued on the base slug, $\frac{A_{base,nt}}{A_0}$ is the ratio of total area insulated over the black–coated surface area, and $T_0(t)$ and $T_{base}(t)$ are the fourth order polynomial functions obtained from regression analyses of the temperatures at the top and average of the three bottom thermocouples, respectively. The constants used for properties of the polyisocyanurate insulation were:

$\rho_{ins} = 32.04 \ kg/m^3$

$c_{p,ins} = 921.1 \ J/kg - C$

$k_{ins} = 0.0238 \ W/m - C.$

An average value of the thermal conductivity of the NanoTool was obtained from the test results shown in Figure A.2

71
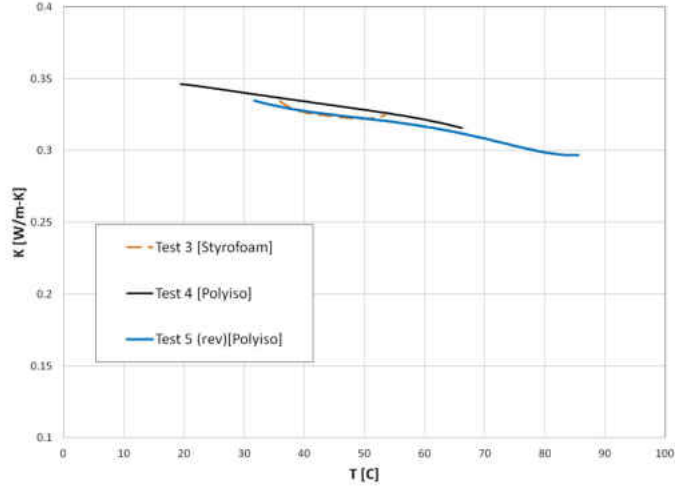
Fig. A.2: Temperature–Dependent Thermal Conductivity of the Somos NanoTool Material.

A.3   Finite–Difference Equation

The temperature distribution in the blade nodal network was determined using an approximate formulation of the finite–difference equation.
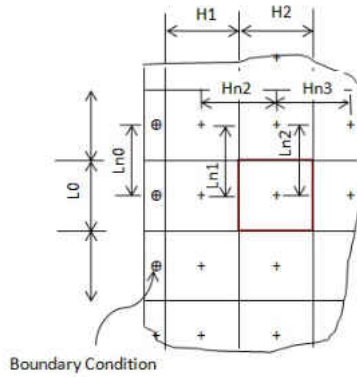
Fig. A.3: Schematic of an Approximate Blade Nodal Network.

$$\sum_{i=1}^{4} q_i = 0 \tag{A.0.2}$$

$$\frac{K \cdot H_2}{Ln_2}\left(T_{l-1,h} - T_{l,h}\right) + \frac{K \cdot L_2}{Hn_2}\left(T_{l,h-1} - T_{l,h}\right) + \frac{K \cdot H_2}{Ln_2}\left(T_{l+1,h} - T_{l,h}\right) + \frac{K \cdot L_3}{Hn_3}\left(T_{l,h+1} - T_{l,h}\right) = 0 \tag{A.0.3}$$

Appendix B

Inlet and Exit Mach number Distribution Plots

The following figures summarize the inlet and exit Mach number distributions obtained at the inlet metal angle of the blade, and the design angles representative of the cruise and take–off points.
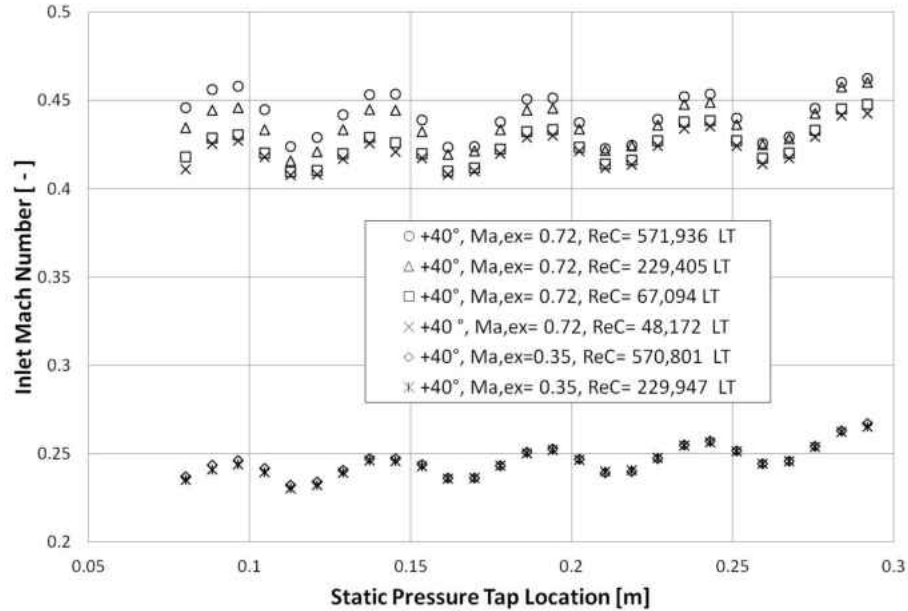
Fig. B.1: Inlet Mach Number Distributions at +5.8° Incidence Angle and Low Turbulence Level.
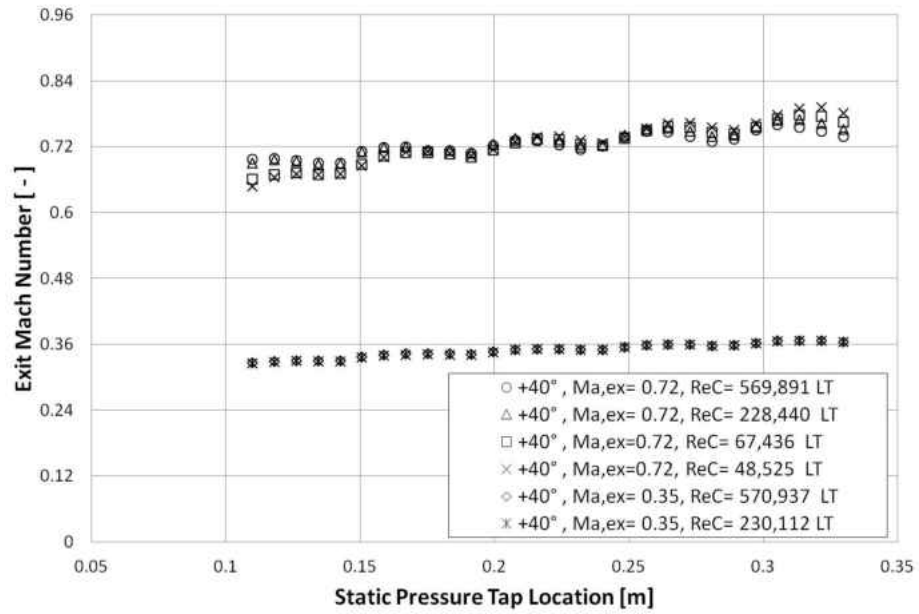
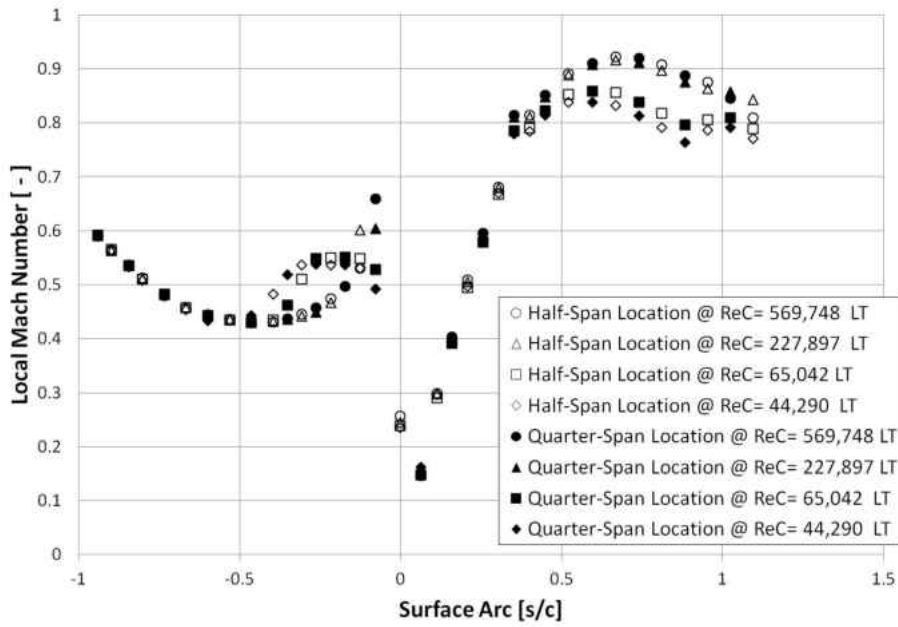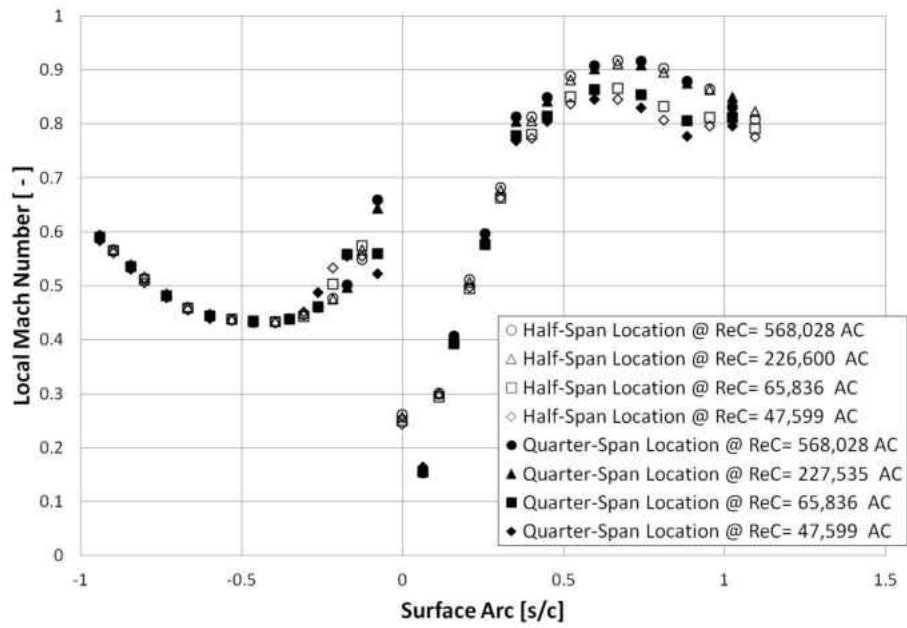Fig. B.2: Exit Mach Number Distributions at +5.8° Incidence Angle and Low Turbulence Level.
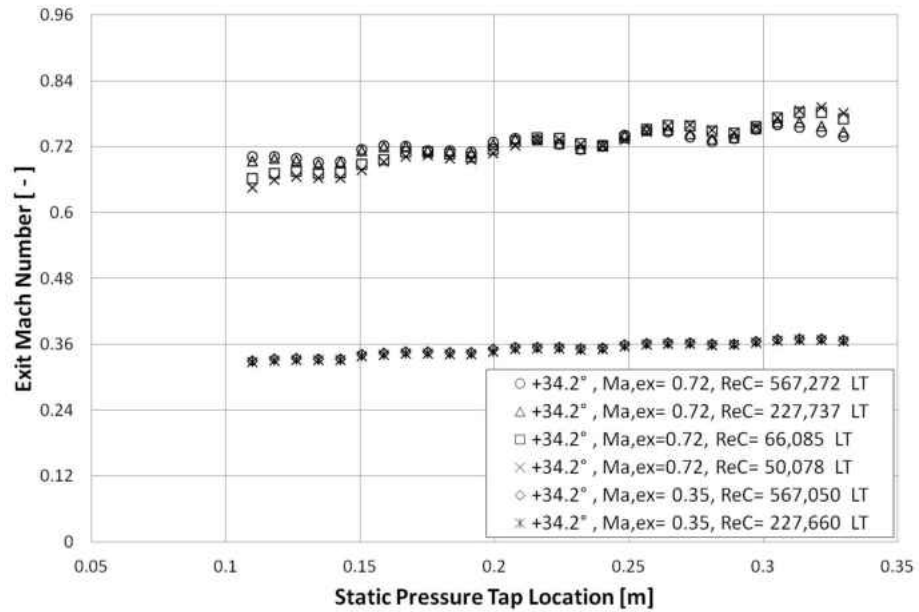
Fig. B.3: Exit Mach Number Distributions at +0° Incidence Angle and Low Turbulence Level.
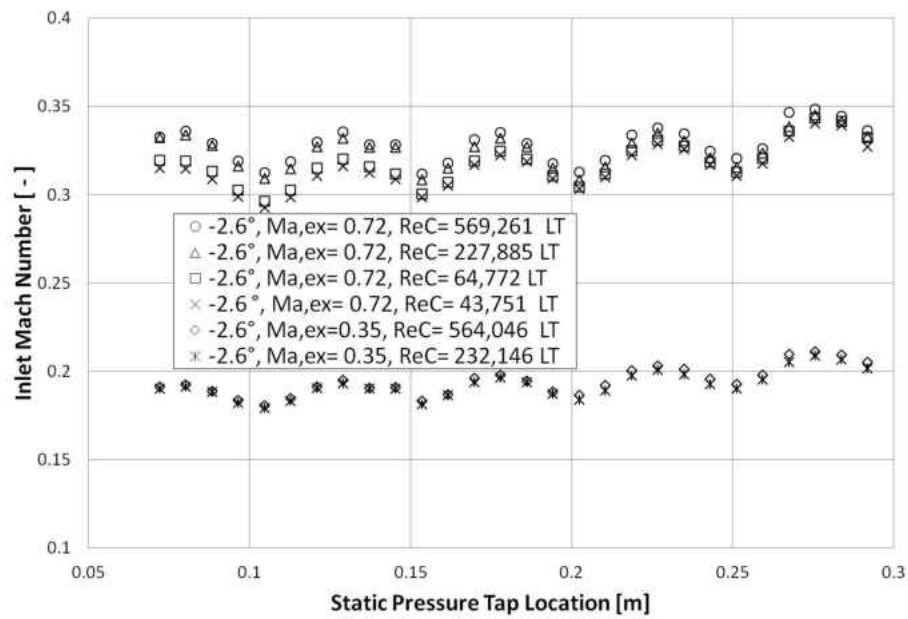
Fig. B.4: Inlet Mach Number Distributions at -36.8° Incidence Angle and Low Turbulence Level.
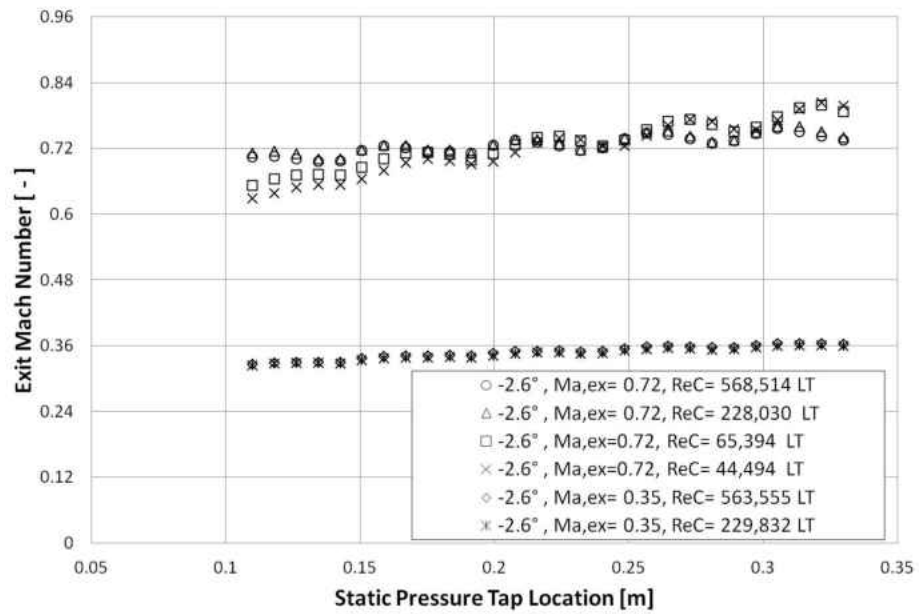
Fig. B.5: Exit Mach Number Distributions at -36.8° Incidence Angle and Low Turbulence Level.
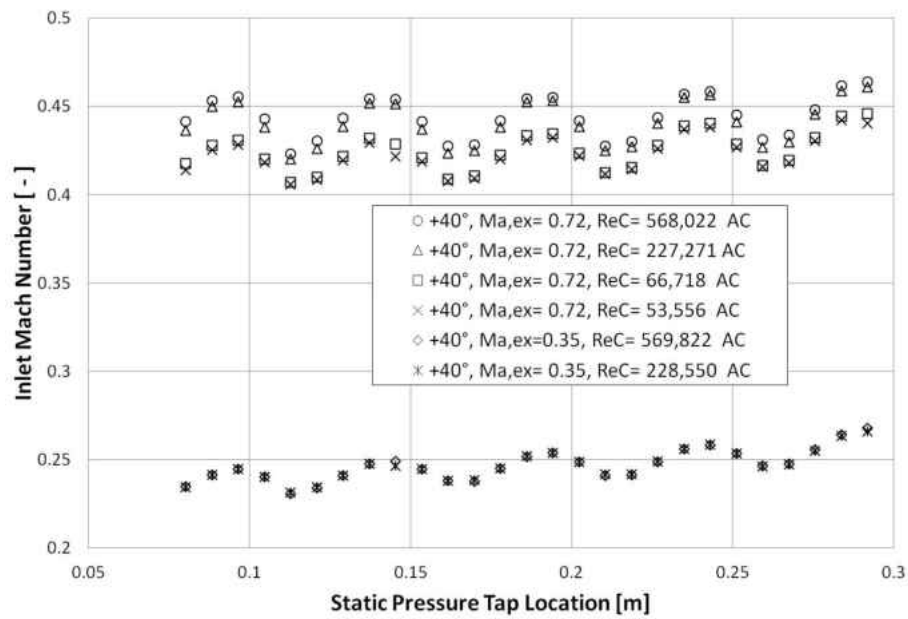
Fig. B.6: Inlet Mach Number Distributions at $+5.8°$ Incidence Angle and High Turbulence Level.
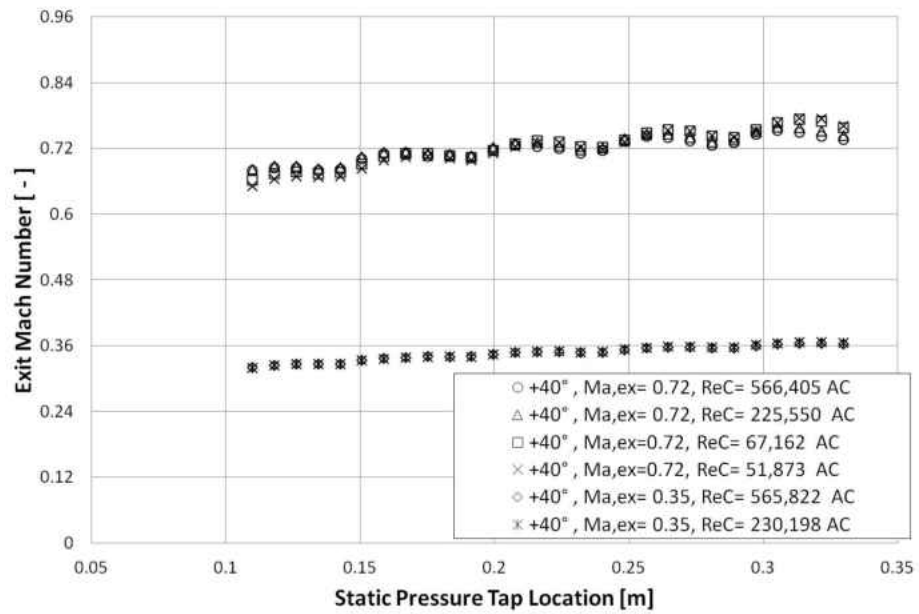
Fig. B.7: Exit Mach Number Distributions at $+5.8°$ Incidence Angle and High Turbulence Level.
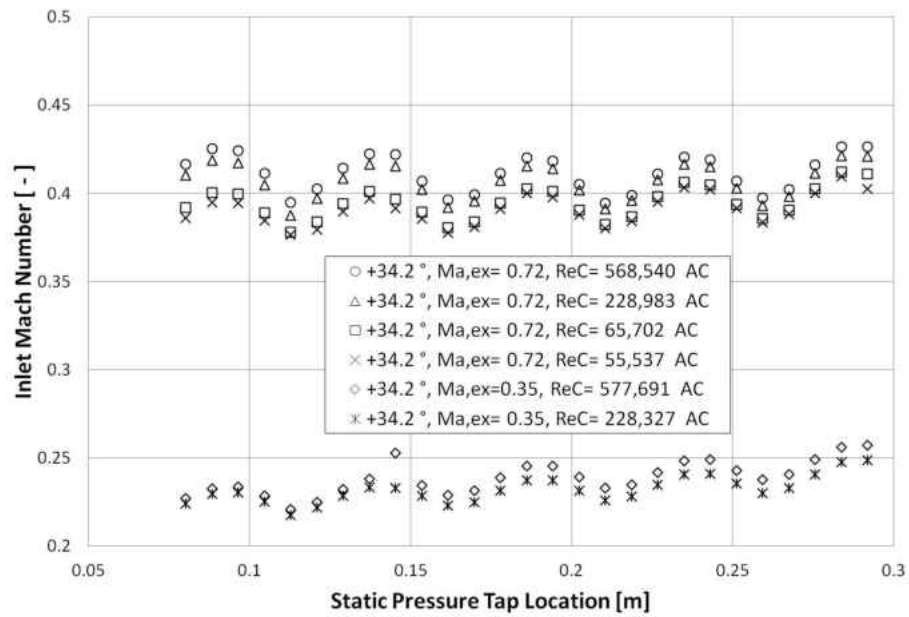
Fig. B.8: Inlet Mach Number Distributions at +0° Incidence Angle and High Turbulence Level.
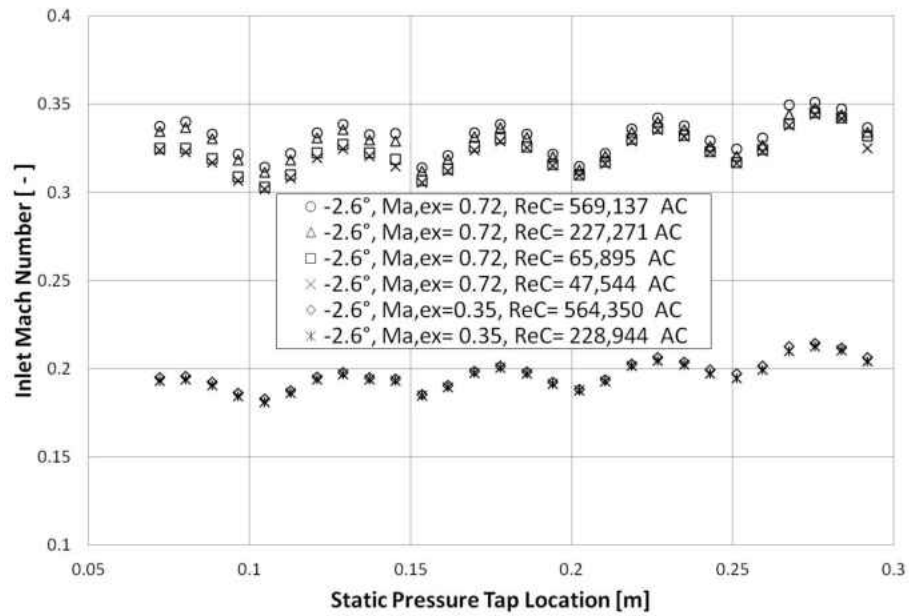
Fig. B.9: Inlet Mach Number Distributions at -36.8° Incidence Angle and High Turbulence Level.
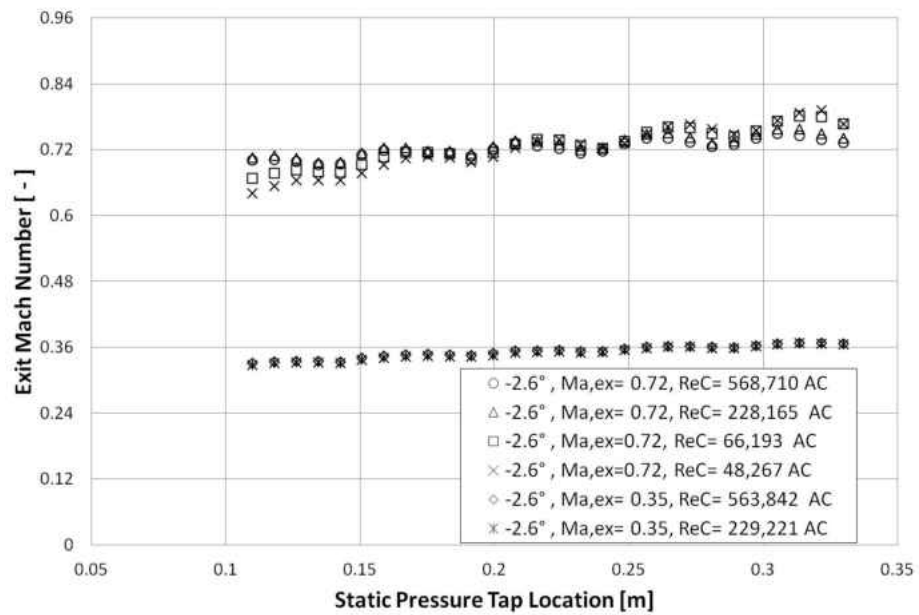
Fig. B.10: Exit Mach Number Distributions at -36.8° Incidence Angle and High Turbulence Level.

Appendix C

Surface Mach number Distribution Plots for Blade 2

The following figures summarize Mach number distributions on blade 2 not shown in the Result section for an exit Mach number of 0.72, and at the different incidence angles.
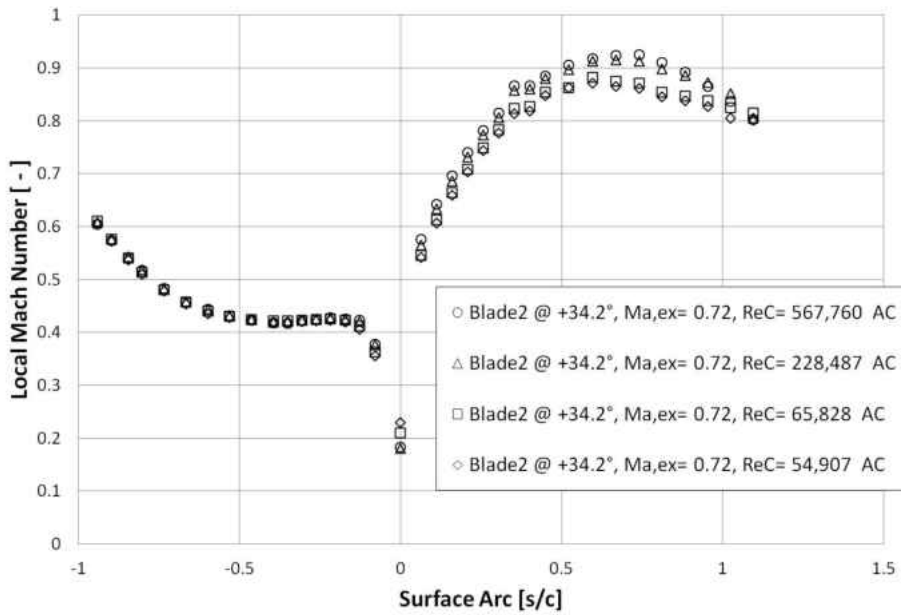
Fig. C.1: Blade 2 Surface Mach Number Distributions at 0° Incidence Angle and High Turbulence Level.
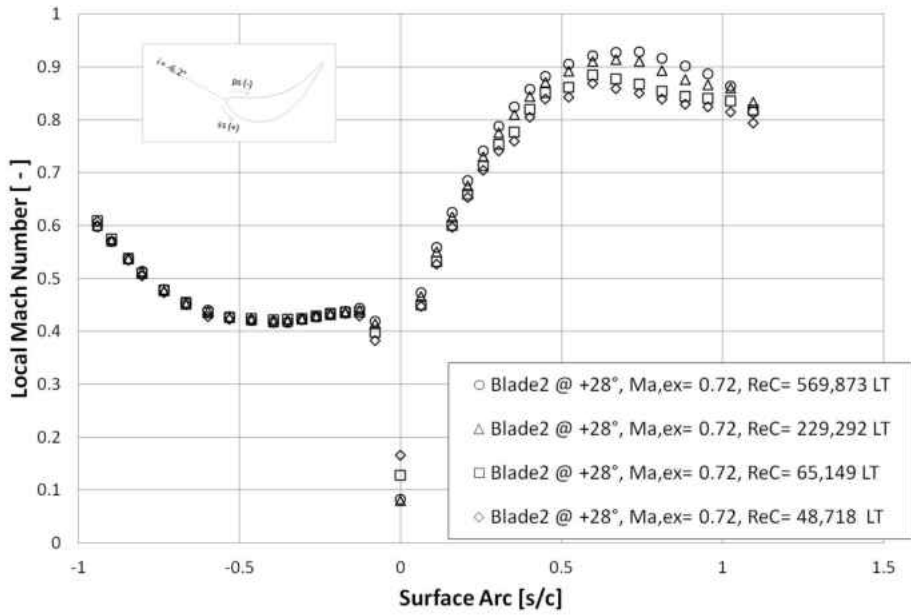
Fig. C.2: Blade 2 Surface Mach Number Distributions at -6.2° Incidence Angle and Low Turbulence Level.
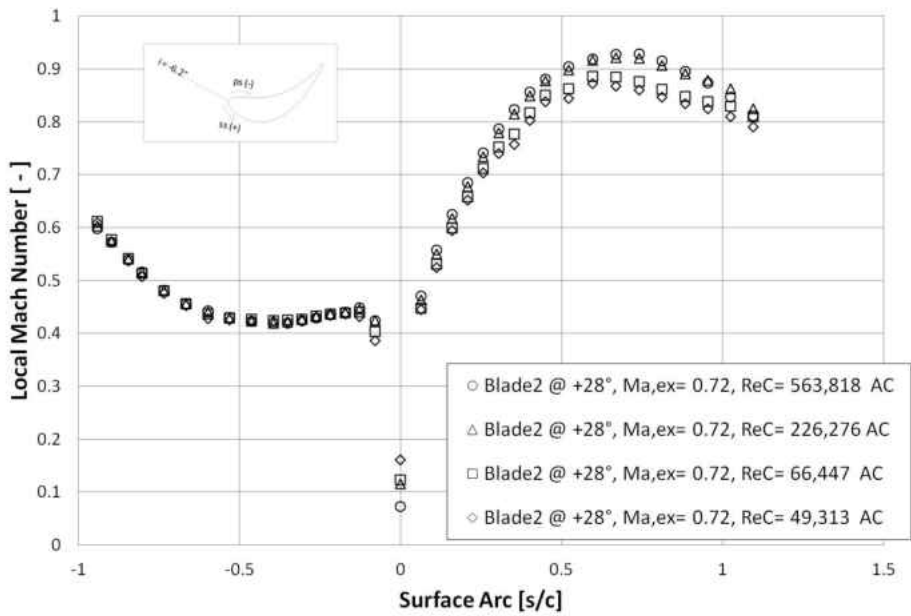
Fig. C.3: Blade 2 Surface Mach Number Distributions at -6.2° Incidence Angle and High Turbulence Level.
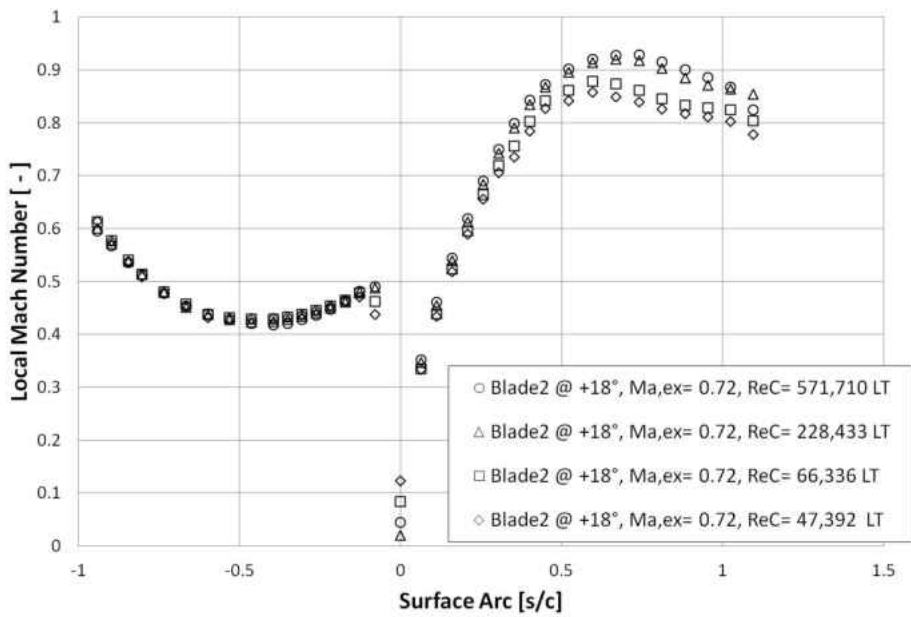
Fig. C.4: Blade 2 Surface Mach Number Distributions at -16.2° Incidence Angle and Low Turbulence Level.
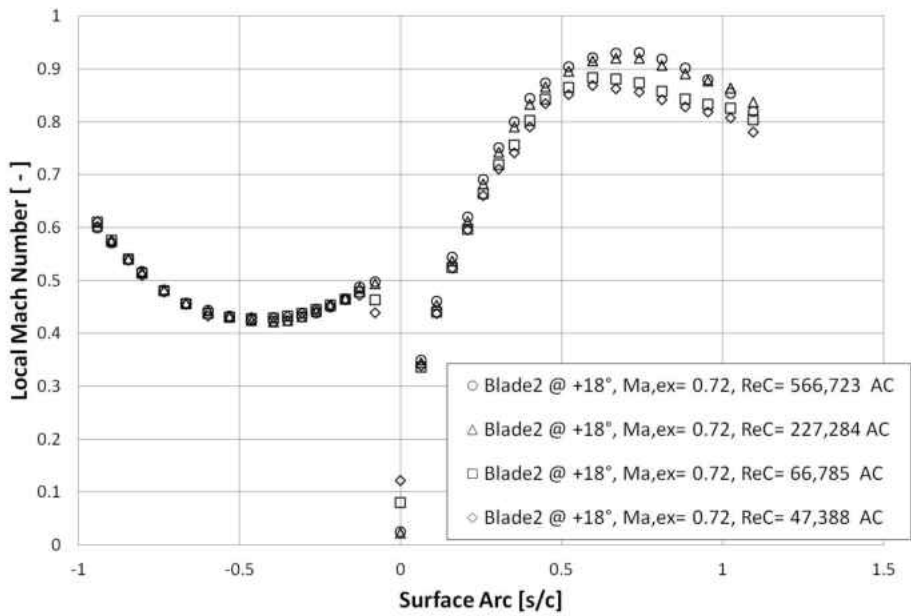
Fig. C.5: Blade 2 Surface Mach Number Distributions at Incidence Angle and High Turbulence Level.
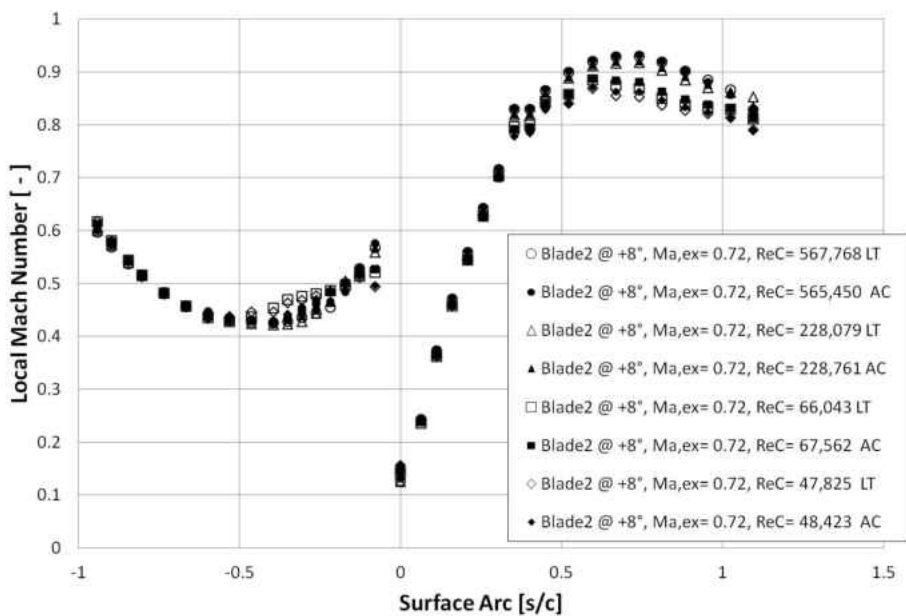
Fig. C.6: The Effect of Free–Stream Turbulence on Blade 2 Surface Mach Number Distributions at -26.2° Incidence Angle.
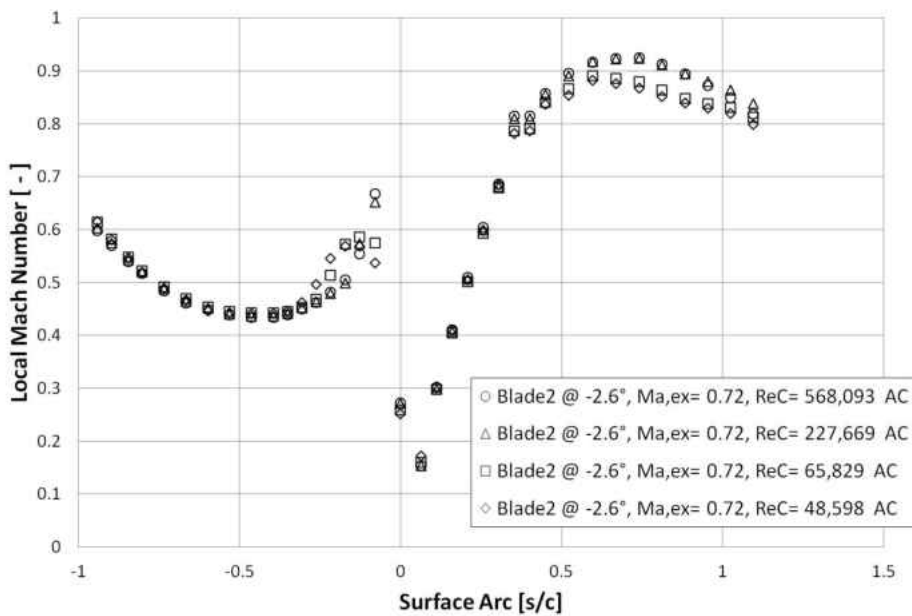
Fig. C.7: Blade 2 Surface Mach Number Distributions at -36.8° Incidence Angle and High Turbulence Level.
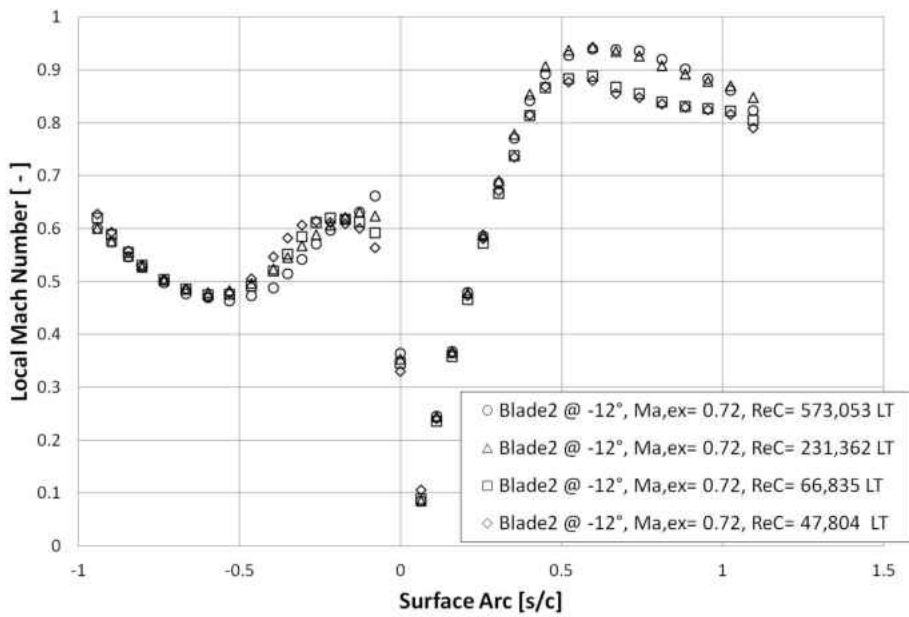
Fig. C.8: Blade 2 Surface Mach Number Distributions at -46.2° Incidence Angle and Low Turbulence Level.
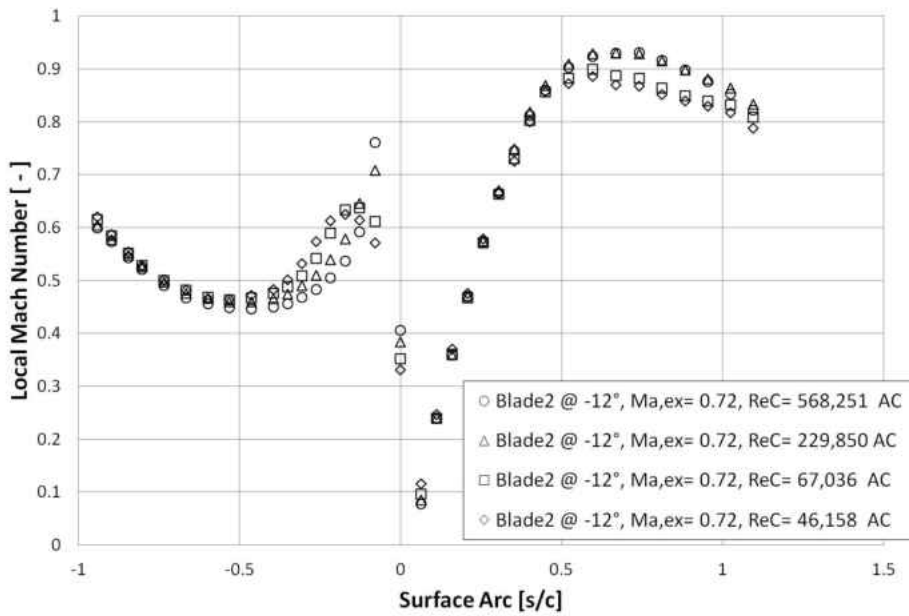
Fig. C.9: Blade 2 Surface Mach Number Distributions at -46.2° Incidence Angle and High Turbulence Level.

Appendix D

Surface Mach number Distribution Plots for Blade 3

The following figures summarize Mach number distributions on blade 3 for an exit Mach number of 0.72, at +5.8°, 0°, and -36.8° incidence angles
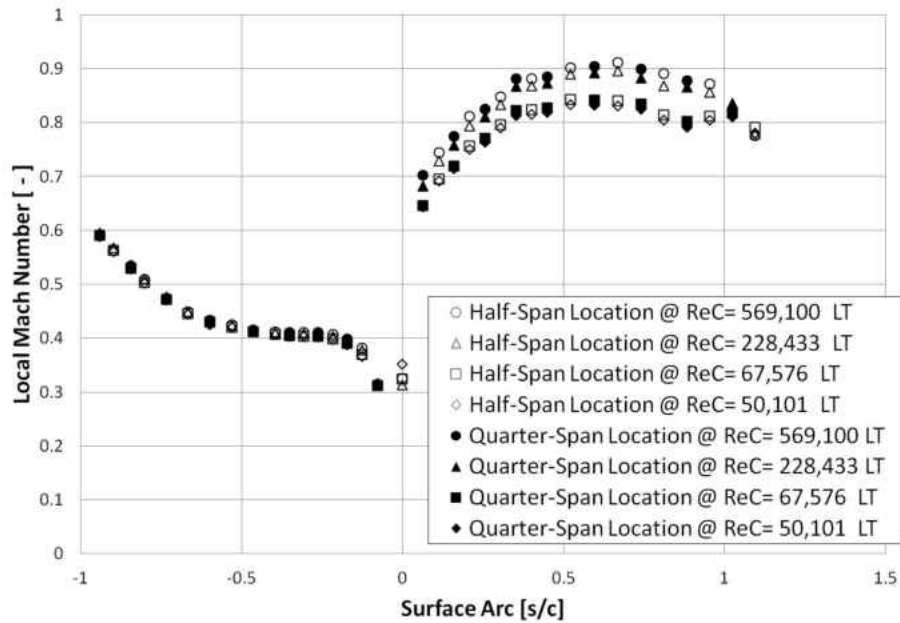
Fig. D.1: Blade 3 Surface Mach Number Distributions at +5.8° Incidence Angle and Low Turbulence Level.
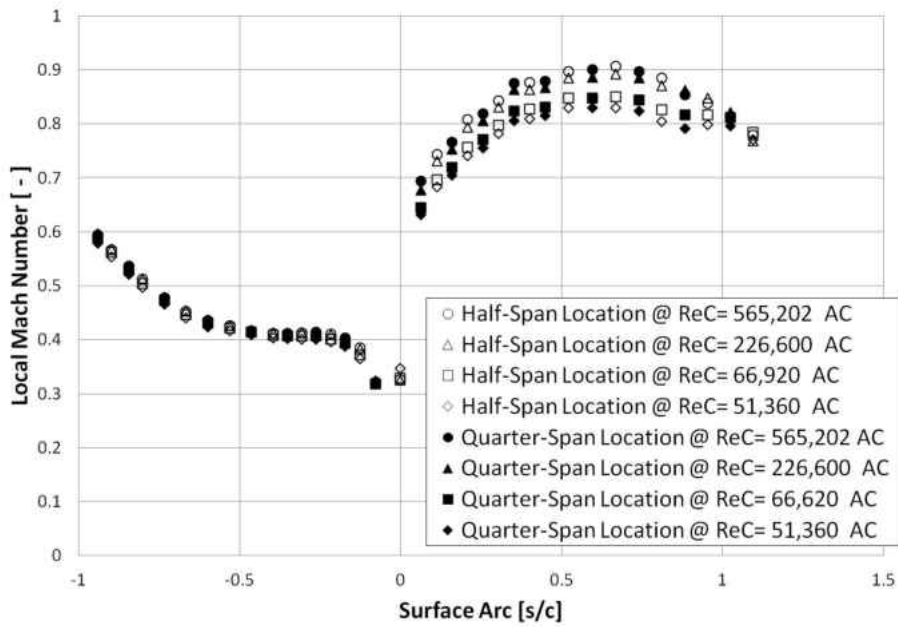
Fig. D.2: Blade 3 Surface Mach Number Distributions at +5.8° Incidence Angle and High Turbulence Level.
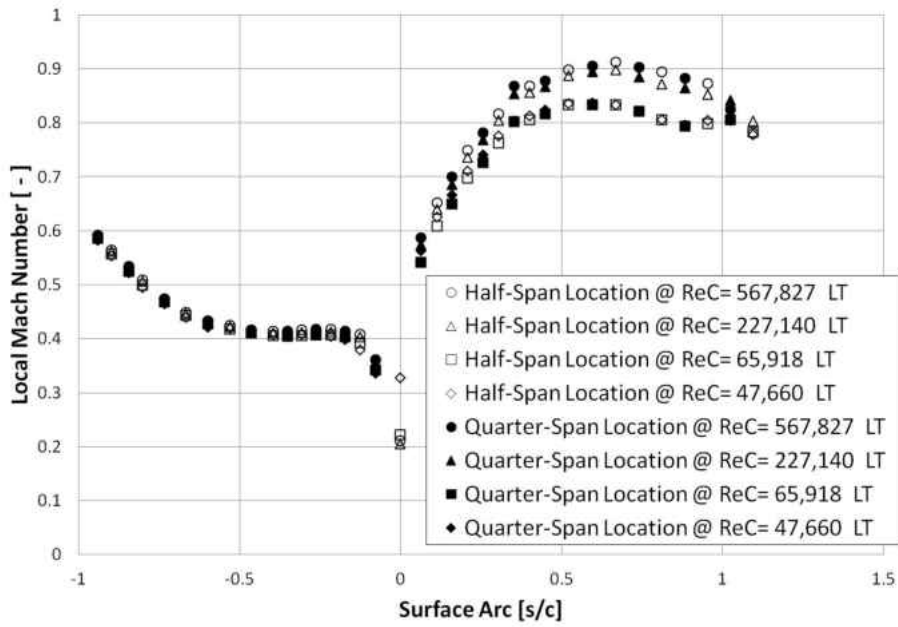
Fig. D.3: Blade 3 Surface Mach Number Distributions at 0° Incidence Angle and Low Turbulence Level.
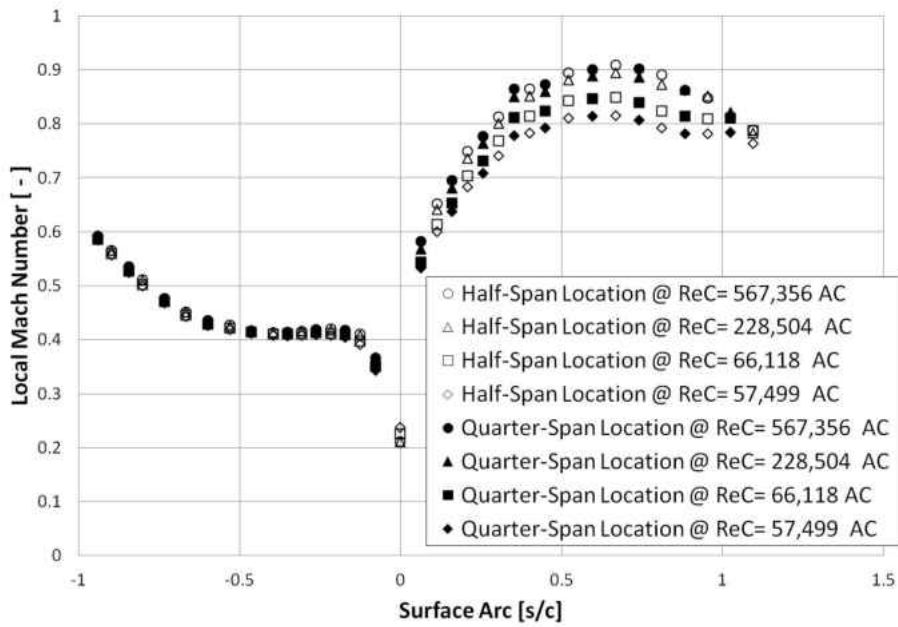
Fig. D.4: Blade 3 Surface Mach Number Distributions at 0° Incidence Angle and High Turbulence Level.

Fig. D.5: Blade 3 Surface Mach Number Distributions at -36.8° Incidence Angle and Low Turbulence Level.

Fig. D.6: Blade 3 Surface Mach Number Distributions at -36.8° Incidence Angle and High Turbulence Level.

Appendix E

Mach number Plots for Blade 2 and 3, at $Ma, ex = 0.35$

The figures summarize in this section show the Mach number distributions on blade 2 and blade 3 for an exit Mach number of 0.35 and at the different incidence angles.
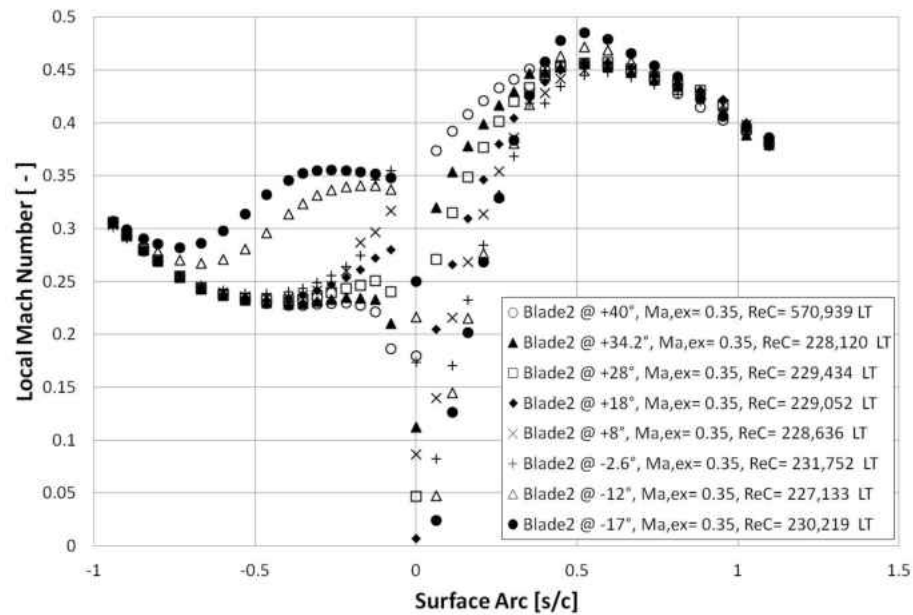
Fig. E.1: The Effect of Incidence Angle on Blade 2 Surface Mach Number Distributions at $ReC = 228,000$, $Ma, ex = 0.35$, LT.
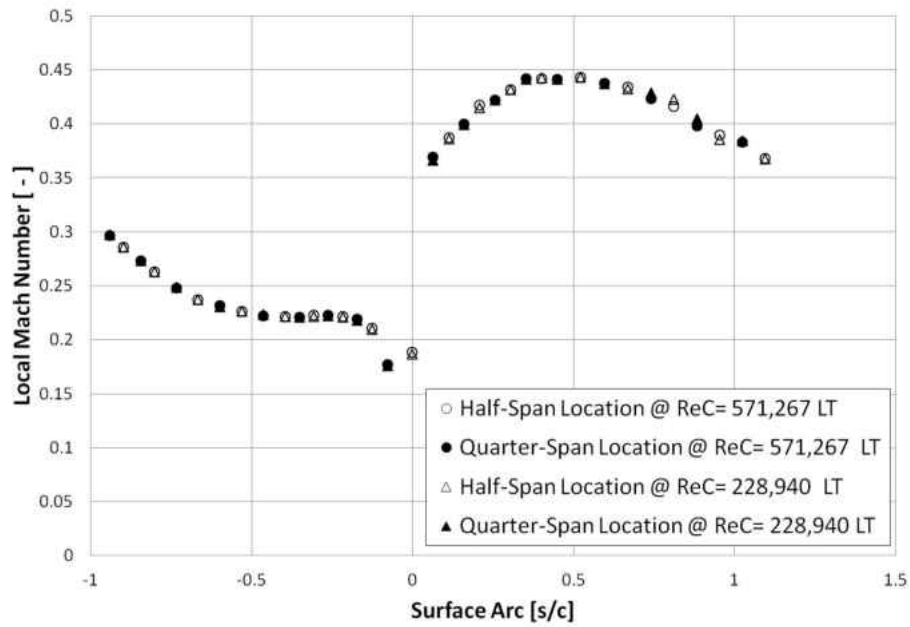
Fig. E.2: Blade 3 Surface Mach Number Distributions at $+5.8°$ Incidence Angle and $Ma, ex = 0.35$, LT.
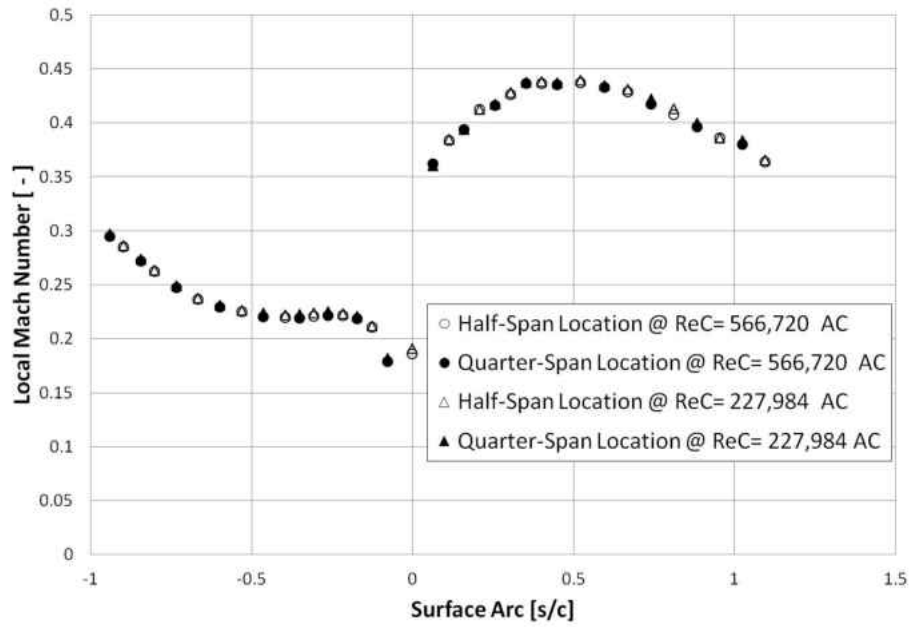
Fig. E.3: Blade 3 Surface Mach Number Distributions at $+5.8°$ Incidence Angle and $Ma, ex = 0.35$, AC.
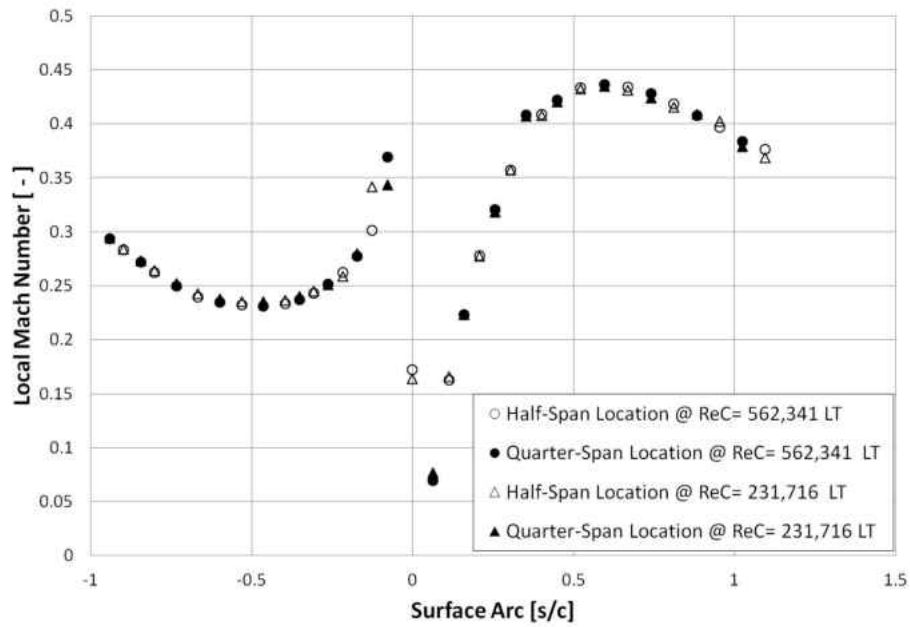
Fig. E.4: Blade 3 Surface Mach Number Distributions at -36.8° Incidence Angle and $Ma, ex = 0.35$, LT.
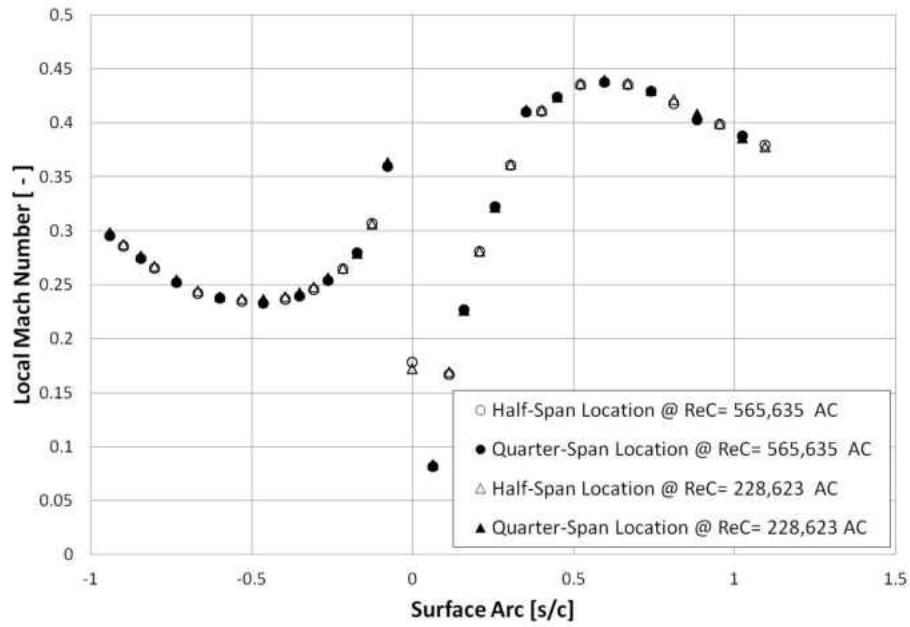
Fig. E.5: Blade 3 Surface Mach Number Distributions at -36.8° Incidence Angle and $Ma, ex = 0.35$, AC.

Appendix F

Adiabatic Wall Temperature Measurements
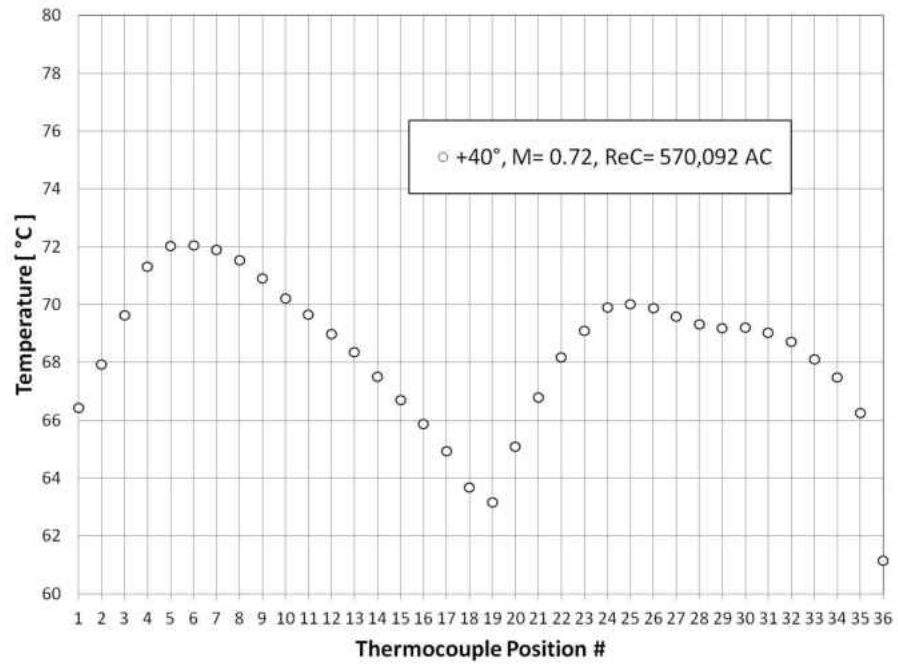
Fig. F.1: Temperature Distribution at $+5.8°$Incidence Angle, $Re_C = 568,000$, $M = 0.72$, AC.
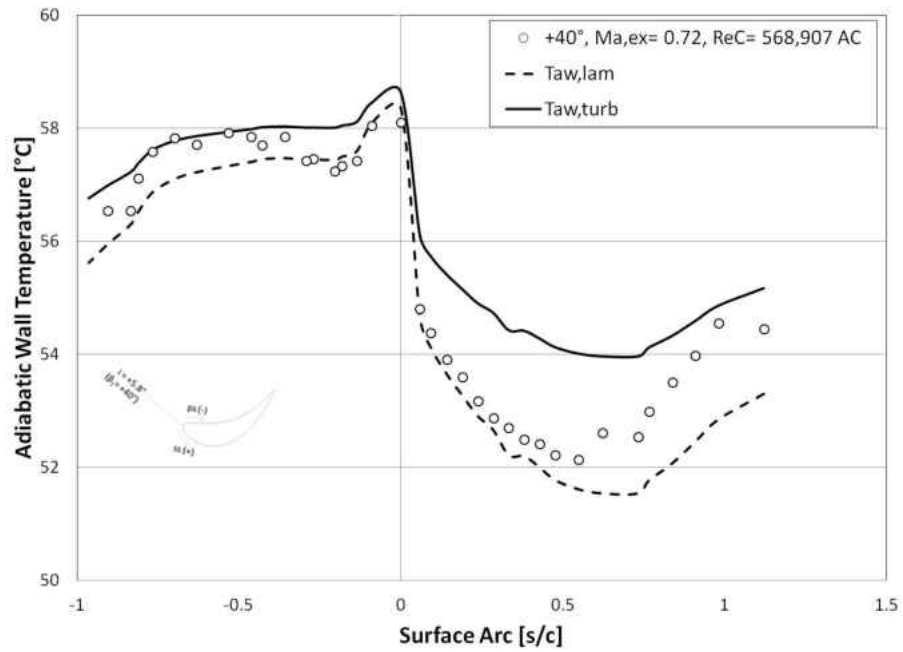
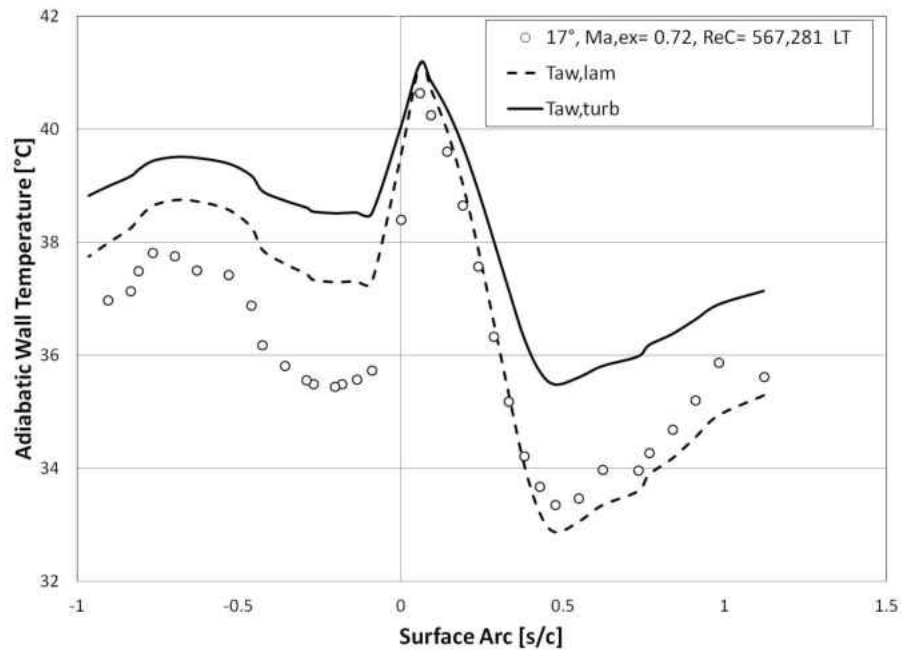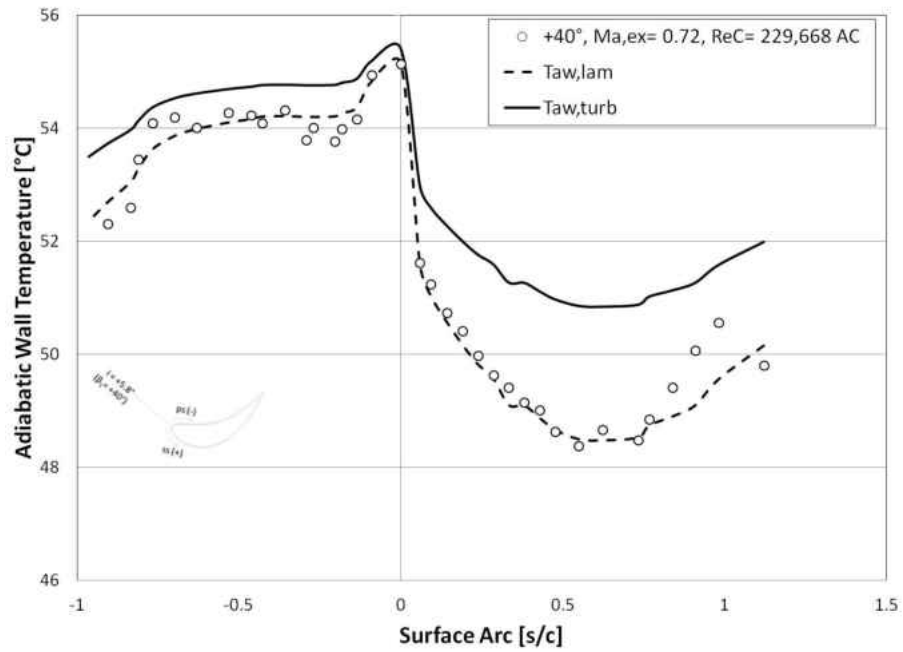Fig. F.2: Adiabatic Wall Temperature at $+5.8°$ Incidence Angle, $Re_C = 568,000$, $Ma, ex = 0.72$, AC.
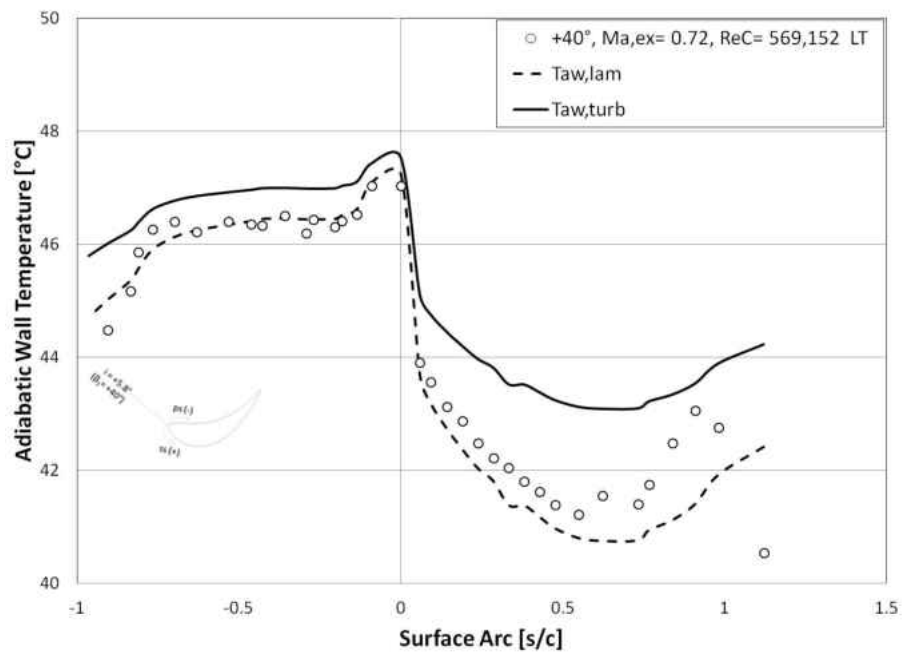
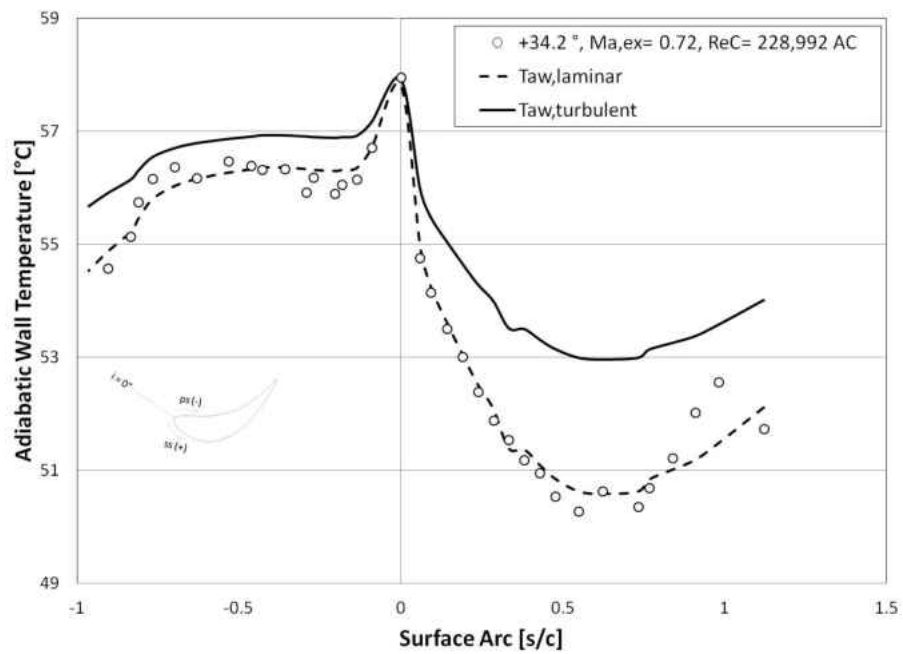Fig. F.3: Adiabatic Wall Temperature at $+5.8°$ Incidence Angle, $Re_C = 568,000$, $Ma, ex = 0.72$, LT.
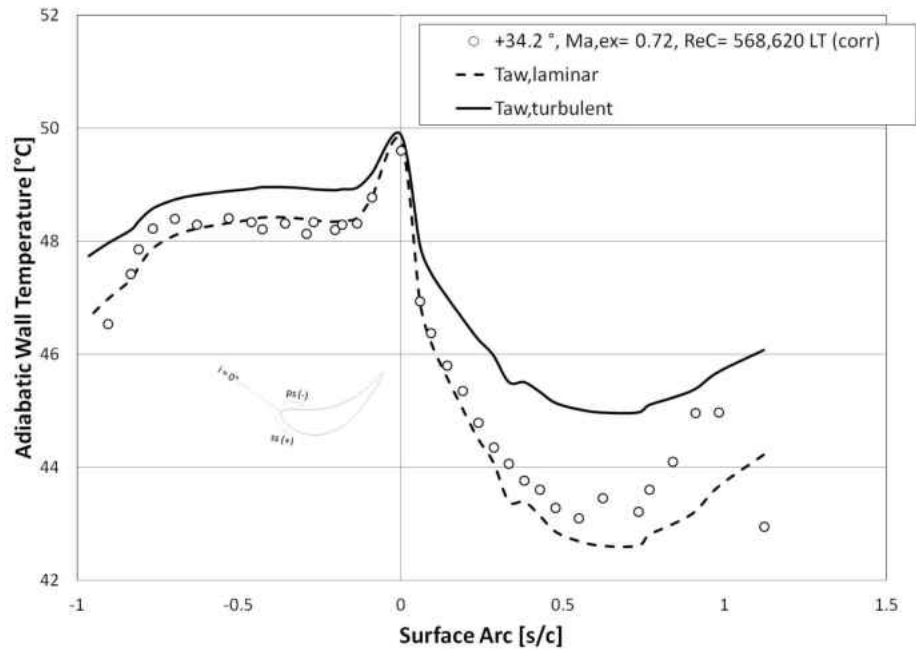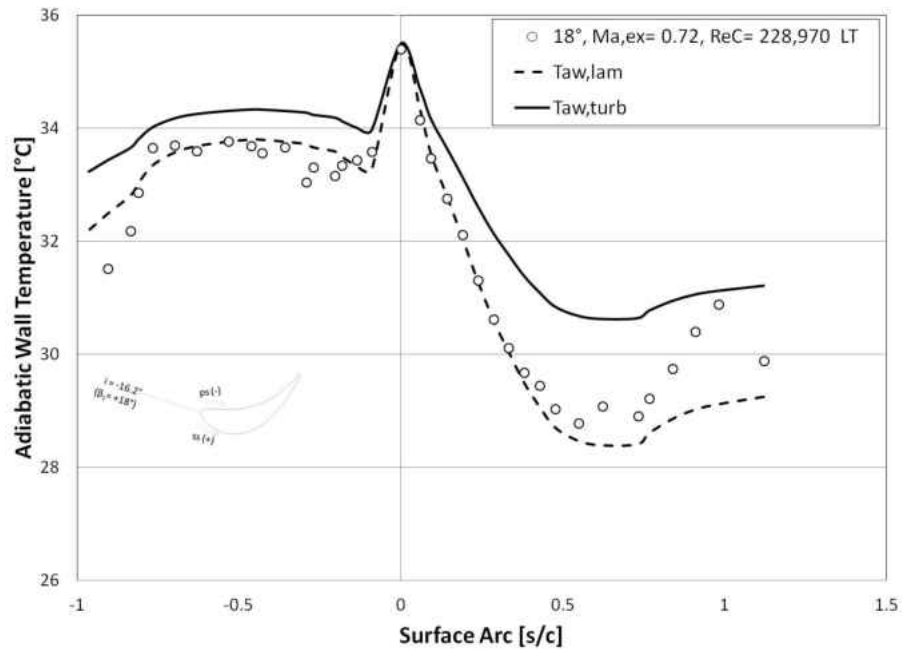
Fig. F.4: Adiabatic Wall Temperature at 0° Incidence Angle, $Re_C = 568,000$, $Ma,ex = 0.72$, LT.
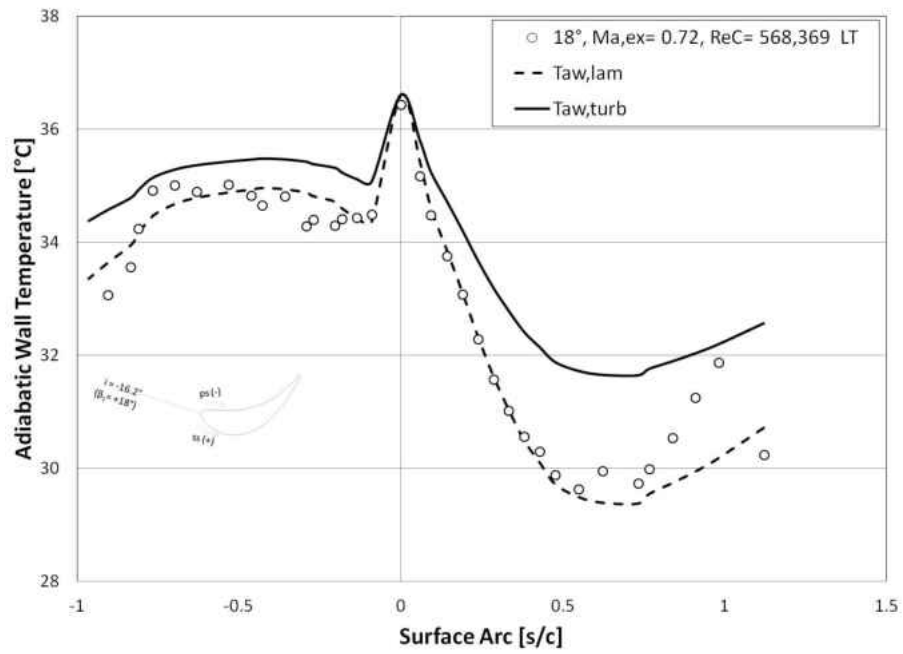
Fig. F.5: Adiabatic Wall Temperature at -16.2° Incidence Angle, $Re_C = 568,000$, $Ma,ex = 0.72$, LT.
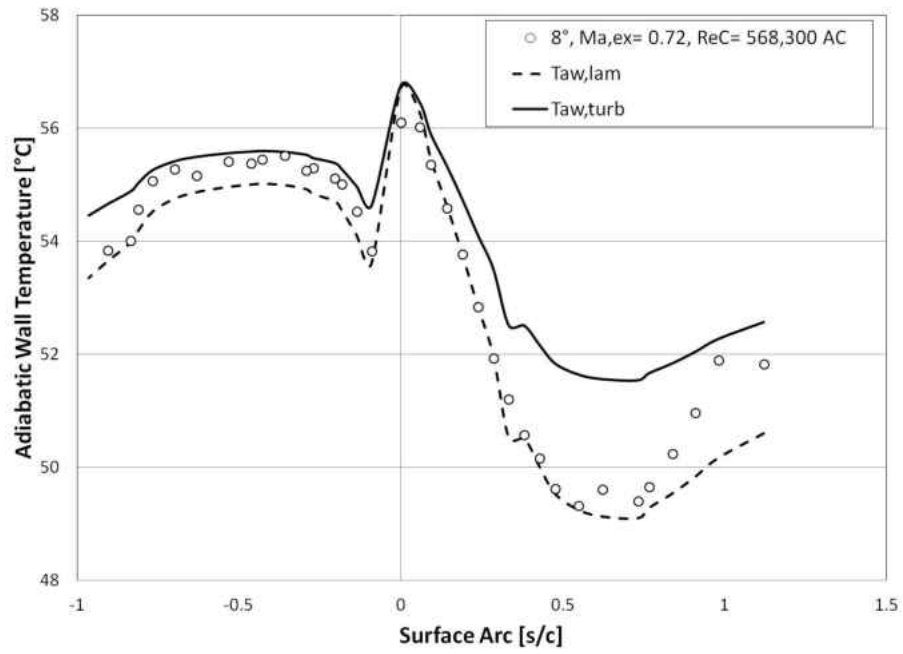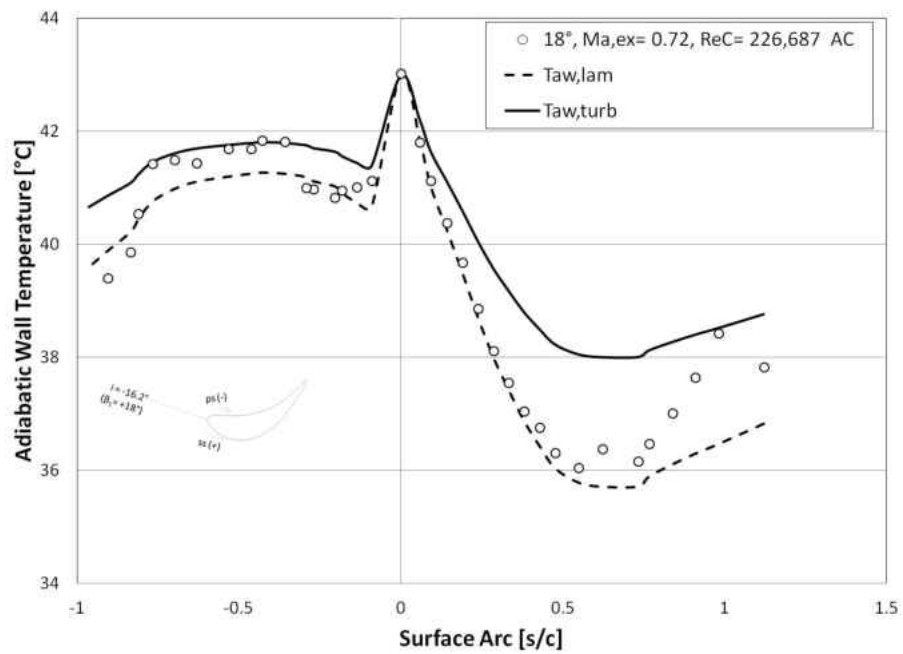
Fig. F.6: Adiabatic Wall Temperature at -26.2° Incidence Angle, $Re_C = 568,000$, $Ma, ex = 0.72$, AC.
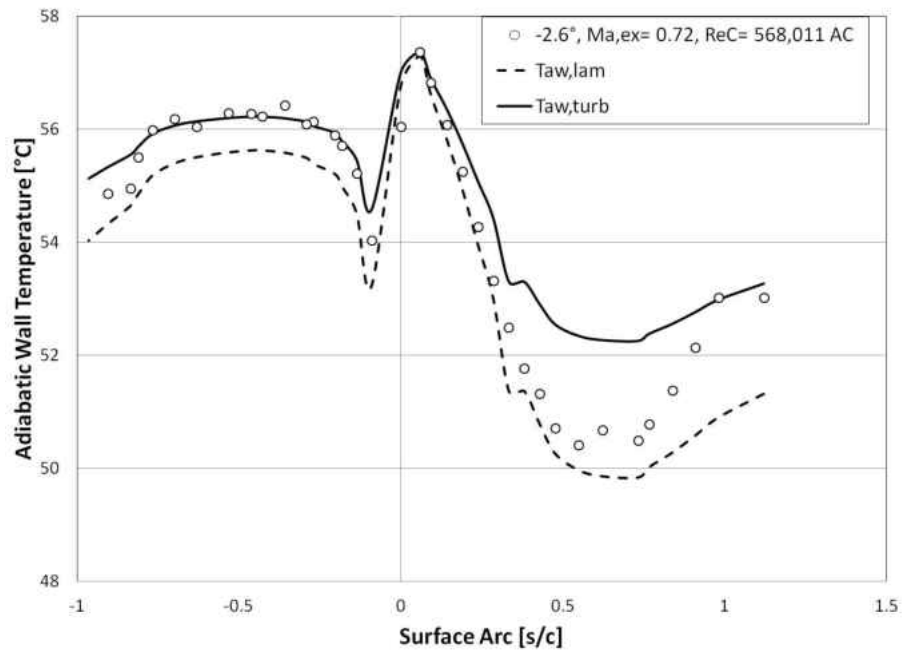
Fig. F.7: Adiabatic Wall Temperature at -36.8° Incidence Angle, $Re_C = 568,000$, $Ma, ex = 0.72$, AC.
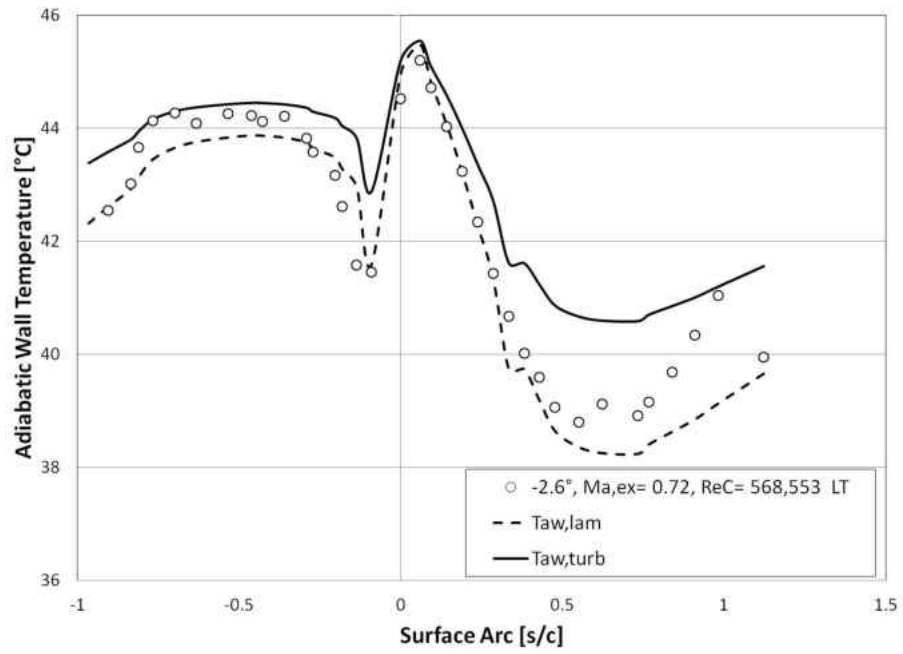
Fig. F.8: Adiabatic Wall Temperature at -36.8° Incidence Angle, $Re_C = 568,000$, $Ma, ex = 0.72$, LT.
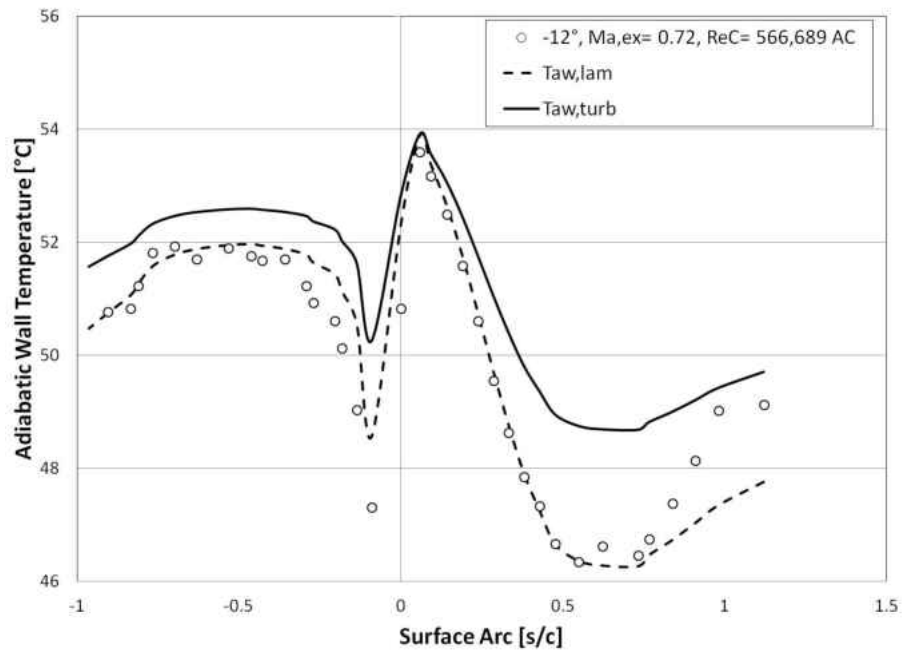
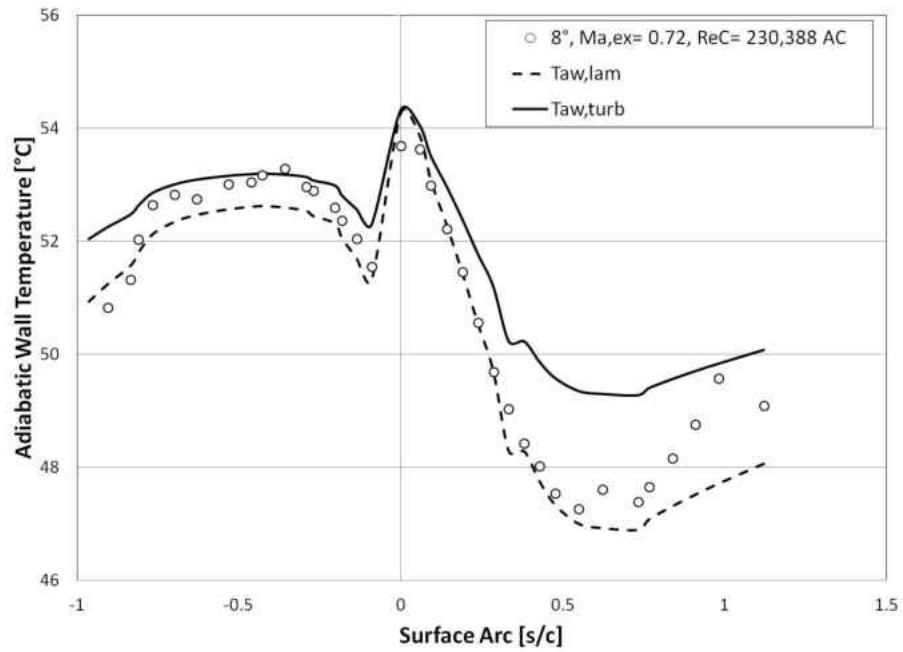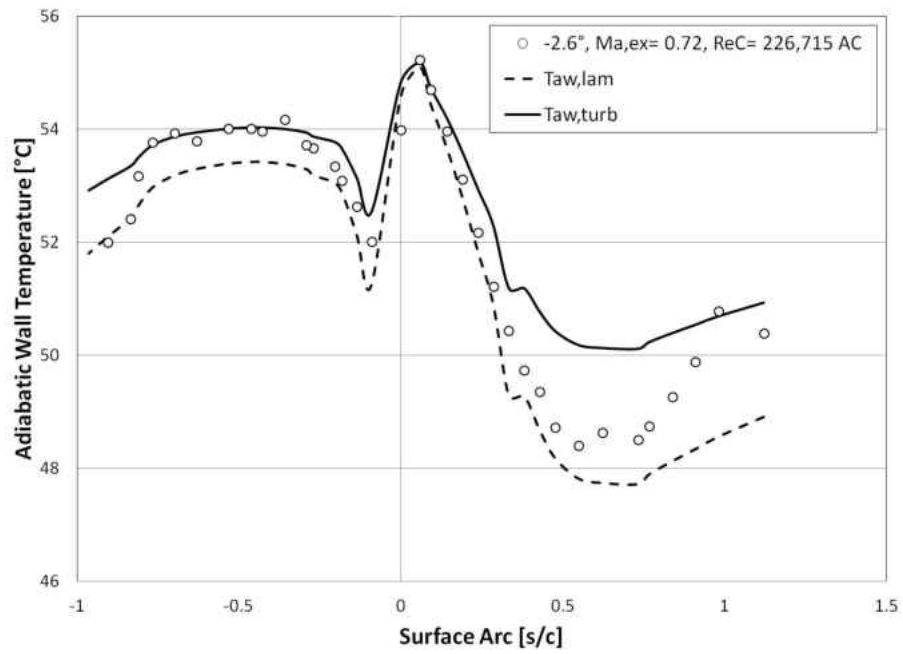Fig. F.9: Adiabatic Wall Temperature at -46.2° Incidence Angle, $Re_C = 568,000$, $Ma, ex = 0.72$, AC.
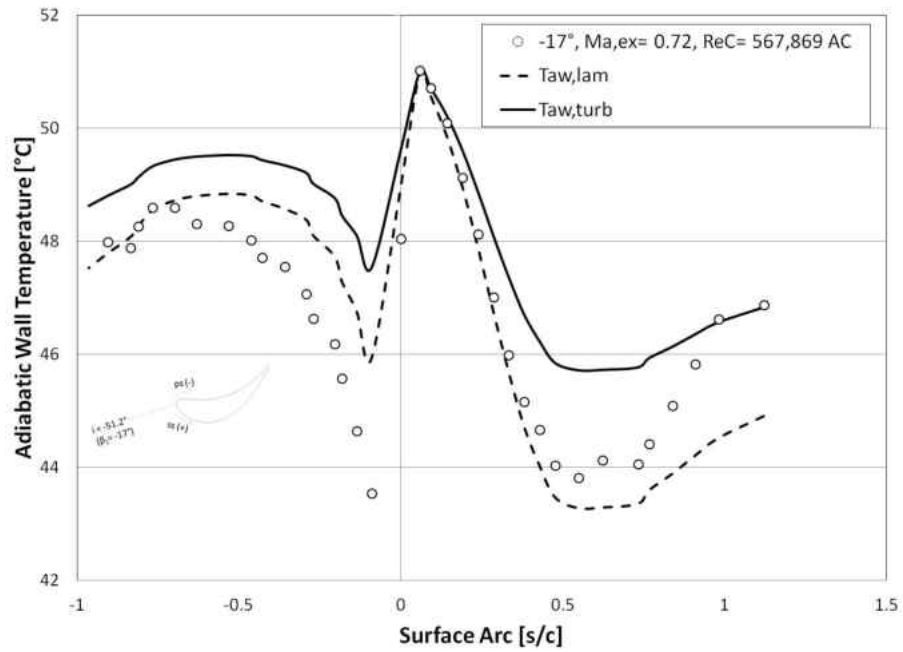
Fig. F.10: Adiabatic Wall Temperature at -51.2° Incidence Angle, $Re_C = 568,000$, $Ma, ex = 0.72$, AC.

Fig. F.11: Adiabatic Wall Temperature at -51.2° Incidence Angle, $Re_C = 568,000$, $Ma, ex = 0.72$, LT.

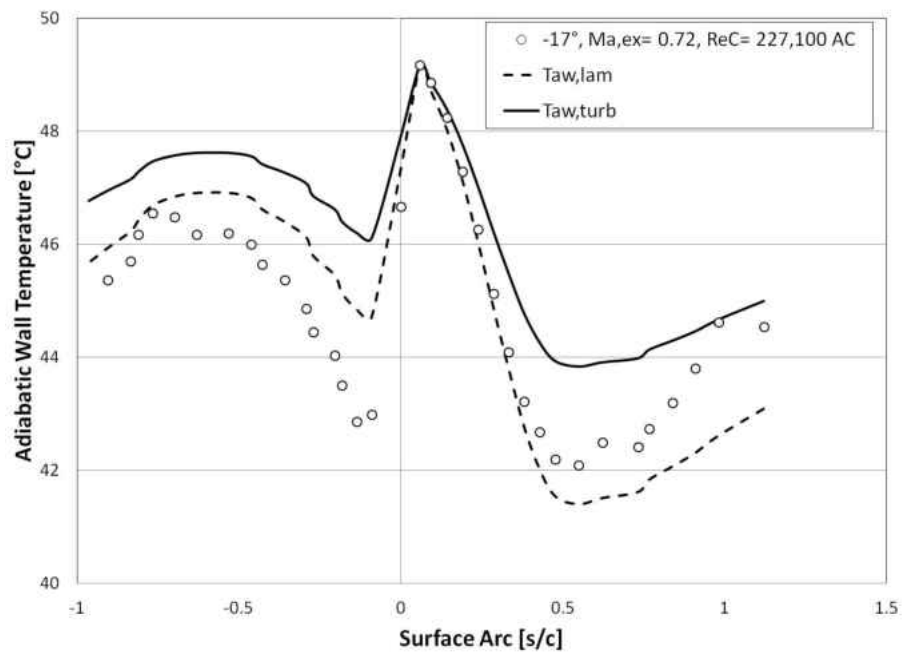Fig. F.12: Adiabatic Wall Temperature at $+5.8°$ Incidence Angle, $Re_C = 228,000$, $Ma, ex = 0.72$, AC.

Fig. F.13: Adiabatic Wall Temperature at $0°$ Incidence Angle, $Re_C = 228,000$, $Ma, ex = 0.72$, AC.

Fig. F.14: Adiabatic Wall Temperature at -16.2° Incidence Angle, $Re_C = 228,000$, $Ma, ex = 0.72$, LT.

Fig. F.15: Adiabatic Wall Temperature at -16.2° Incidence Angle, $Re_C = 228,000$, $Ma, ex = 0.72$, AC.

Fig. F.16: Adiabatic Wall Temperature at -26.2° Incidence Angle, $Re_C = 228,000$, $Ma, ex = 0.72$, AC.

Fig. F.17: Adiabatic Wall Temperature at -36.8° Incidence Angle, $Re_C = 228,000$, $Ma, ex = 0.72$, AC.

Fig. F.18: Adiabatic Wall Temperature at -51.2° Incidence Angle, $Re_C = 228,000$, $Ma, ex = 0.72$, AC.

Appendix G

Stanton Number Plots

Measurement of the total pressure at the cascade inlet resulted to an uncertainty of about $+/-$ 1%. The exit velocity, determined from the exit Mach number, had an uncertainty of about $+/-$ 2%. The uncertainty for the Stanton number was determined to be $+/-$ 5%.
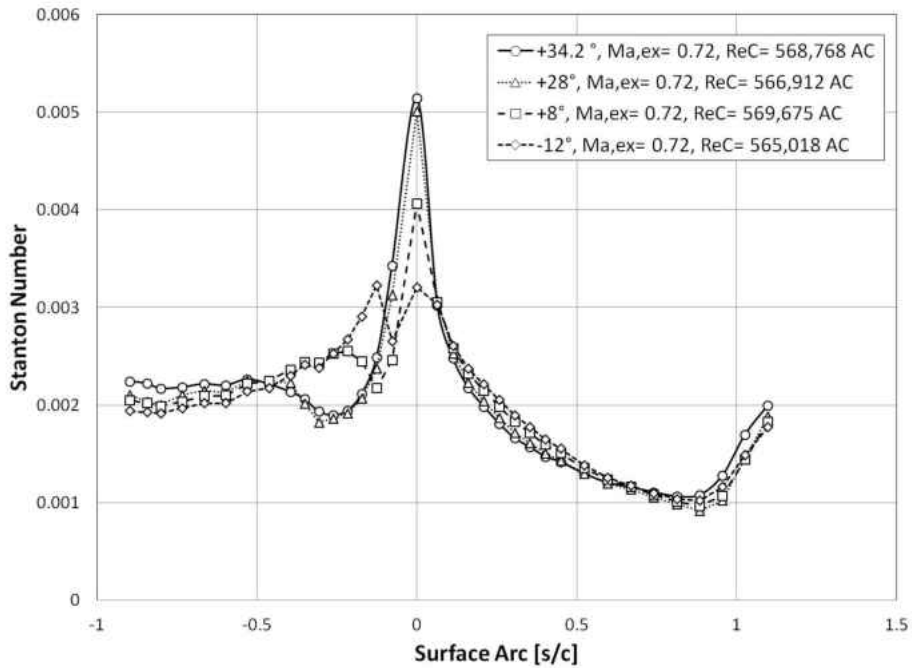

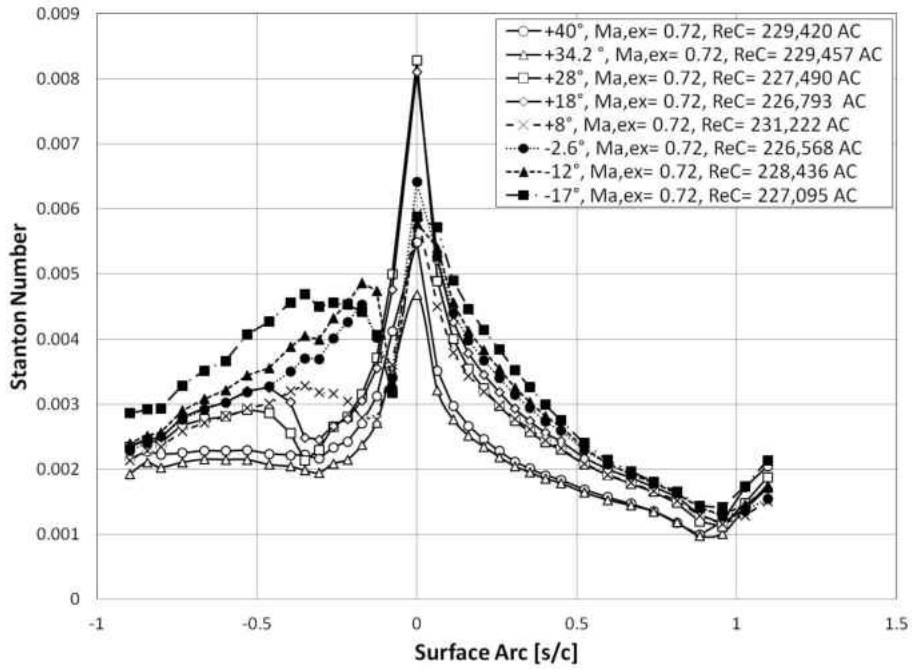Fig. G.1: Stanton Number Distributions at Different Incidence Angles, $Re_C = 568,000$, AC.

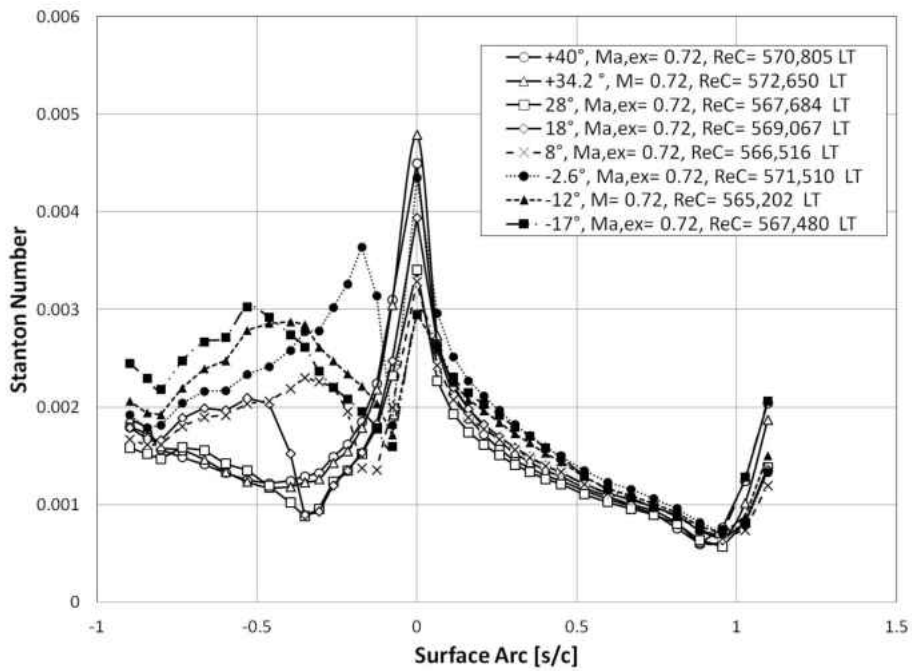Fig. G.2: Stanton Number Distributions at Different Incidence Angles, $Re_C = 228,000$, AC.

Fig. G.3: Stanton Number Distributions at Different Incidence Angles, $Re_C = 568,000$, LT.
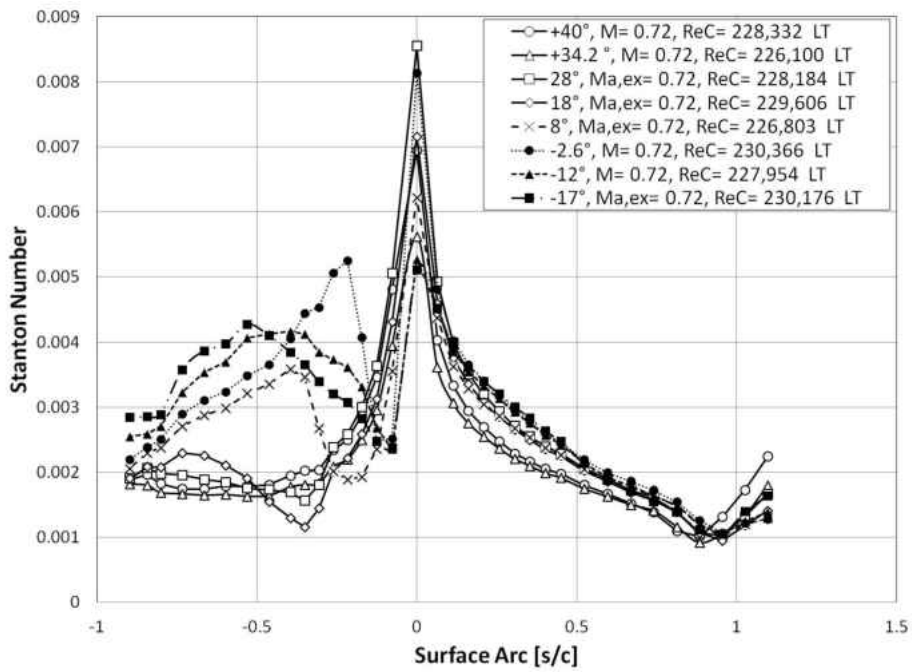
Fig. G.4: Stanton Number Distributions at Different Incidence Angles, $Re_C = 228,000$, LT.